Chapter 1
Geochronology of Layered Intrusions

James S. Scoates and Corey J. Wall

Abstract Layered intrusions crystallize mainly from basaltic magma to form large bodies of igneous rocks that exhibit prominent layering and they preserve stunning rock records of the processes by which magma evolves in crustal magma chambers. These intrusions contain world-class deposits of chromium, platinum group elements (PGE), and vanadium, metals that are vital to industry and society in general. Despite their scientific and practical importance, precise age constraints are lacking for many layered intrusions, and geochronological frameworks linking crystallization and cooling ages for the most part do not exist. This has resulted in critical knowledge gaps related to their origin and formation. This chapter provides an overview of dating methods (U–Th–Pb, $^{40}Ar/^{39}Ar$) and mineral chronometers (e.g., zircon, baddeleyite, rutile, apatite, titanite) potentially present in layered intrusions that is coupled with field, textural, and petrographic criteria for targeting sample selection to allow for the successful implementation of geochronologic studies of layered mafic-ultramafic rocks of any age. As an application, we demonstrate how the thermal history of the Bushveld Complex is documented by mineral ages from samples of the PGE-rich Merensky Reef. High-precision U–Pb zircon ages, involving pretreatment of zircon by the chemical abrasion (annealing and leaching) or CA-TIMS technique, for two samples separated by >300 km are indistinguishable from each other (2056.88 ± 0.41 Ma, Eastern Limb; 2057.04 ± 0.55 Ma, Western Limb; uncertainty reported as 2s) confirming synchronous crystallization of this horizon at near-solidus conditions across the intrusion. Rapid cooling (~125 °C/Ma) down to temperatures of ~400–450 °C is defined by U–Pb rutile ages from the same samples (2052.96 ± 0.61 Ma, 2053.0 ± 2.7 Ma) and a regional hydrothermal event is signaled in $^{40}Ar/^{39}Ar$ biotite ages (1999 ± 10 Ma, 2002 ± 10 Ma). The geochronology of layered intrusions, where magma differentiation processes are captured in a wide range of rock textures and structures, represents an essential tool for assessing the evolution of mafic magmatism in the Earth's crust.

J. S. Scoates (✉) · C. J. Wall
Department of Earth, Ocean & Atmospheric Sciences, Pacific Centre for Isotopic and Geochemical Research, University of British Columbia, Vancouver, BC V6T-1Z4, Canada
e-mail: jscoates@eos.ubc.ca

C. J. Wall
e-mail: cwall@eos.ubc.ca

B. Charlier et al. (eds.), *Layered Intrusions,* Springer Geology,
DOI 10.1007/978-94-017-9652-1_1

Keywords Zircon · Baddeleyite · Cumulates · Bushveld · U–Pb dating

Introduction

For over a century, mafic-ultramafic layered intrusions have fascinated geologists with their detailed records of crystal accumulation and growth that reflect the interplay of a wide variety of magmatic, and post-magmatic, processes in crustal magma chambers (Harker 1904; Bowen 1928; Wager and Brown 1967; Parsons 1987; Cawthorn 1996). Layered intrusions crystallize predominantly from basaltic magma and form sill-like bodies of plutonic igneous rocks that exhibit prominent layering (Irvine 1982) (e.g., Muskox layered intrusion, Fig. 1.1). They consist of cumulates (e.g., Figs. 1.1b, c and d), rocks formed by crystal accumulation, and are the repositories of crystals fractionated from magma. As such, layered intrusions play an important role in illustrating compositional diversity in magmas and they represent a critical link in the evolution of basaltic magma from partial melting in the mantle to differentiation in crustal reservoirs to eruption, in many cases as voluminous and extensive flood basalts. These intrusions are integral components of Earth's continental crust throughout geological time and some host world-class ore bodies of chromium, platinum group elements (PGE), and vanadium (Cawthorn et al. 2005). Mafic layered intrusions may even be exposed on the surface of Mars at Columbia Hills and thus potentially serve as a model for early crustal development of planets (Francis 2011). Accurate and precise ages of rocks from different parts of layered intrusions will define how they are related to each other temporally as well as genetic relations between layered intrusions and their associated ore bodies, links to mafic dike swarms and volcanic rocks within large igneous provinces, and even potential environmental impacts. Yet surprisingly, even the classic mafic layered intrusions in petrology (e.g., Stillwater, Bushveld, Skaergaard) do not yet have robust geochronological frameworks.

In the past decade, major advances in sample pretreatment, instrument sensitivities, and data reduction protocols for U–Th–Pb and $^{40}Ar/^{39}Ar$ geochronology have led to significantly improved precision and accuracy of ages. These advances include development of the combined annealing and partial dissolution analysis of zircon or "chemical abrasion" method of Mattinson (2005) for removing zircon domains that have lost lead, establishment of the "EARTHTIME Initiative" with the goal of improving the precision of U–Pb geochronology through the use of widely available high-purity tracers, synthetic standard solutions, and software systems for data-handling (Schmitz and Schoene 2007; Bowring et al. 2011), and improved accuracy of $^{40}Ar/^{39}Ar$ ages through new calibrations of decay constants and standard ages (Kuiper et al. 2008; Smith et al. 2010; Renne et al. 2010). Combined with the recognition that zircon and other mineral chronometers (e.g., baddeleyite, apatite, rutile, titanite, biotite) can be successfully separated from mafic-ultramafic rocks (e.g., Scoates and Chamberlain 1995; Schwartz et al. 2005; Scoates and Friedman 2008; Grimes et al. 2009; Morisset et al. 2009), it is now possible to date multiple samples from individual layered intrusions allowing for the assessment of variations in their crystallization ages and cooling histories.

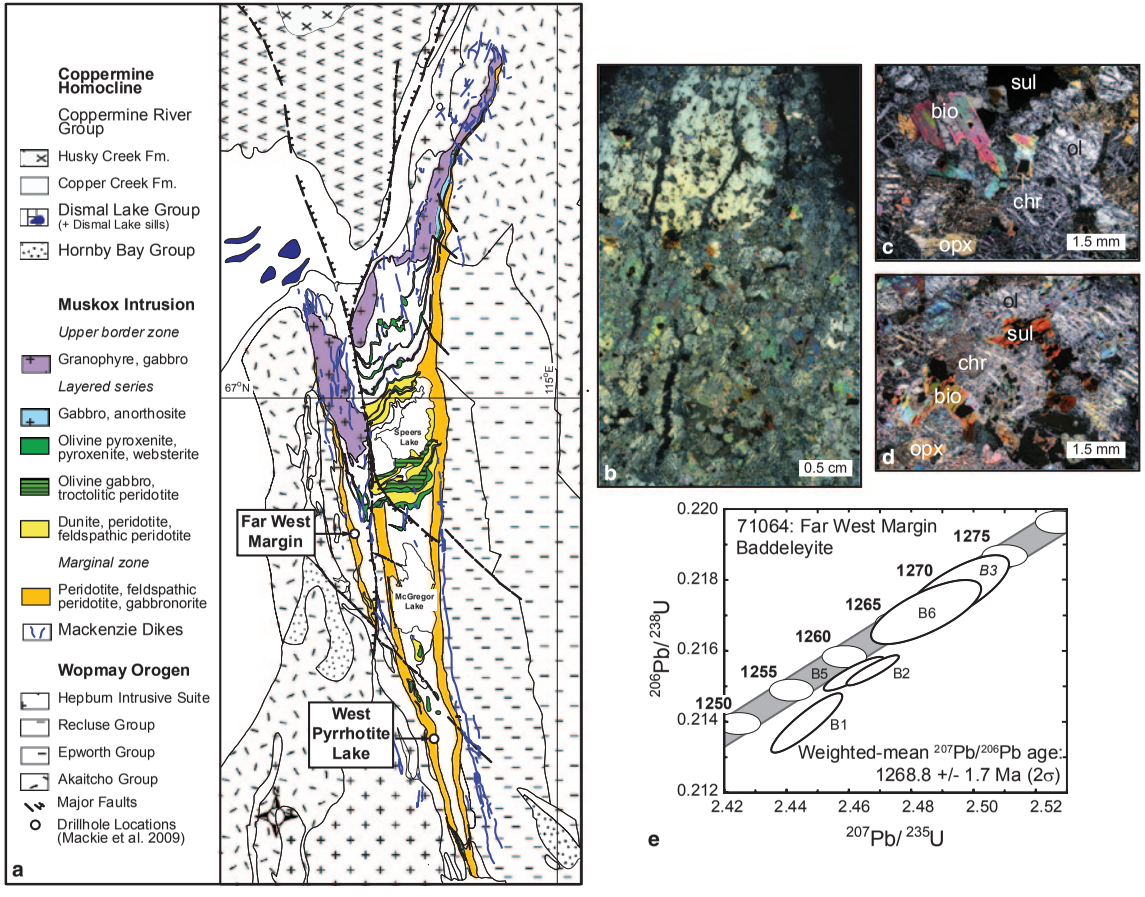

Fig. 1.1 Composite figure showing the application of U–Pb geochronology in determining the age of crystallization of

This contribution begins by providing an overview of the major dating techniques and mineral chronometers available to researchers on layered intrusions. Using the Archean Stillwater Complex (Montana, USA) as a test case, we then outline a field and petrologic approach for a sampling strategy to identify rock types and textures in layered intrusions that are most likely to yield dateable minerals for geochronology. This is followed by an application to dating of the Merensky Reef, host to one of the world's largest concentrations of platinum group elements, from the giant Bushveld Complex in South Africa. Two samples of the Merensky Reef, separated by > 300 km, each yielded multiple mineral chronometers (zircon, rutile, apatite, biotite) that allow for a detailed investigation of their crystallization ages, including a revision of the age reported in Scoates and Friedman (2008), and subsequent cooling path over 50–60 million years in the Paleoproterozoic using combined U–Pb and $^{40}Ar/^{39}Ar$ isotopic systematics. Petrographic relations among dated accessory minerals and rock-forming minerals in the Merensky Reef, coupled with cathodoluminescence imaging of the internal structure of zircon, are fundamentally imperative to interpreting the geochronological results. Finally, we conclude with an overview on future directions in the geochronology of layered intrusions and identify some of the major analytical and conceptual advances that will significantly improve our understanding of the timing of emplacement and geochemical evolution of these remarkable igneous bodies.

Layered Intrusions Through Time

Layered intrusions are present in crustal sequences of the Earth's earliest greenstone belts, they are common in Archean and Proterozoic terranes, and they may be found associated with young Cenozoic continental and oceanic flood basalts (Table 1.1). The oldest terrestrial layered igneous bodies may be the metamorphosed ultramafic sills, 5–30 m wide, which occur within the ca. 3.8 Ga Nuvvuagittuq greenstone belt

an ultramafic rock from the marginal zone of the Muskox layered intrusion, Nunavut, Canada. **a** Geologic map of the Muskox intrusion showing the location of the Far West Margin and West Pyrrhotite Lake drill holes in the marginal zone studied by Mackie et al. (2009) (map after Hulbert 2005, based on the map of Smith 1962). **b** Thin section scan (XPL) of 71064c, a sulphide-bearing, chromite-rich peridotite (sample 71064; 40.3 wt% MgO anhydrous) from near the *top* of the Far West Margin drill hole (28 m depth, ~89 m from contact) that was targeted for dating based on the presence of abundant interstitial biotite (but no interstitial plagioclase). The scan shows several large, cm-scale, poikilitic orthopyroxene crystals including mm-sized olivine (pervasively serpentinized); prominent fractures are filled with secondary magnetite. **c** Photomicrograph showing coarse sulphide (pyrrhotite, pentlandite, chalcopyrite), euhedral chromite, serpentinized olivine, and late biotite overgrowths (note zoning in biotite). **d** Photomicrograph showing interstitial biotite overgrowths around sulphide and chromite in a matrix of serpentinized olivine and poikilitic orthopyroxene. **e** Concordia diagram showing U–Pb geochronological results for baddeleyite from peridotite sample 71064; individual fractions are represented by a 2s error ellipse and labeled B1, B2, etc.; shaded grey band shows the error bounds of the concordia curve taking into consideration uncertainty in the U decay constants. Abbreviation: *Fm* Formation

Table 1.1 Summary of ages of representative layered intrusions through geological time

Intrusion	Region	Location	Era/Period	Age(s)[a]	Method[b]	Rock Type[c]	Reference
Ujaraaluk	Nuvvuagittuq	Québec	Hadean	4406 + 14/−17 Ma	^{146}Sm–^{142}Nd isochron	Meta-mafic/ ultramafic rocks	O'Neil et al. (2012)
Akilia	Itsaq, Isua	Greenland	Eoarchean	3811 ± 4 Ma (min.)	U–Pb zircon SHRIMP	Enclaves in tonalite	Nutman et al. (1996)
Stella		South Africa	Mesoarchean	3033.5 ± 0.3 Ma	U–Pb zircon ID-TIMS	Gabbro	Maier et al. (2003)
Fiskenaesset		Greenland	Mesoarchean	2973 ± 28 Ma	^{147}Sm–^{143}Nd errorchron	Mafic-ultramafic rocks	Polat et al. (2010)
Windimurra	Yilgarn Craton	Australia	Mesoarchean	2813 ± 3 Ma	U–Pb zircon ID-TIMS	Rhyolite in roof pendant	Ivanic et al. (2010)
Bird River	Manitoba	Canada	Neoarchean	2743.0 ± 0.5 Ma	U–Pb zircon CA-TIMS	Gabbro	Scoates and Scoates (2013)
Mulcahy Lake	Ontario	Canada	Neoarchean	2733.2 ± 1.0 Ma	U–Pb zircon ID-TIMS	Mt-rich gabbro	Morrison et al. (1985)
Stillwater	Montana	USA	Neoarchean	2701 ± 8 Ma	^{147}Sm–^{143}Nd isochron	Gabbronorite	DePaolo and Wasserburg (1979)
				2704 ± 1 Ma	U–Pb zircon ID-TIMS	Pegmatitic anorthosite	Premo et al. (1990)
				2709.05 ± 0.85 Ma	U–Pb zircon CA-TIMS	Pegmatitic troctolite	Wall et al. (2010)
Great Dyke		Zimbabwe	Neoarchean	2575.9 ± 1.0 Ma	U–Pb zircon ID-TIMS	Orthopyroxenite	Oberthür et al. (2002)
Lukkulaisvaara	Karelia	Russia	Paleoproterozoic	2442.1 ± 1.4 Ma	U–Pb zircon ID-TIMS	Gabbroic pegmatite	Amelin et al. (1995)
Kemi	Elijfirvi	Finland	Paleoproterozoic	2.44 Ga	U–Pb zircon ID-TIMS	Gabbro	Patchett et al. (1981)
Bushveld		South Africa	Paleoproterozoic	2056.88 ± 0.41 Ma	U–Pb zircon CA-TIMS	Pegmatitic orthopyroxenite	This study

Table 1.1 (continued)

Intrusion	Region	Location	Era/Period	Age(s)[a]	Method[b]	Rock Type[c]	Reference
Fox River	Manitoba	Canada	Paleoproterozoic	1882.9±1.5 Ma	U–Pb zircon ID-TIMS	Gabbroic pegmatite	Heaman et al. (1986)
Panton	East Kimberley	Australia	Paleoproterozoic	1856±2 Ma	U–Pb zircon SHRIMP	Anorthosite	Page and Hoatson (2000)
Poe Mountain	Laramie	Wyoming, USA	Mesoproterozoic	1434.4±0.6 Ma	U–Pb bad-deleyite ID-TIMS	Anorthosite	Scoates and Chamberlain (1995)
Kiglapait	Nain, Labrador	Canada	Mesoproterozoic	1305±22 Ma	^{147}Sm–^{143}Nd isochron	Ferrodiorite	DePaolo (1985)
Muskox	Nunavut	Canada	Mesoproterozoic	1269.4±1.1 Ma	U–Pb bad-deleyite ID-TIMS	Feldspathic peridotite	French et al. (2002)
				1268.8±1.7 Ma	U–Pb bad-deleyite ID-TIMS	Chr-bearing peridotite	Mackie et al. (2009)
Ilimaussaq	Gardar Province	Greenland	Mesoproterozoic	1160±5 Ma	U–Pb bad-deleyite ID-TIMS	Augite syenite	Krumrei et al. (2006)
Duluth	Duluth Complex	Minnesota, USA	Mesoproterozoic	1099.1±0.2 Ma	U–Pb zircon ID-TIMS	Anorthosite	Schmitz et al. (2003)
Sonju Lake	Duluth Complex	Minnesota, USA	Mesoproterozoic	1096.1±0.8 Ma	U–Pb bad-deleyite ID-TIMS	Apatite ferrodiorite	Paces and Miller (1993)
Bjerkreim–Sokndal	Rogaland	Norway	Neoproterozoic	932±5 Ma	U–Pb zircon ID-TIMS	Quartz mangerite	Pasteels et al. (1979)
Sept Iles	Québec	Canada	Neoproterozoic	565±4 Ma	U–Pb zircon ID-TIMS	Granophyre	Higgins and van Breemen ((1998)
Fongen-Hyllingen	Caledonides	Norway	Silurian	437.8±2.3 Ma	U–Pb zircon ID-TIMS	Monzonite	Nilsen et al. (2007)

Table 1.1 (continued)

Intrusion	Region	Location	Era/Period	Age(s)[a]	Method[b]	Rock Type[c]	Reference
Hongge	Emeishan	China	Permian	259.3 ± 1.3 Ga	U–Pb zircon ID-TIMS	Ilm-rich gabbro	Zhong and Zhu (2006)
Dufek	Ferrar	Antarctica	Jurassic	183.9 ± 0.3 Ma	U–Pb zircon ID-TIMS	Granophyre	Minor and Mukasa (1997)
Duke Island	Alaska	USA	Cretaceous	108 ± 1 Ma	U–Pb zircon ID-TIMS	Hbl-plag pegmatite	Saleeby (1992)
Rum	Inner Hebrides	Scotland	Paleocene	60.53 ± 0.08 Ma	U–Pb zircon ID-TIMS	Feldspathic pegmatite	Hamilton et al. (1998)
Skaergaard	East Greenland	Greenland	Eocene	55.40 ± 0.14 Ma	$^{40}Ar/^{39}Ar$ hornblende	Granophyre	Hirschmann et al. (1997)
				55.960 ± 0.018 Ma	U–Pb zircon CA-TIMS	Ferrodiorite	Wotzlaw et al. (2012)
Kap Edvard Holm	East Greenland	Greenland	Eocene	48.8 ± 0.2 Ma	$^{40}Ar/^{39}Ar$ hornblende	Gabbroic pegmatite	Tegner et al. (1998)
Val	Kerguelen	Indian Ocean	Oligocene	24.25 ± 0.15 Ma	U–Pb zircon ID-TIMS	Gabbro	Scoates et al. (2007)

[a] Uncertainty reported as 2s; all ages reported as Ma, except where there is insufficient precision (Ga)

[b] Abbreviations: SHRIMP = sensitive high-resolution ion microprobe, *ID-TIMS* isotope dilution-thermal ionization mass spectrometry, *CA-TIMS* chemical abrasion-thermal ionization mass spectrometry

[c] Abbreviations: *Mt* magnetite, *Chr* chromite, *Ilm* ilmenite, *Hbl* hornblende

of the Superior Province, Canada (O'Neil et al. 2007, 2012). The sill interiors are composed predominantly of serpentine and talc, however, they also contain amphibole-rich layers and layers of metamorphic orthopyroxene that represent original pyroxene cumulate horizons (O'Neil et al. 2007). These ultramafic sills are geochemically correlative with the Ujaraaluk unit amphibolites of volcanic protolith (O'Neil et al. 2011) for which a ^{146}Sm–^{142}Nd isochron age of 4406 + 14/− 17 Ma has been determined (O'Neil et al. 2012) (Table 1.1). Neoarchean layered intrusions hosting stratiform chromitites occur in the 3.81 Ga deformed layered anorthosite-ultramafic intrusions in the Ivîsartoq region of West Greenland (Rollinson et al. 2002) and Paleoarchean komatiitic sills with chromitite layers are recognized in the Zimbabwe craton (Prendergast 2008). Mesoarchean stratiform chromitites and layered intrusions are found in India (Mondal et al. 2006), South Africa (Maier et al. 2003), Greenland (Fiskenaesset, Polat et al. 2010), and western Australia (Ivanic et al. 2010). Layered intrusions are notable in the Neoarchean rock record from ca. 2700–2750 Ma, especially in the Superior Province of Canada, and also include the Stillwater Complex in the Wyoming Province of southwestern Montana (Hess 1960; Jackson 1961; McCallum 1996). The Bushveld Complex, the world's largest layered intrusion and host to remarkable resources of chromium, platinum group elements, and vanadium (Eales and Cawthorn 1996; Cawthorn et al. 2005; Cawthorn (Chap. 12, The Bushveld Complex), is one of a number of major Paleoproterozoic intrusions that are also exemplified by mafic intrusions in the eastern Baltic (Fennoscandian) Shield (Amelin et al. 1995), the Kemi intrusion of northern Finland with its major chromite deposit (Alapieti et al. 1989), the 250 km-long Fox River Sill in northeastern Manitoba (Scoates 1990), and numerous layered mafic-ultramafic intrusions in the East Kimberley of western Australia (Hoatson and Blake 2000). Mesoproterozoic layered intrusions are typically related to either crustal extension and rifting (e.g., 1.27 Ga Muskox intrusion, Mackenzie large igneous province, northern Canada, Fig. 1.1; 1.1 Ga Duluth complex, Keweenawan or Midcontinent Rift, Minnesota; 0.56 Ga Sept Iles intrusion, eastern Québec) or with Proterozoic anorthosite plutonic suites (e.g., 1.43 Ga Poe Mountain intrusion, Laramie; 1.3 Ga Kiglapait intrusion, Nain; ca. 0.93 Ga Bjerkreim–Sokndal intrusion, Rogaland) (Table 1.1). The Phanerozoic record of layered intrusions, including the 56 Ma Skaergaard intrusion in East Greenland (Wager and Brown 1967; Wotzlaw et al. 2012), is dominated by those that are part of large igneous provinces (e.g., Emeishan, Ferrar, North Atlantic) (Table 1.1). This association reflects their emplacement during large-scale crustal rifting and outpouring of voluminous flood basalt sequences and development of high-level magma reservoirs as staging chambers prior to the eruption of flood basalts on oceanic islands (e.g., 24 Ma Val gabbro, Kerguelen Archipelago, southern Indian Ocean; Scoates et al. 2007).

Cumulates and Geochronology

Layered intrusions consist of cumulates (Fig. 1.2), rocks that began by forming on magma chamber floors, walls, and roofs as a framework of touching minerals, cumulus crystals or "primocrysts", with interstitial melt or intercumulus melt filling

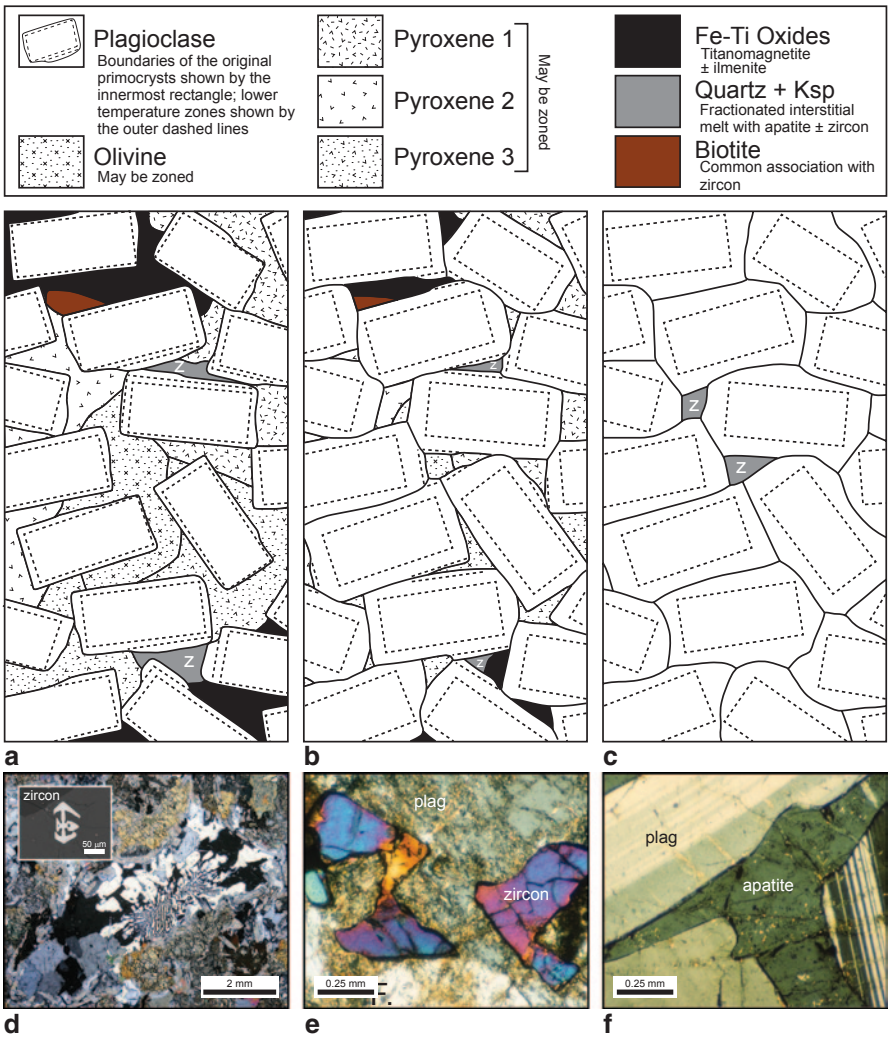

Fig. 1.2 Schematic diagrams and photomicrographs showing the textural setting of dateable accessory minerals in different types of plagioclase cumulates in layered intrusions. Diagrams are after Wager et al. (1960). **a** Plagioclase cumulate with abundant poikilitic pyroxene, olivine, and Fe–Ti oxides, and interstitial *patches* of quartz/K-feldspar that represent a component of the most fractionated interstitial melt; zircon (and apatite) is preferentially associated with these interstitial residual areas and with late biotite overgrowths. **b** Plagioclase cumulate with minor amounts of interstitial pyroxene, olivine, and Fe–Ti oxides, and small interstitial *patches* of fractionated interstitial melt (quartz/K-feldspar). **c** Pure plagioclase cumulate (anorthosite) with cumulus and interstitial plagioclase; anorthosites generally make excellent target rocks for dating. **d** Photomicrograph of a large granophyre clot (quartz/K-feldspar) within subophitic gabbronorite of the marginal zone, Muskox intrusion (West Pyrrhotite Lake, sample 71139). The clot contains abundant acicular apatite and minor hopper (skeletal) zircon shown in the backscatter electron image inset. **e** Photomicrograph of interstitial (poikilitic) zircon in layered leucogabbro of the Poe Mountain intrusion, Laramie anorthosite complex, Wyoming. **f** Photomicrograph of interstitial apatite in layered leucogabbro of the Poe Mountain intrusion, Laramie anorthosite complex, Wyoming (sample PM310)

the pore spaces (Wager et al. 1960; Wager and Brown 1967; Irvine 1982; Hunter 1996). From the perspective of geochronology, the evolution of this interstitial melt and its potential to saturate in the U–Th–Pb-bearing minerals (e.g., zircon, baddeleyite, apatite) and K-bearing minerals (e.g., biotite, amphibole) that can be dated by modern, high-precision geochronological techniques is of critical importance (Figs. 1.2a, b and c). Crystal frameworks in slowly cooled intrusions are characterized by an initial high porosity and permeability (e.g., Jerram et al. 2003) that allow exchange of melt from the crystal mush to the main body of magma by compositional convection or by diffusion (e.g., Morse 1986). Elimination of this porosity occurs by consolidation or densification of the crystal mush (e.g., Wager and Brown 1967; Irvine 1982; Hunter 1996). This may involve a variety of processes, including (1) continued crystallization and growth of cumulus crystals from interstitial melt, (2) crystallization of new minerals from evolved interstitial melt that grow as poikilitic or subpoikilitic crystals surrounding cumulus crystals, (3) crystallization of remaining melt as zoned overgrowths on cumulus crystals, as pockets of minerals that crystallize from fractionated melt such as quartz, alkali feldspar, biotite ± zircon/baddeleyite/apatite, or as mono-mineralic rims on cumulus crystals that represent the presence of grain boundary liquid during the final stages of crystallization of mafic intrusions (e.g., Holness et al. 2007), and (4) mechanical compaction. Some adcumulates, cumulates with only minor postcumulus material (Irvine 1987), may also have formed directly on the surface of the cumulate pile (Campbell et al. 1983; Campbell 1987). Crystal ageing (Boudreau 2011) and textural coarsening (Higgins 2011; Higgins (Chap. 3, Quantitative textural analysis of rocks in layered mafic intrusions)) may also modify the final texture of a cumulate.

The ability to successfully date a layered intrusion depends on selecting appropriate samples that have a high probability of containing extractable quantities of minerals that can be used as chronometers. For reasons outlined in subsequent sections, zircon ($ZrSiO_4$) is the most important mineral that can be dated to high precision and accuracy from layered intrusions. Not only is zircon found in mafic or ultramafic cumulates from layered intrusions (e.g., Premo et al. 1990; Scoates and Friedman 2008; Scoates and Scoates 2013), but it also occurs in a wide range of other mafic cumulates, including gabbros from mid-ocean ridges (e.g., Grimes et al. 2009; Schmitt et al. 2011) and plagioclase-rich rocks from Proterozoic anorthosite plutonic suites (e.g., McLelland and Chiarenzelli 1990; Scoates and Chamberlain 1995, 2003). Experimental results demonstrate that zircon cannot crystallize directly from basaltic liquids because unrealistically high Zr concentrations (> 5000 ppm) in the melt would be required (Boehnke et al. 2013). Thus, zircon that is found in mafic-ultramafic rocks, and that is not inherited as pre-existing crystals from other rocks, must have crystallized from late-stage, evolved melts probably at near-solidus temperatures (e.g., Scoates and Chamberlain 1995; Grimes et al. 2009; Boehnke et al. 2013). If zircon and other U–Th–Pb-bearing accessory minerals crystallize from liquid that is interstitial to cumulus grains and is trapped (i.e., the permeability of the consolidating cumulate goes to zero), these accessory phases should be directly associated with other lower temperature minerals that will saturate (e.g., quartz, alkali feldspar, magnetite/ilmenite, biotite; Fig. 1.2d) (Meurer and Meurer

2006). In contrast, if zircon is not associated with these near-solidus minerals or occurs as poikilitic overgrowths (Fig. 1.2e), it did not crystallize from a trapped liquid, but rather from an evolved liquid undergoing expulsion from the semi-consolidated cumulate by compaction (e.g., Meurer and Boudreau 1998; Meurer and Meurer 2006). In this contribution, textural observations of the in situ relationship between zircon and other minerals in mafic-ultramafic cumulates that are fundamental in constraining the relative timing of zircon crystallization will be addressed in the context of zircon from the Merensky Reef of the Bushveld Complex.

Dating Methods for Layered Intrusions

There are number of excellent and comprehensive references on geochronological techniques that should be a starting point for any researcher interested in the dating of layered intrusions. These include the book by McDougall and Harrison (1999) on $^{40}Ar/^{39}Ar$ geochronology, volume 53 of the Reviews in Mineralogy and Geochemistry entitled "Zircon" published by the Mineralogical Society of America (Hanchar and Hoskin, editors), which includes key chapters on the history of U–Th–Pb geochronology, analytical methods, and a very useful atlas of zircon textures (Corfu et al. 2003), and the May 2013 issue of Elements focused on "One Hundred Years of Geochronology" (Condon and Schmitz, guest editors). The Second Edition of the Treatise on Geochemistry also contains an exceptional overview on "U–Th–Pb Geochronology" by Schoene (2014). In the section below, the most commonly used dating approaches, isotopic systems, analytical techniques and protocols, and mineral chronometers are reviewed in the context of their application to layered intrusions.

Mineral-Whole Rock Isochrons

Due to elemental redistribution during post-crystallization hydrothermal alteration and metamorphism in ancient (Proterozoic to Archean) mafic and ultramafic rocks, obtaining precise and accurate dates of layered intrusions in the 1960s and 1970s was a challenge using conventional Rb–Sr, K–Ar, and U–Th–Pb methods. This changed with the pioneering application of Sm–Nd isotopes to the Stillwater Complex by DePaolo and Wasserburg (1979) who reported a precise age of 2701 ± 8 Ma for a gabbronorite from just below the J-M Reef (West Fork Adit). This age was based on the isochron relationship defined by the analyses of the whole rock and separates of plagioclase, clinopyroxene, and orthopyroxene (Fig. 1.3a). A similar U–Pb zircon-baddeleyite age of 2704 ± 1 Ma was determined from the Lower Banded Series of the Stillwater Complex by Premo et al. (1990) and more recent dating has revealed that most of the Lower Banded Series crystallized at 2709 Ma (Wall et al. 2010).

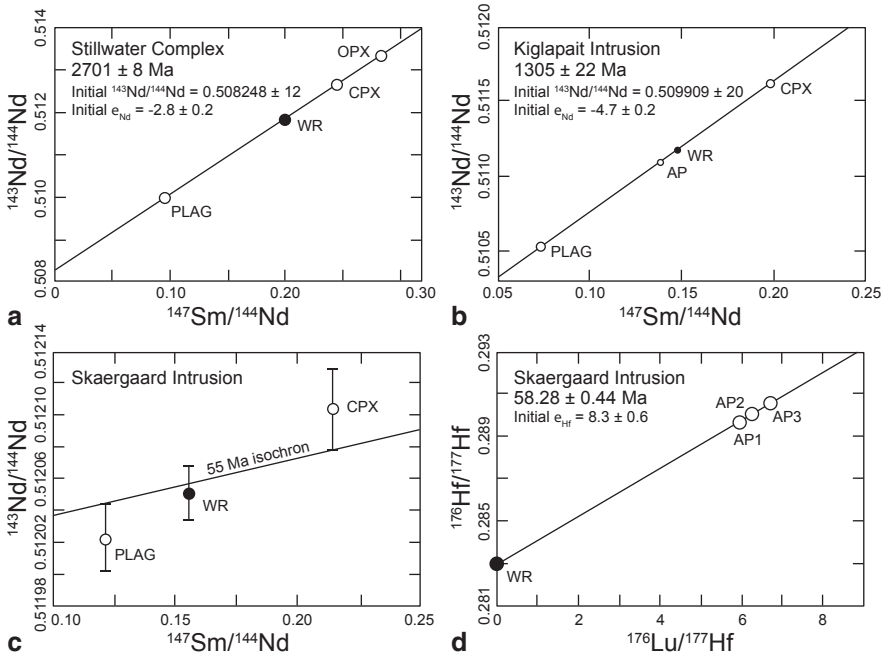

Fig. 1.3 Isochron plots showing mineral–whole rock isotopic results for representative layered intrusions. **a** Stillwater Complex: $^{147}Sm/^{144}Nd$ vs. $^{143}Nd/^{144}Nd$ plot showing analytical results of the whole rock, plagioclase, clinopyroxene, and orthopyroxene from a gabbronorite (STL-100) from the West Fork of the Stillwater River (top of Gabbronorite II in the Lower Banded Series) that define an isochron with an age of 2701 ± 8 Ma (modified from DePaolo and Wasserburg 1979). **b** Kiglapait intrusion: $^{147}Sm/^{144}Nd$ vs. $^{143}Nd/^{144}Nd$ plot showing analytical results for the whole rock, plagioclase, apatite, and clinopyroxene from a ferrodiorite (3379) from the *Upper* Zone at the 98.6 PCS level (modified from DePaolo 1985) that define an isochron age of 1305 ± 22 Ma. **c**. Skaergaard intrusion: $^{147}Sm/^{144}Nd$ vs. $^{143}Nd/^{144}Nd$ plot showing analytical results of the whole rock, plagioclase, and clinopyroxene from a ferrogabbro (SK-80) from *Upper* Zone c, 2540 m above the base of the Layered Series that appear to show isotopic heterogeneity between minerals with a 55 Ma reference isochron only just barely intersecting the error bars of the analyses for co-existing plagioclase and clinopyroxene (modified from Stewart and DePaolo 1990). **d** Skaergaard intrusion: $^{176}Lu/^{177}Hf$ vs. $^{176}Hf/^{177}Hf$ plot showing analytical results for the whole rock and three apatite fractions from an apatite-rich ferrogabbro (GGU-348881) from *Upper* Zone b that define a precise Lu–Hf isochron age of 58.28 ± 0.44 Ma (modified from Barfod et al. 2003). Abbreviations: *PLAG* plagioclase; *WR* whole rock; *CPX* clinopyroxene; *OPX* orthopyroxene; *AP* apatite (AP1, AP2, AP3 indicate different analyses of apatite)

Isochron diagrams compare the number of parent atoms in a radioactive decay scheme to the number of daughter atoms where the isotopes of the parent-daughter atoms are normalized to a stable isotope in the system of interest (e.g., Rb–Sr method: $^{87}Sr/^{86}Sr$ vs. $^{87}Rb/^{86}Sr$; Sm–Nd method: $^{143}Nd/^{144}Nd$ vs. $^{147}Sm/^{144}Nd$) (Faure and Mensing 2005; White 2013). The slope of the line passing through the data for the analyzed samples, with variable parent-daughter concentration ratios, is related to the age of the system and is called an isochron (Fig. 1.3). The intercept of the iso-

chron is equal to the initial ratio, which is useful for fingerprinting magma sources and contamination. The isochron method of dating requires that all samples or minerals dated have the same initial isotopic ratio and crystallized at the same time. Precise isochron dating is critically dependent on analyzing minerals and whole rocks from the same samples with a wide range of parent-daughter concentration ratios (e.g., Rb/Sr, Sm/Nd, Lu/Hf). Deviations from the isochron may indicate open-system behavior during alteration or metamorphism and this leads to the possibility of defining secondary isochrons that date the approximate timing of these events. For example, in the Stillwater Complex, the $^{87}Rb/^{86}Sr$ isotopic systematics of plagioclase, clinopyroxene, and orthopyroxene from the gabbronorite that yielded the precise Sm–Nd whole rock-mineral isochron do not define a straight line in an isochron plot and, instead, lie closer to a 2.2 Ga isochron (DePaolo and Wasserburg 1979). These disparate results are consistent with differences in the relative mobility of the two parent-daughter systems during low-grade metamorphism with the Sm–Nd isotope systematics remaining unaffected.

The use of mineral-whole rock isochrons, especially Sm–Nd isochron dating, has been successfully applied to constraining the ages of crystallization and other events in a number of important layered intrusions (e.g., Stillwater, Kiglapait). Even though the uncertainty of these ages can be high (up to several percent), they are useful for broadly characterizing temporal relationships between intrusions and host rocks and for assessing regional tectonic controls on magmatism. DePaolo (1985) reported a Sm–Nd isochron age of 1305 ± 22 Ma for a ferrodiorite from the Upper Zone of the Kiglapait intrusion, Labrador, based on the analytical results from plagioclase, apatite, the whole rock, and clinopyroxene (Fig. 1.3b). For the same sample, it was not possible to determine a precise Rb–Sr isochron due to the limited range of Rb/Sr in the minerals. For the Muskox intrusion (Fig. 1.1a), part of the giant Mackenzie large igneous province that also includes the Coppermine River flood basalts and the Mackenzie dike swarm in northern Canada, a Sm–Nd isochron (plagioclase, whole rock, clinopyroxene, orthopyroxene) of 1258 ± 40 Ma was determined for a gabbronorite from Cyclic Unit 22 near the top of the cumulate sequence (Stewart and DePaolo 1996). This age, while relatively imprecise, is in agreement with the higher precision U–Pb baddeleyite dating of the Muskox intrusion (e.g., 1270 ± 4 Ma, LeCheminant and Heaman 1989; 1268.8 ± 1.7 Ma, Mackie et al. 2009). Intriguingly, Stewart and DePaolo (1996) also reported an Sm–Nd isochron age of 1822 ± 165 Ma for a sample of roof zone breccia in the Muskox intrusion, thus providing evidence that this material actually represents a stoped piece of surrounding wall rock. All Rb–Sr isochrons in the Muskox intrusion are young (1000–1139 Ma) due to disturbance of the Sr isotopic systematics during a ca. 1000 Ma metamorphic event (Stewart and DePaolo 1996).

When applied to the Skaergaard intrusion of East Greenland, mineral-whole rock isochron results provide both crystallization age information (i.e., data from analyses of individual samples lie along 55 Ma isochrons) and evidence for resetting due to metamorphism and partial melting from the nearby Basistoppen intrusion (Stewart and DePaolo 1990), despite showing limited variations in Rb/Sr and Sm/Nd and in initial $^{87}Sr/^{86}Sr$ and $^{143}Nd/^{144}Nd$. Importantly, the Sm–Nd isotopic systematics

of a sample from Upper Border Zone c, where the 55 Ma isochron barely intercepts the error bars of the analyses for plagioclase and clinopyroxene (Fig. 1.3c) and where the Rb–Sr isochron is coherent, suggested that isotopic heterogeneity between minerals in cumulates may need to be considered (e.g., incomplete equilibration between cumulus crystals and interstitial melt derived from another part of the intrusion). Evidence for mineral-scale isotopic heterogeneity in the Skaergaard intrusion was confirmed by McBirney and Creaser (2003) and there is now an increasing number of studies from the Bushveld Complex that document initial Sr–Nd isotopic differences between plagioclase and orthopyroxene (Prevec et al. 2005; Chutas et al. 2012; Roelofse and Ashwal 2012).

A promising approach to dating layered intrusions involves utilizing the ^{176}Lu–^{176}Hf isotopic systematics of apatite, which is a relatively common accessory mineral in mafic-ultramafic rocks. Apatite preferentially incorporates rare earth elements (REE) and contains little Hf (typically $\ll$1 ppm) (e.g., Fujimaki 1986). Barfod et al. (2003) presented a method for the separation of Lu and Hf from apatite that allows for rapid sample processing prior to analysis by multiple collector-inductively coupled plasma-mass spectrometry (MC-ICP-MS). When applied to a sample from Upper Zone b of the Skaergaard intrusion, isotopic data from three apatite fractions and the whole rock yield an isochron with a precise Lu–Hf age of 58.28 ± 0.44 Ma (Barfod et al. 2003: decay constant of ^{176}Lu of 1.869×10^{-11} year^{-1} from Scherer et al. 2001) (Fig. 1.3d). The Lu–Hf isochron is older than the recently published U–Pb zircon age of 55.960 ± 0.018 Ma (Wotzlaw et al. 2012), perhaps the result of disturbance of the original Lu–Hf systematics, but nonetheless demonstrates the potential for determining precise ages of layered intrusions from apatite when zircon is not present in the samples of interest.

U–Th–Pb Geochronology

The U–Th–Pb dating method has been a longstanding geochronological tool for the last 100 years, with significant improvements being made in the last 50 years, and has been used to determine the ages of U- and Th-bearing accessory minerals in rocks representing the span of Earth history (e.g., Parrish and Noble 2003; Mattinson 2013; Schoene 2014), including the vast majority of dated layered intrusions (Table 1.1). U–Th–Pb geochronology is based on the decay (parent to daughter) of the long-lived radioactive isotopes ^{238}U to ^{206}Pb, ^{235}U to ^{207}Pb, and ^{232}Th to ^{208}Pb where the Pb is referred to as radiogenic (i.e., Pb*); a fourth Pb isotope, ^{204}Pb, is stable and has no radioactive parent. From each of these decay systems, an independent age can be determined following isotopic measurements of the mineral of interest (e.g., zircon, monazite, baddeleyite, rutile) with knowledge of the decay constants of ^{238}U, ^{235}U, and ^{232}Th, an assumed present-day ^{238}U/^{235}U isotopic composition (Condon et al. 2010; Hiess et al. 2012), and the initial or common Pb present (i.e., Pb$_c$), which is the nonradiogenic Pb that occurs in the mineral upon crystallization or Pb introduced during sample processing in the laboratory (e.g., Dickin 2005; Faure and Messing 2005). A ^{207}Pb/^{206}Pb date can be calculated by combining

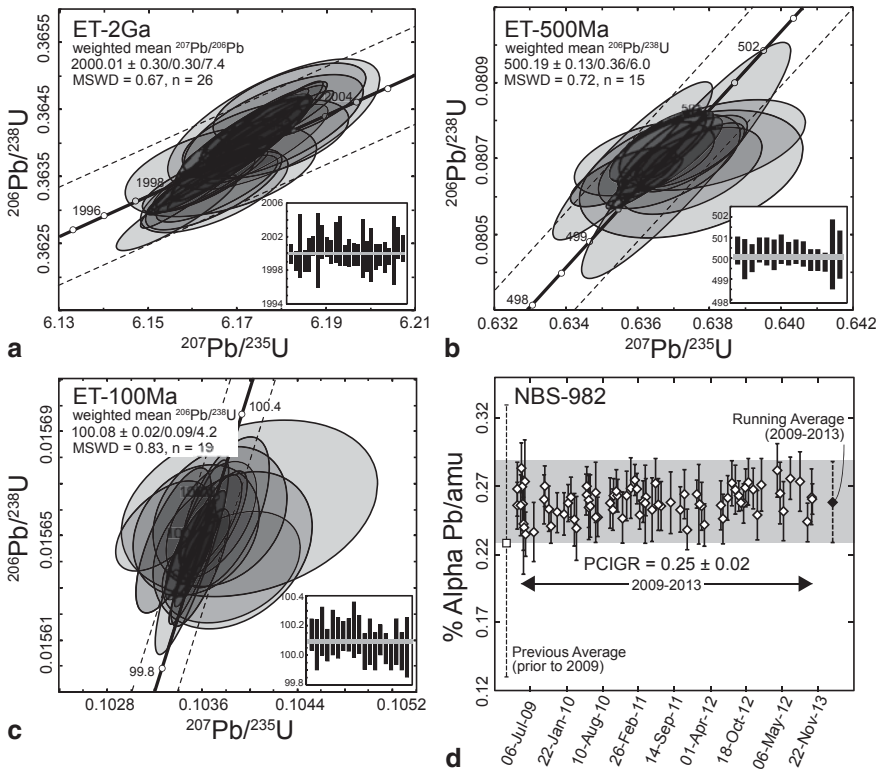

Fig. 1.4 Plots showing results for standard analyses at PCIGR (UBC) since early 2009. **a** Concordia diagram showing U–Pb results for the EARTHTIME 2 Ga synthetic solution (ET-2 Ga). **b** Concordia diagram showing U–Pb results for the EARTHTIME 500 Ma synthetic solution (ET-500 Ma). **c** Concordia diagram showing U–Pb results for the EARTHTIME 100 Ma synthetic solution (ET-100 Ma). The U–Pb errors are reported in the ± X/Y/Z format of Schoene et al. (2006) with internal error in the absence of all systematic errors (± X), tracer calibration error (± Y), and uncertainty due to decay-constant errors (± Z), which is used for comparison with other isotopic geochronometers (e.g., $^{40}Ar/^{39}Ar$). The *dashed* lines indicate the error bounds of the Concordia curve. The inset shows the $^{207}Pb/^{206}Pb$ ages for individual analyses for ET-2 Ga in panel **a** and the $^{206}Pb/^{238}U$ ages for panels **b** and **c**; the *grey horizontal* lines correspond to the weighted mean ages for each synthetic solution. **d** Fractionation factor, alpha (%/amu), from measurements of $^{208}Pb/^{206}Pb$ for 66 analyses of the NBS-982 Pb standard over nearly 5 years (2009–2013). The *dark grey* band shows the average value (0.25 ± 0.02, 2s) compared the previous value (0.23 ± 0.05, 2s) used at PCIGR

the daughter isotope determinations from the two uranium decay systems. For visualization, U–Pb results are most commonly presented on a Wetherill concordia diagram (Wetherill 1956), which plots $^{207}Pb^*/^{235}U$ vs. $^{206}Pb^*/^{238}U$ from the same analyses (e.g., Figs. 1.1e, 1.4a, b, and c). The concordia curve represents the locus of points of equal age from the two different uranium decay schemes and is non-linear due to the different half-lives of ^{238}U (4.468×10^9 years or 4.468 Ga) and ^{235}U (7.038×10^8 years or 703.8 Ma) (Jaffey et al. 1971). Concordant U–Pb results (i.e.,

$^{207}Pb^*/^{235}U$ age = $^{206}Pb^*/^{238}U$ age) for an analysis indicate that the sample (i.e., mineral) has remained a closed system since the time of formation (see analyses B3 and B6 on Fig. 1.1e). U–Pb results that do not lie on concordia are referred to as being discordant (see analyses B2, B5, and B1 on Fig. 1.1e) and result from open-system processes at some point after formation. This can include a variety of processes, but is most commonly attributed to Pb loss and mixing of materials with different ages (e.g., inheritance of older grains, metamorphic overgrowths). Background information on the most commonly used analytical methods (ID-TIMS, SIMS, LA-ICP-MS), pretreatment protocols for zircon analysis, and community-wide innovations spurred on by EARTHTIME is provided in the following sub-sections because of the importance of U–Th–Pb geochronology in determining the ages of layered intrusions.

Isotope Dilution-Thermal Ionization Mass Spectrometry

U–Pb geochronology using isotope dilution-thermal ionization mass spectrometry (ID-TIMS) is by far the most precise analytical technique with average precisions now reported from most laboratories on single zircons of ~0.2% of the reported date and some laboratories achieving significantly higher precision (<0.1%) (Schoene 2014). Comprehensive summaries of the history and application of TIMS to U–Th–Pb geochronology can be found in Davis et al. (2003) and Parrish and Noble (2003). Briefly, in ID-TIMS, minerals selected for dating after standard mineral separation procedures are spiked with a tracer solution, dissolved in Teflon vessels using HF or HCl, and U and Pb are chemically separated from other elements using ion exchange chromatography (Krogh 1973; Davis et al. 2003; Parrish and Noble 2003). Addition of a mixed U–Pb isotopic tracer of known composition and quantity, or isotope dilution, allows for correction of elemental fractionation during analysis on a mass spectrometer and determination of precise isotopic ratios as well as elemental abundances. The separated sample containing U and Pb after column chemistry is placed on a metal filament (e.g., Re), which is heated under vacuum in the source of the TIMS to ionize both U and Pb with the ions then accelerated into and analyzed by a magnetic sector mass spectrometer (Parrish and Noble 2003; Schoene 2014). The method is highly accurate and precise with very stable beams and measurement times of 2–3 h per sample, which are substantially longer than those for in situ techniques described below (e.g., SIMS, LA-ICP-MS). The vast majority of the reported ages for layered intrusions worldwide are based on the ID-TIMS methods for U–Th–Pb geochronology (Table 1.1).

Pretreatment Methods for Zircon

Zircon ($ZrSiO_4$) is the most widely used U–Th–Pb-bearing mineral in geochronology (e.g., Davis et al. 2003; Parrish and Noble 2003, and references therein) due to its presence in a wide range of igneous, metamorphic, and sedimentary rocks,

to its stability under crustal and upper mantle conditions, and to its high closure temperature for diffusion of Pb (> 1000 °C, Cherniak and Watson 2000). Zircon is, however, susceptible to radiation damage (e.g., Holland and Gottfried 1955; Ewing et al. 2003). The crystal structure can become metamict through self-irradiation from alpha recoil during the decay of U and Th, which produces defects in the crystal lattice and amorphous material (Rios et al. 2000). Such amorphous zones can be linked along microcracks to form passages that allow Pb (the daughter product of U and Th) to be lost from the crystal during interaction with hydrothermal or metamorphic fluids (e.g., Rios et al. 2000; Geisler et al. 2003; Nasdala et al. 2005), resulting in significant discordance of U–Pb results and young apparent U–Pb ages. A major issue in U–Pb geochronology has long been the identification and removal of Pb-loss zones in zircon (e.g., Tilton et al. 1957; Silver and Deutsch 1963; Krogh and Davis 1974). The technique of Krogh (1982a, b) allowed for removal of the outer, U + Th-rich layer of zircon crystals by air abrasion and for the determination of precise, concordant U–Pb results after careful grain selection. The more recently developed chemical abrasion technique (CA-TIMS) of Mattinson (2005) allows for removal of zircon domains that have lost Pb from the interior of grains and the analysis of low-U + Th, closed system residues with both concordant results and ages with significantly improved accuracy. For low to moderately damaged zircon, annealing and leaching is effective at removing altered discordant domains in zircon and the technique allows for determination of ages with a high degree of concordance. For highly damaged zircon, especially high-U Precambrian zircon, it may not be possible to fully restore primary U–Pb ages under any annealing conditions (Das and Davis 2010). The CA-TIMS technique provides very robust results for determining ages of layered intrusions to high precision and accuracy, although relatively few studies have reported U–Pb zircon CA-TIMS ages to date (Table 1.1).

Isotope Tracers, Synthetic Solutions, and Standards

The "EARTHTIME Initiative", initiated in 2003 with the goal of sequencing Earth history throughout geologic time by producing a highly resolved, calibrated geologic timescale, has been instrumental in spearheading significant improvements in high-precision geochronology (Bowring et al. 2011; Schmitz and Kuiper 2013). One of the main goals of EARTHTIME is to stimulate cooperation and intercalibration of U–Pb and $^{40}Ar/^{39}Ar$ laboratories worldwide through the use of common enriched isotope tracer solutions, or spikes, and synthetic Pb–U isotope solutions. A new ^{205}Pb –^{233}U –^{235}U spike (ET535) was made available to U–Pb labs, including the Pacific Centre for Isotopic and Geochemical Research (PCIGR) at the University of British Columbia (Vancouver, Canada) where the analyses in this study were conducted (Table 1.2), provided they met certain criteria following an international quorum with the different labs analyzing a range of reference materials. Another tracer that is available from EARTHTIME is the ^{202}Pb –^{205}Pb –^{233}U –^{235}U (ET2535) spike, which allows for in-run correction of instrumental Pb fractionation instead of relying on an external correction from repeat analyses of a Pb standard (e.g.,

Table 1.2 U–Pb geochronologic analytical techniques and protocols at PCIGR (UBC)

Variable	Pre-2008	Post-2008
Mass spectrometer	VG54R single collector, analog Daly	VG354S single collector, Sector 54 electronics, analog Daly
Pyrometer	Analog optical	Digital optical
Data collection	Peak-hopping on Daly, RL Armstrong (unpubl.)	Micromass Sector 54 IR software; employs Dodson (1978) 2nd-degree interpolation (release 3.977)
Spike	Parrish (1987) ^{205}Pb–$^{233–235}U$ spike	EARTHTIME 535 ^{205}Pb–$^{233–235}U$ spike
Pb standard	NBS-982	NBS-982
Reference	R33 zircon + others	EARTHTIME 100Ma, 500Ma, 2Ga synthetic solutions
Pb blanks	1.4–9 pg	0.4–1.7 pg
Data reduction	HTB—Roddick (1987)	Tripoli + U-Pb_Redux (Bowring et al. 2011) & UPbr (Schmitz and Schoene 2007)

NBS-981) and thus improved precision of $^{207}Pb/^{206}Pb$ ages. Using the same isotopic tracer allows for the direct comparison of analyses between labs without having to propagate errors related to spike calibrations and thus effectively eliminates interlaboratory bias due to tracer calibration.

Another major component of EARTHTIME intercalibration process was the production of synthetic U-Pb solutions with concordant isotopic compositions and elemental ratios (corresponding to 10 Ma, 100 Ma, 500 Ma, and 2 Ga) for distribution between various U–Pb labs to monitor long-term mass spectrometer performance (Condon et al. 2007; Schmitz and Kuiper 2013). The solutions were prepared by iterative mixing of natural uranium (SRM 950a), ^{206}Pb (SRM 991) and ^{207}Pb (metal from Cambridge Isotopes) solutions. Determination of the ^{206}Pb –^{238}U and ^{207}Pb –^{235}U ratios is being achieved via calibration against the ET535 tracer. As these solutions are pure U and Pb, they do not require any chemical purification, thus the U–Pb loads can be prepared by mixing in a pre-cleaned beaker, which means that exposure to laboratory blank and effort in preparing loads is greatly reduced compared to using a mineral standard. These solutions have the potential to replace natural mineral standards (e.g., R33, Temora) for ID-TIMS, allowing for a more accurate evaluation of mass spectrometry behaviour because post-crystallization Pb-loss and natural compositional variation observed in zircon are not factors. PCIGR has been analyzing three synthetic U–Pb solutions since 2009 with the following results: ET-2 Ga, weighted mean $^{207}Pb/^{206}Pb$ date = 2000.01 ± 0.30 Ma (uncertainty quoted at 2s with internal errors); ET-500 Ma, weighted mean $^{206}Pb/^{238}U$ date = 500.19 ± 0.13 Ma; ET-100 Ma, weighted mean $^{206}Pb/^{238}U$ date = 100.08 ± 0.02 Ma (Figs. 1.4a, b, and c).

Additional outgrowths of EARTHTIME include the development of common, open-source software platforms or cyber infrastructure in data collection and analysis (Tripoli and U–Pb_Redux; Bowring et al. 2011; McLean et al. 2011) and derivation of isotope ratios, errors, and error correlations for U–Pb geochronology using

the mixed ET535 (or ET2535) tracer (Schmitz and Schoene 2007), which are now in use at PCIGR. Other areas of potential analytical improvement include the characterization of Pb fractionation during thermal ionization mass spectrometry, which is the largest source of uncertainty in $^{207}Pb/^{206}Pb$ ages when analyzing Archean zircon grains due to the high amounts of Pb per analysis (can be over 1 ng). Over the past 5 years at PCIGR, we have characterized the Pb fractionation value of the commonly used Pb standard NBS-982 based on the $^{208}Pb/^{206}Pb$ and $^{207}Pb/^{206}Pb$ isotopic ratios measured on a VG354S single collector mass spectrometer with Sector 54 electronics and an analog Daly (Table 1.2). The calculated Pb fractionation value for 66 analyses is 0.25 ± 0.03 %/amu (2s, error based on $^{208}Pb/^{206}Pb$ as these are the most abundant isotopes for NBS-982) (Fig. 1.4d), which means that uncertainties as low as 0.02 % are now achievable provided all other sources of uncertainty (e.g., Pb blanks) are kept at a minimum (Table 1.2). An additional way to reduce analytical uncertainty related to Pb fractionation, even in sub-nanogram sample loads, is through the use of a double Pb spike (e.g., ^{202}Pb–^{205}Pb, Amelin and Davis 2006) or the mixed ET2535 tracer. Collectively, these improvements provide the opportunity to discriminate different magmatic episodes in the crystallization sequences of layered intrusions.

In Situ Methods (SIMS, LA-ICP-MS)

In addition to high-precision TIMS analysis using the chemical abrasion pretreatment technique, modern U–Th–Pb geochronology has been revolutionized by the advent of high-spatial resolution isotope analyses by secondary ionization mass spectrometry (SIMS) and laser ablation inductively coupled plasma mass spectrometry (LA-ICP-MS) (e.g., Ireland and Williams 2003; Nemchin et al. 2013). These in situ techniques allow for the determination of isotopic ratios from within single zones of crystals at scales of tens of microns that can target areas with distinctive textural, chemical, and isotopic signatures. The number of minerals than can be analyzed for U–Th–Pb geochronology by in situ methods is rapidly expanding and includes zircon, monazite, xenotime, apatite, titanite, baddeleyite, rutile, pervokskite, and allanite.

In a SIMS instrument, or ion microprobe (e.g., SHRIMP, CAMECA), a beam of high-energy primary ions (e.g., oxygen) is focused onto a polished target sample and a small amount of material is sputtered, typically with dimensions of 10–50 microns in diameter and less than 5 microns depth. Secondary ions are produced during sputtering and they are analyzed in the mass spectrometer (Ireland and Williams 2003). The SIMS technique is effectively non-destructive and ideal for analyzing complexly zoned zircon and for distinguishing the ages of inherited cores and magmatic and metamorphic overgrowths. The SHRIMP, or sensitive high-resolution ion microprobe, was specifically designed for the U–Th–Pb geochronology of zircon and the first results were reported in the early 1980s (e.g., Williams et al. 1983; Compston et al. 1984). In a LA-ICP-MS instrument, high intensity photons or laser radiation of uniform wavelength (e.g., 213- and 193-nm), phase, and polarization

interact with a solid sample, which results in vaporization and ablation of atoms, ions, molecules, melt, and solid particles (e.g., Kosler and Sylvester 2003; Chang et al. 2006; Frei and Gerdes 2009; Fisher et al. 2010). This material is then introduced into an ICP-MS and isotope ratios analyzed by mass spectrometry. Compared to SIMS, the LA-ICP-MS technique involves destruction and removal of more material with typical spot sizes of 30–60 microns and depths of 10–20 microns, although recent studies are demonstrating successful application of single shot laser ablation analysis with small spot sizes (down to 6 microns) (Cottle et al. 2009, 2012). The availability, lower capital cost of the instrumentation compared to TIMS and SIMS, and the capability of obtaining ages from 100s of unknowns in a single analytical session has resulted in widespread application of U–Pb dating by LA-ICP-MS over the past 5–10 years (Fisher et al. 2010).

For geochronologic applications, both SIMS and LA-ICP-MS require comparison of measured values from a sample with those from matrix-matched reference materials that have been previously determined, typically from ID-TIMS or solution multiple collector-ICP-MS. As a result, the precision and accuracy of the analyses is limited to the precision and accuracy of the elemental ratios of interest in the reference materials being used with achievable precision typically not better than 2 % at the 2s level (Nemchin et al. 2013). Analyses by in situ techniques must also be designed to deal with changes in the measured isotopic ratios with time (e.g., sputtering-related changes in secondary ion emissions by SIMS, Ireland and Williams 2003; laser-induced fractionation of U relative to Pb by LA-ICP-MS, Fisher et al. 2010). The lack of chemical preparation, the ability to rapidly collect data, and the capability of determining age variations within mineral grains and structurally complex minerals make in situ analyses an essential dating technique where the scale of mineral (and age) heterogeneity is of concern. These techniques have as yet seen little application in dating the age of layered intrusions (Table 1.1) given the relatively high uncertainty compared to ID-TIMS (~2 % vs. < 0.1 %) and typically simple zircon morphologies encountered (see below).

$^{40}Ar/^{39}Ar$ Geochronology

The $^{40}Ar/^{39}Ar$ dating method is a widely applicable and precise method of geochronology, with relative precision better than 0.1 % in many cases, that has been used to calibrate Cenozoic time scales, determine the age of emplacement of volcanic rocks, and constrain the cooling path of plutonic and metamorphic rocks (e.g., Renne et al. 1998; McDougall and Harrison 1999; Renne et al. 2010). $^{40}Ar/^{39}Ar$ dating, based on the ^{40}K–^{40}Ar method (i.e., decay of ^{40}K to ^{40}Ar), is applied to K-bearing minerals or rocks in which potassium is an essential structural constituent (e.g., micas, feldspars) or present in limited amounts (e.g., amphibole, < 1 % K) (Harrison and Zeitler 2005). An $^{40}Ar/^{39}Ar$ date requires calculation of a $^{40}K/^{39}Ar$ ratio from isotopic measurements after a sample has been irradiated with fast neutrons to transform a proportion of the ^{39}K atoms to ^{39}Ar. A standard sample of known age (e.g., 28.305 ± 0.036 Ma Fish Canyon sanidine, Renne et al. 2010) is irradiated together

with the unknown sample and the age of the unknown is derived by comparison with the $^{40}Ar/^{39}Ar$ of the standard (Harrison and Zeitler 2005). Systematic errors in the $^{40}Ar/^{39}Ar$ method arise from imprecise K and Ar isotopic data for standards and from uncertainties in ^{40}K decay constants (Renne et al. 1998; Min et al. 2000). When data pairs of $^{206}Pb/^{238}U$ and conventional $^{40}Ar/^{39}Ar$ ages are compared from the same samples, a systematic bias of older U–Pb ages is observed ranging from > 1.5 % for young rocks (Phanerozoic) to 0.5 % for rocks as old as 2 Ga (e.g., Renne et al. 2010, 2011). It is now possible to reconcile the two isotopic systems (Smith et al. 2010) by using the revised age for the Fish Canyon standard (Kuiper et al. 2008).

$^{40}Ar/^{39}Ar$ geochronology has been most successfully applied to young (Phanerozoic) intrusions, such as the Paleogene mafic layered intrusions related to the North Atlantic Igneous Province (e.g., Skaergaard, Kap Edvard Holm, Rum), where post-crystallization hydrothermal alteration and metamorphism have not resulted in open-system behavior. Hirschmann et al. (1997) reported the first precise date for the Skaergaard intrusion based on hornblende (55.48 ± 0.30 Ma) and biotite (55.40 ± 0.14 Ma) from a Transgressive granophyre from Upper Zone a of the Layered Series (Table 1.1) and used these cooling ages to evaluate the cooling history of the intrusion and the timing of the Skaergaard intrusion relative to eruption of the East Greenland basalts. Hamilton et al. (1998) reported the first precise dates from the Rum intrusion (Isle of Rum, Hebrides) from combined U–Pb zircon (60.53 ± 0.08 Ma: marginal alkaline segregation) (Table 1.1) and $^{40}Ar/^{39}Ar$ phlogopite (60.1 ± 1.0 Ma: gabbro pegmatite) systematics. These results indicated rapid cooling of the Rum intrusion and were used to calculate magma production rates for the Skye volcanic centre comparable to those for magmatism above upwelling mantle plumes such as Hawaii. $^{40}Ar/^{39}Ar$ geochronological results from Tegner et al. (1998) for plagioclase, biotite, amphibole, and whole rocks from a wide range of East Greenland layered intrusions document their ages of emplacement allowing for the recognition of discrete mantle melting episodes, the timing of coeval flood basalt magmatism and continental breakup, and even the potential links between massive outpourings of basalt and environmental impacts (e.g., Paleocene-Eocene Thermal Maximum, Storey et al. 2007).

U–Th–Pb-bearing Minerals in Layered Intrusions

U–Pb geochronology involves determination of ages for U–Th–Pb-bearing minerals (e.g., zircon, baddeleyite, monazite, titanite) to constrain timing of a wide range of geological events from magma crystallization to metamorphism to hydrothermal activity throughout all of geological history (e.g., Heaman and Parrish 1991; Davis et al. 2003; Parrish and Noble 2003). These accessory minerals are characterized by variable U concentrations, the amount of common Pb incorporated during crystallization, and closure temperatures (Table 1.3). Closure temperature is a complex function involving diffusivity of the element of interest (i.e., Pb), effective grain radius, which may not be the same as grain size, and cooling rate (Dodson 1973). For the U–Th–Pb-bearing minerals typically encountered in layered intrusions

Table 1.3 Geochemical characteristics of dateable accessory minerals in layered intrusions

Mineral	Chemical Formula	Closure Temperature (°C)	U Concentration (ppm)	Common Pb (ppm)	References
Zircon	$ZrSiO_4$	>950	1 to >10,000	<2	Cherniak and Watson (2000, 2003); Belousova et al. (2002)
Baddeleyite	ZrO_2	>950	1 to >3000	<2	Heaman and LeCheminant (1993, 2000)
Monazite	$(Ce,La,Nd,Th)PO_4$	>750	100–1000	<2	Cherniak (2010)
Titanite	$CaTiSiO_5$	600–650	20–1000	0.2–10	Frost et al. (2000); Cherniak (2010)
Apatite	$Ca_5(PO_4)_3(F,Cl,OH)$	425–500	8–100	<5–800	Cherniak (2000); Chamberlain and Bowring (2000)
Rutile	TiO_2	400–450	<<1–400	<2–100	Schmitz and Bowring (2003)

(Table 1.3), closure temperatures range from ~1000 °C down to 400 °C, which allows for the possibility of determining integrated crystallization and cooling ages. Key geochronological characteristics of the most common, and not so common, U–Th–Pb-bearing minerals that may be present in layered intrusions and indicate both successful and potential dating applications are briefly outlined below.

Zircon

Zircon, $ZrSiO_4$, a common accessory mineral occurring in a wide variety of terrestrial rocks (igneous, metamorphic, sedimentary) and extraterrestrial rocks (meteorites, lunar rocks, tektites), is one of the most widely used minerals for geochronology. Zircon is a refractory mineral and easily separated from crushed rock samples due to its high density ($\rho = 4.6–4.7$ g/cm^3) and hardness (H = 7.5). Zircon incorporates a wide range of trace elements with large ionic radii, including the heavy rare earth elements, Nb, Ta, Hf, and the actinides, U and Th (Belousova et al. 2002; Finch and Hanchar 2003). A fundamental aspect for geochronological applications is the incorporation of U (typical range of 10–1000 ppm) and Th (1–100 ppm) into the zircon structure during crystallization and the preferential exclusion of Pb (Parrish and Noble 2003) (Table 1.3) such that the Pb accumulated in zircon over time from the radioactive decay of parent U and Th isotopes is considered as radiogenic Pb (i.e.,

Pb*). The closure temperature for Pb diffusion in zircon is in excess of 950–1000 °C (Cherniak 1993, 2010; Cherniak and Watson 2000, 2003), which corresponds to the temperature range estimated for near-solidus conditions in layered intrusions (e.g., Lindsley et al. 1969; Morse 2008) based on experimental and field-based studies. Lead diffusion in crystalline zircon is so slow at geologically reasonable temperatures in the crust that Pb-loss cannot be attributed to volume diffusion through its crystal lattice, but rather is related to more rapid diffusion in metamict zircon that has been radiation-damaged during decay of U + Th through the release of a low-energy, but heavy, alpha-recoil nucleus (daughter isotope) or a high-energy, and light, alpha-particle (He nucleus) (Cherniak and Watson 2003; Geisler et al. 2007). Primary magmatic zircon can also be replaced by secondary hydrothermal zircon with significant elemental gains and losses, including both U and Pb (Ewing et al. 2003; Geisler et al. 2003, 2007; Nasdala et al. 2005) with important implications for zircon geochronology. Fortunately, careful grain examination during selection under a binocular microscope coupled with imaging by cathodoluminescence and backscattered electron techniques (e.g., Corfu et al. 2003) can be used to identify zircon that may not record primary crystallization ages. As noted previously, zircon is the mineral of choice for high-precision geochronology of layered intrusions (Table 1.1) given its relative abundance amongst all dateable accessory minerals, high U/Pb ratio upon crystallization, and high closure temperature similar to the temperatures of crystallization of zircon from late-stage, fractionated interstitial melt in mafic-ultramafic cumulates. In addition, heavy mineral separates from mafic-ultramafic rocks tend to be dominated by a single population of zircon without evidence for inheritance of zircon from earlier intrusive phases and are characterized by relatively simple zoning patterns. These grains do not typically record the complex, multi-stage crystallization histories that are so commonly preserved in zircon found in granitoids and other felsic rocks.

Baddeleyite

Baddeleyite, ZrO_2, occurs in many terrestrial and lunar rocks, and some meteorites, and is the mineral with the highest potential for U–Pb dating in mafic dikes and high-level mafic sills (Heaman and LeCheminant 1993). In mafic rocks, it is found in the late-stage, chemically fractionated regions with K-feldspar, mica, amphibole, and small amounts of quartz (Heaman and LeCheminant 1993). Baddeleyite is ideal for U–Pb dating yielding concordant high-precision ages due to the abundant U incorporated into the crystal lattice (generally < 1500 ppm, but up to 3000 ppm), negligible initial common Pb, and an apparent high U–Pb closure temperature similar to that of zircon (Heaman and LeCheminant 1993, 2000; Lumpkin 1999) (Table 1.3). Baddeleyite has become a major tool for dating mafic rocks, especially dike swarms associated with large igneous provinces, and the resultant ages provide important constraints on supercontinent reconstructions and mantle dynamics (e.g., Ernst and Buchan 2001; Söderlund et al. 2010). The newly developed in situ U–Pb SIMS technique for dating micro-baddeleyite needles (< 10–40 μ long by a

few microns wide), which are difficult to recover with conventional concentration techniques, now allows for non-destructive dating with precisions ranging from 0.1% for Precambrian rocks to 3–7% for Phanerozoic rocks (Chamberlain et al. 2010; Schmitt et al. 2010). Post-crystallization Pb loss and intergrowth of baddeleyite and zircon resulting in discordant results has been documented (Heaman and LeCheminant 1993; Rioux et al. 2010). Recent advances in multi-step digestion have been used successfully to isolate magmatic baddeleyite from secondary zircon inter- and overgrowths so that igneous and subsequent hydrothermal or metamorphic events can now be resolved (Rioux et al. 2010). Discordance in baddeleyite may also involve several isotope-specific mechanisms, including (1) ^{206}Pb deficit due to disequilibrium in Th/U (i.e., low Th in baddeleyite), (2) ^{207}Pb excess from protactinium (Amelin and Zaitsev 2002), and (3) preferential loss of ^{206}Pb from radon loss (Davis and Sutcliffe 1985; Heaman and LeCheminant, 2000). Application of U–Pb baddeleyite dating to layered intrusions is still relatively restricted (e.g., Poe Mountain, Scoates and Chamberlain 1995; Muskox intrusion, Mackie et al. 2009, Fig. 1.1; Ilimaussaq, Krumrei et al. 2006; Sonju Lake, Paces and Miller 1993) as zircon is the principal Zr-bearing phase recovered and dated from layered intrusions worldwide (Table 1.1).

Apatite

Apatite, $Ca_5(PO_4)_3(F,Cl,OH)$, is a common accessory mineral in many igneous rocks, including mafic-ultramafic rocks in layered intrusions (e.g., Poe Mountain intrusion, Fig. 1.2f) where it ranges in composition from fluorapatite-hydroxylapatite in most cumulates to anomalous chlorapatites in the sequences below the PGE reefs in both the Stillwater and Bushveld complexes (e.g., Boudreau et al. 1986; Boudreau and Hoatson 2004). Apatite is a relatively low-U mineral (<100 ppm), with lattice-bound U and Pb, and closure temperatures to Pb diffusion in the range of 425–500 °C (Cherniak et al. 1991; Chamberlain and Bowring 2000) (Table 1.3), depending on diffusion radii and cooling rates. These characteristics make apatite an important thermochronometer for investigating the cooling history of layered intrusions, however, there are as yet few studies that exploit its potential. Because apatite can accommodate significant amounts of initial Pb in its crystal structure, the ratio of radiogenic Pb to common Pb can be very low and thus the accuracy and precision of U–Pb apatite ages requires careful selection of initial Pb isotopic compositions in age calculations (e.g., co-existing feldspar) (Chamberlain and Bowring 2000).

Rutile

Rutile, TiO_2, is the most common naturally occurring titanium dioxide polymorph and is found in a wide range of rocks as an accessory mineral, including granitoids, metamorphic rocks, mantle rocks, and meteorites (Meinhold 2010). Rutile

is a major host for Nb, Ta, and other high field strength elements and it contains sufficient U (up to 100 ppm) making precise U–Pb geochronology possible (e.g., Mezger et al. 1989; Luvizotto et al. 2009). However, rutile can incorporate significant non-radiogenic or common Pb during crystallization (Table 1.3). This common Pb must be corrected for either by analyzing a coexisting leached feldspar for common Pb (Mezger et al. 1989), using a Pb growth model (Stacey and Kramers 1975), or using the measured $^{238}U/^{206}Pb$ and $^{207}Pb/^{206}Pb$ ratios (Tera and Wasserburg 1972). The closure temperature to Pb diffusion in rutile is variable. Experimental Pb diffusion data for rutile from Cherniak (2000, 2010) indicate relatively high temperatures (600–700 °C), whereas field-based studies indicate lower temperatures (400–450 °C) when compared to co-existing U–Pb and $^{40}Ar/^{39}Ar$ chronometers (Mezger et al. 1989; Schmitz and Bowring 2003).

In igneous rocks, rutile is most commonly found in granites and associated quartz veins, pegmatites, carbonatites, kimberlites, and metallic ore deposits (Meinhold 2010). Rutile is rarely reported in layered intrusions. It has however been noted throughout the Critical Zone of the Bushveld Complex (Cameron 1979), mostly associated with chromite and as inclusions in plagioclase and orthopyroxene. It is present in bronzitites, orthopyroxenites, of the Great Dyke (Oberthür et al. 2002), where interstitial quartz, K-feldspar, and phlogopite are present, the latter containing inclusions of coarse rutile. We have observed that rutile is a common accessory in many ultramafic and mafic cumulates from both the Stillwater Complex and Bushveld Complex. U–Pb geochronological studies of rutile from layered intrusions are rare. Metamorphic rutile ages (~650 Ma) are reported for the Niquelandia layered intrusion in central Brazil (Ferreira-Filho et al. 1994). To our knowledge, only two studies provide U–Pb rutile dates for magmatic rutile from layered intrusions: (1) a 2575.0 ± 1.0 Ma age from sulphide-bearing bronzitites of the Main Sulphide Zone of the Great Dyke, which overlaps within uncertainty the U–Pb zircon age of 2575.9 ± 1.0 Ma from the same sample (Oberthür et al. 2002), and (2) a 2055.0 ± 3.9 Ma age from the Merensky Reef of the Bushveld Complex, where rutile occurs mainly as inclusions within or overgrowths on chromite, especially in the chromitite stringers that bound the reef, and also as acicular grains with biotite (Scoates and Friedman 2008).

Titanite

Titanite, $CaTiSiO_5$, is a U–Pb-bearing mineral that is commonly found in mafic and calc-silicate metamorphic rocks and in relatively oxidized igneous rocks (Frost et al. 2000). Titanite is useful for U–Pb dating as U concentrations in igneous rocks vary from 10s to 100s of ppm, which combined with relatively low 0.2–10 ppm common Pb (Table 1.3) allows for the possibility of determining high-precision U–Pb ages (Frost et al. 2000). The closure temperature to Pb diffusion in titanite is high (> 600 °C; Cherniak 1993, 2010) making it a valuable chronometer for reconstructing the high-temperature cooling history of intrusions. U–Pb titanite dating has been successfully applied to ancient and young felsic rocks, ranging from Ar-

chean granitoids (Corfu et al. 1985) to the ca. 28 Ma Fish Canyon Tuff (Hemming and Rasbury 2000; Chew et al. 2014). There are as of yet few published studies using U–Pb titanite for dating layered intrusions, although titanite may be a relatively common mineral in late-stage granophyric segregations that occur locally in many intrusions (e.g., Stillwater granophyres, Wall 2009). A notable exception is the Bushveld Complex where Buick et al. (2001) reported a U–Pb titanite age of 2058.9 ± 0.8 Ma (weighted mean $^{207}Pb/^{206}Pb$ age of three multigrain fractions) from a hydrothermally retrogressed calc-silicate xenolith in the Upper zone of the Bushveld Complex. Assuming that fluid flow and titanite growth in the xenolith were directly related to Bushveld magmatism, they proposed that this metamorphic titanite age restricted crystallization of the layered mafic-ultramafic rocks of the Bushveld Complex to the interval of 2059–2061 Ma.

Other Minerals

Two other minerals that have been identified in mafic-ultramafic rocks may also be potential U–Pb chronometers. Zirconolite, $CaZrTi_2O_7$, is a rare U-bearing oxide mineral that has been reported in lunar basalts and meteorites, in silica undersaturated alkaline rocks, in mafic dikes, and in a few layered intrusions (Heaman and LeCheminant 1993; Rasmussen and Fletcher 2004; Zaccarini et al. 2004). Zirconolite from mafic intrusions in Australia typically occurs as euhedral laths and needles (< 200 microns long and < 20 μ wide), is light tan to dark brown to opaque, and contains several wt% $UO_2 + ThO_2$ and up to 15 wt% combined REE (Rasmussen and Fletcher 2004). U–Pb SHRIMP dating of zirconolite from mafic and lunar rocks shows that it typically contains minimal common Pb and can produce precise and tightly grouped $^{207}Pb/^{206}Pb$ dates due largely to the high ionization efficiency for Pb^+(Rasmussen and Fletcher 2004; Norman and Nemchin 2014). Loveringite, $(Ca,Ce)(Ti,Fe,Cr,Mg)_{21}O_{38}$, a U-bearing Ca-end-member of the crichtonite group, was discovered in orthopyroxene-rich cumulates of the Jimberlana intrusion, Western Australia (Gatehouse et al. 1978), and has been found in gabbroic cumulates from ophiolites (Cabella et al. 1997) and in some layered intrusions in Finland and Russia (e.g., Koitelainen, Tarkian and Mutanen 1987; Penikat, Alapieti 1982; Barkov et al. 1996). In the Jimberlana intrusion, loveringite is black, occurs as rare anhedral to needle-like grains (50 × 100 microns), is closely associated with quartz, K-feldspar, or phlogopite, and contains 0.18–0.34 wt% UO_2 and 0.09–0.53 wt% ThO_2 (Campbell and Kelly 1978). There are as yet no published U-Pb geochronological determinations of loveringite. It is possible that both zirconolite and loveringite are more widespread in layered intrusions than their documented occurrences suggest, however, their very fine grain size, trace abundance, and morphological similarities to rutile and baddeleyite to date hinder their routine separation and identification.

Sampling Strategy for Dateable Accessory Minerals in Layered Intrusions

Previous Geochronologic Investigations of the Stillwater Complex

Using the Stillwater Complex as a test case, we describe the criteria to successfully identify samples in mafic-ultramafic cumulates in layered intrusions that are likely to yield small quantities of dateable accessory minerals. The Stillwater Complex is a large fragment of a mafic-ultramafic layered intrusion in the Beartooth Range (Montana, USA) of the Archean Wyoming Province (Fig. 1.5a) and represents a crystallized sub-volcanic magma chamber that fed voluminous volcanic rocks (Hess 1960; Jackson 1961; McCallum, 1996). From base-to-top, the intrusion is subdivided into the thin Basal Series, the 2000 m-thick Ultramafic Series with a lower Peridotite Zone and upper Bronzitite Zone, and the overlying Banded Series, which consists of the Lower Banded Series (host to the PGE-rich J-M Reef horizon), Middle Banded Series, and Upper Banded Series (Fig. 1.5b). Determining the precise age of crystallization of the Stillwater Complex has been the focus of studies since the late 1960s (e.g., Fenton and Faure 1969; Nunes and Tilton 1971), but has been difficult to achieve. As noted above, DePaolo and Wasserburg (1979) produced a relatively precise internal Sm–Nd isochron for mineral-whole rock analyses from a gabbronorite of 2701 ± 8 Ma. A 100-pound (45 kilograms) sample of norite from the Basal Series yielded abundant zircon (Nunes and Tilton 1971) from which Nunes (1981) published a revised age of 2713 ± 3 Ma, an upper intercept $^{207}Pb/^{206}Pb$ age from highly discordant analyses of multi-grain zircon fractions (up to 1 mg) that is slightly older than the Sm-Nd isochron age. Premo et al. (1990) reported a range of U–Pb ages for zircon separated from footwall mafic sills and dikes (2711–2712 Ma) and a composite (7 multi-grain fractions) zircon-baddeleyite age (2705 ± 4 Ma) for two samples from the Lower Banded Series. The uncertainty of this age was reduced to 2704 ± 1 Ma ($^{207}Pb/^{206}Pb$ upper intercept ages) if the results of two fractions were omitted. Based on their associated uncertainties, these studies indicate a possible range of ~ 10–20 million years at ca. 2.7 Ga for crystallization of the Stillwater Complex.

U–Th–Pb-bearing Accessory Minerals in Stillwater Cumulates

To constrain the duration of magmatism in the Stillwater Complex, to test whether there were distinct magmatic episodes during emplacement of the intrusion, and to constrain the temporal relationship of PGE mineralization (J-M Reef) to the cumulates, we initiated a detailed U–Pb geochronological study of the Stillwater Complex from all the major units of the intrusion and from cross-cutting granophyres (Fig. 1.5). Samples were collected over the course of two field seasons. In summer

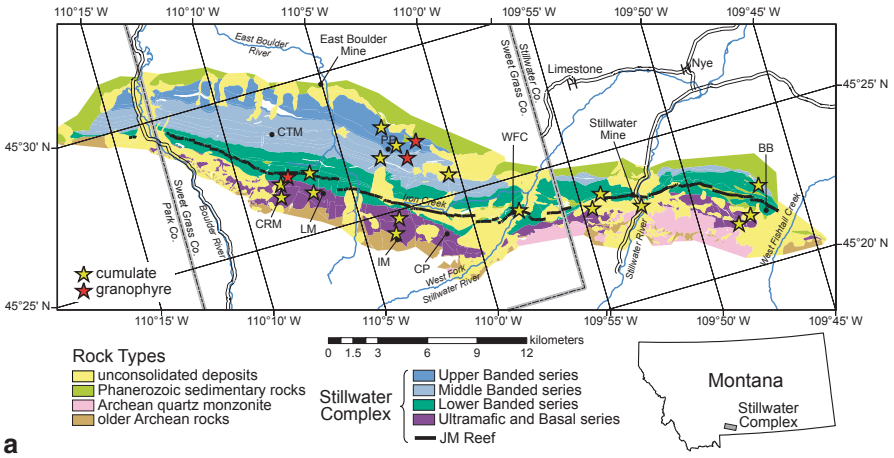

a

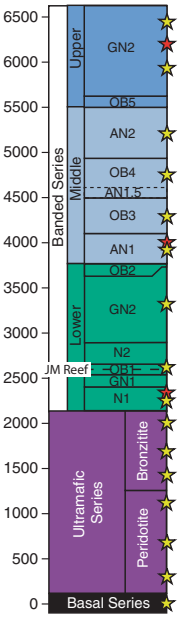

b

c

Zircon	Baddeleyite	Rutile	Apatite	Titanite	Weight (kg)
+	+	-	+	-	27.6
+	-	+	+	+	18.2
-	-	-	-	-	15.5
+	+	+	+	-	50.2
-	-	-	+	-	15.3
+	+	-	+	-	11.5
+	+	+	+	+	20.0
-	-	-	+	-	23.4
+	+	-	+	-	23.4
+	+	+	+	+	16.8
+	-	+	+	-	13.2
-	-	-	-	-	16.8
+		-	+	-	17.1
+	+	-	+	-	14.5
+	+	-	+	-	23.8
+	+	-	+	-	9.5
+	-	-	+	-	19.3

Fig. 1.5 Locations and mineral yields for U–Pb geochronological samples collected in the Stillwater Complex (Montana, USA). **a** Simplified geological map of the Stillwater Complex showing sample locations (adapted from Zientek et al. 2005); *stars* indicate sample locations. Also shown are the locations of the two PGE mines, Stillwater and East Boulder Mine. Abbreviations: *CTM* Contact Mountain; *CRM* Chrome Mountain, *IM* Iron Mountain; *PP* Picket Pin, *CP* Castle Point; *WFC* West Fork Creek, *BB* Benbow. **b** Stratigraphic section after McCallum (1996) showing the relative locations of samples—stratigraphic height in metres above the basal contact of the intrusion. **c** Table indicating range of U–Pb-bearing accessory minerals separated from each of the samples (+=mineral recovered; −=mineral not recovered) and weight in kilograms of samples that were processed (range from 9.5 to 50.2 kg)

2005, the first set of samples ($n=8$) was collected from the Picket Pin, Chrome Mountain, and Contact Mountain areas of the high plateau in the west-central part of the Stillwater Complex and the sampling focused mainly on the gabbroic rocks of the Banded Series (Fig. 1.5a). Samples were selected based primarily on accessibility and with knowledge of existing whole rock trace element concentrations for samples from the two olivine-bearing zones (OB3 and OB4) in the Middle Banded Series (Meurer and Boudreau 1996; Meurer et al. 1999; WP Meurer, unpublished data). Samples with elevated incompatible trace element concentrations (e.g., Zr, U, Th, REE) were assumed to contain higher relative abundances of minerals that crystallized from fractionated interstitial melt and thus had an enhanced potential to contain zircon or baddeleyite. Based on these criteria, the success rate was approximately 50 % for the cumulates (four out of eight mafic-ultramafic samples yielded zircon ± baddeleyite) and 100 % for the four granophyre samples (all contained zircon ± rutile and titanite).

In summer 2011, sampling ($n=14$) was focused primarily on the Ultramafic Series as well as remaining gaps in the Banded Series, including samples from the uppermost units of the intrusion just below the unconformity with overlying Paleozoic and Mesozoic sedimentary rocks (Fig. 1.5a). Using knowledge gained from sampling mafic-ultramafic rocks in the intervening years (e.g., Bushveld Complex, Scoates and Friedman 2008; Muskox intrusion, Mackie et al. 2009; Thompson Nickel Belt, Scoates et al. 2010; Bird River Sill, Scoates and Scoates 2013), we targeted samples based primarily on their textural features (Fig. 1.6). Outcrops with heterogeneous structures (e.g., sulphide-bearing Basal Series norite, Fig. 1.6a), outcrops that contained coarse-grained (pegmatitic) patches, especially with coarse interstitial plagioclase (e.g., feldspathic pyroxenites and troctolites, Figs. 1.6b, c, and d), or plagioclase-rich rocks with relatively abundant and irregularly distributed poikilitic to sub-poikilitic pyroxene (ortho- and clinopyroxene) (Figs. 1.6e and f) were preferentially sampled. Outcrops that were avoided included those with no evidence for interstitial plagioclase (e.g., knobby peridotite with orthopyroxene oikocrysts, Fig 1.7a), with monomineralic rock types (e.g., orthopyroxenite pegmatite, Fig. 1.7b), consisting of one, two-, and three-phase cumulates with only minor interstitial material (i.e., "adcumulates" in the terminology of Wager et al. 1960) (e.g., bronzitite, Fig. 1.7c; gabbronorite, Figs. 1.7d and 1.7f), and plagioclase-rich rocks dominated by large (up to 5 cm) orthopyroxene oikocrysts (Fig. 1.7e). As a result, recovery of zircon (± baddeleyite) was over 90 % successful (13 out of the 14 samples processed) (Fig. 1.5c), including nearly all of the samples from the Ultramafic Series. Anorthosites, or other plagioclase-rich rocks, from the Banded Series are particularly good targets when multiple poikilitic to oikocrystic phases are present. Haskins and Salpas (1992) noted from their study of the geochemistry of ANII in the Middle Banded Series that samples with elevated incompatible trace element contents were richest in cumulus plagioclase and in intercumulus plagioclase and pyroxene. Preliminary results from the dated Stillwater samples indicate that the Banded Series crystallized at ca. 2709 Ma (Wall et al. 2010) and on-going results constrain the total duration of magmatism to a 3–4 million year window from 2709 to 2712 Ma (Wall et al. 2013).

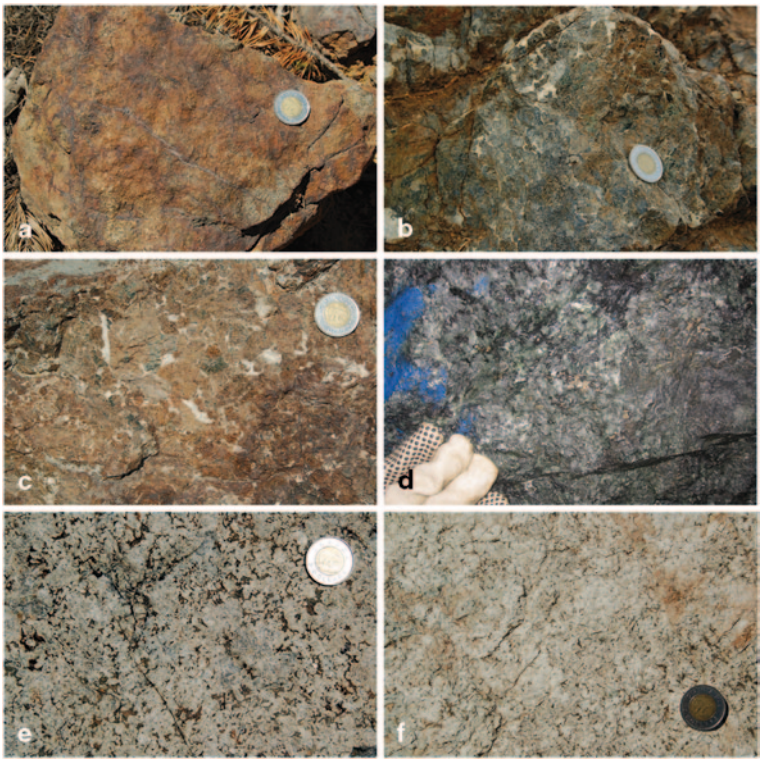

Fig. 1.6 Photographs of outcrops in the Stillwater Complex showing the macroscopic textures of successful sample targets that yielded zircon or baddeleyite for U–Pb dating (scale: *coin* is 2.75 cm in diameter). **a** Sulphide-bearing norite, Basal Series (Benbow). **b** Pegmatitic feldspathic orthopyroxenite *above* Chromitite J, Peridotite Zone (Benbow). **c** Pegmatitic feldspathic orthopyroxenite (note large *green* clinopyroxene), base of Bronzitite Zone (Iron Mountain). **d** Pegmatitic feldspathic olivine gabbronorite, J-M Reef (East Boulder Mine), Olivine-bearing zone I, Lower Banded Series; note coarse interstitial sulphide clots. Glove for scale (*blue* color is paint). **e** Leucogabbronorite with irregular poikilitic ortho- and clinopyroxene, Anorthosite-II zone, Middle Banded Series (Picket Pin). **f** Anorthosite with minor interstitial ortho- and clinopyroxene, uppermost Gabbronorite-III zone, Upper Banded Series (Picket Pin)

Dating the Merensky Reef in the Bushveld Complex

Background

The Paleoproterozoic Bushveld Complex in the northern Kaapvaal craton of South Africa (Fig. 1.8) (Cawthorn, Chap. 12, The Bushveld Complex) is host to some of the richest PGE, chromium, and vanadium deposits on Earth (Lee 1996) and currently produces the majority of the world's platinum (~80%), primarily from two stratiform sequences, the Merensky Reef and the Upper Group 2 (UG2) chromitite (Cawthorn et al. 2005). The age of the Bushveld Complex and of these major min-

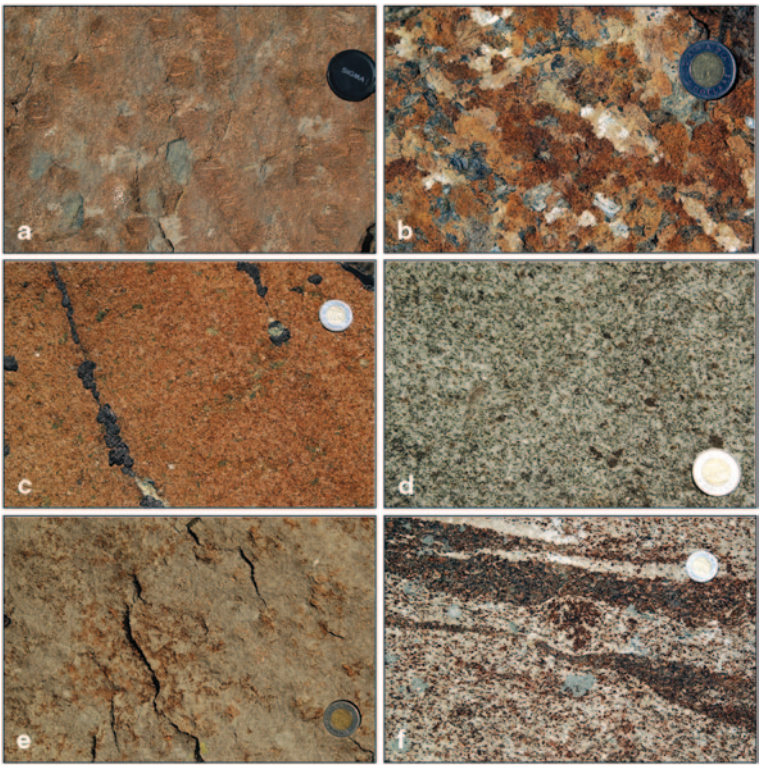

Fig. 1.7 Photographs of outcrops in the Stillwater Complex showing the macroscopic textures of sample targets that failed to yield zircon or baddeleyite or that are not considered prospective for U–Pb dating (scale: *coin* is 2.75 cm in diameter). **a** Peridotite with abundant orthopyroxene oikocrysts, Peridotite zone (Iron Mountain); lens cap is 7.25 cm in diameter. **b** Orthopyroxenite pegmatite, Peridotite zone (Chrome Mountain). **c** Clinopyroxene-bearing orthopyroxenite, Bronzitite zone (Chrome Mountain). **d** Gabbronorite, Gabbronorite-I (*below* J-M Reef), Lower Banded Series (West Fork); note that this is the sample locality of STL-100 from DePaolo and Wasserburg (1979). **e** Anorthosite with large orthopyroxene oikocrysts, Anorthosite-I, Middle Banded Series (Picket Pin). **f** Layered gabbronorite, Gabbronorite-III, Upper Banded Series (Picket Pin)

eralized horizons has long been of interest with comprehensive summaries provided in Walraven et al. (1990), Buick et al. (2001), and Nomade et al. (2004). Scoates and Friedman (2008) reported the first published precise age of crystallization for the Bushveld Complex by the CA-TIMS technique from a sample of the Merensky Reef (U–Pb zircon, 2054.4 ± 1.3 Ma, weighted mean $^{207}Pb/^{206}Pb$ age). In the section below, we provide an integrated U–Pb zircon/rutile/apatite and $^{40}Ar/^{39}Ar$ biotite geochronological approach from two widely separated (~310 km) samples of the Merensky Reef, including a revised value for the Scoates and Friedman (2008) age based on the significant changes in analytical protocols described in previous sections (Table 1.2).

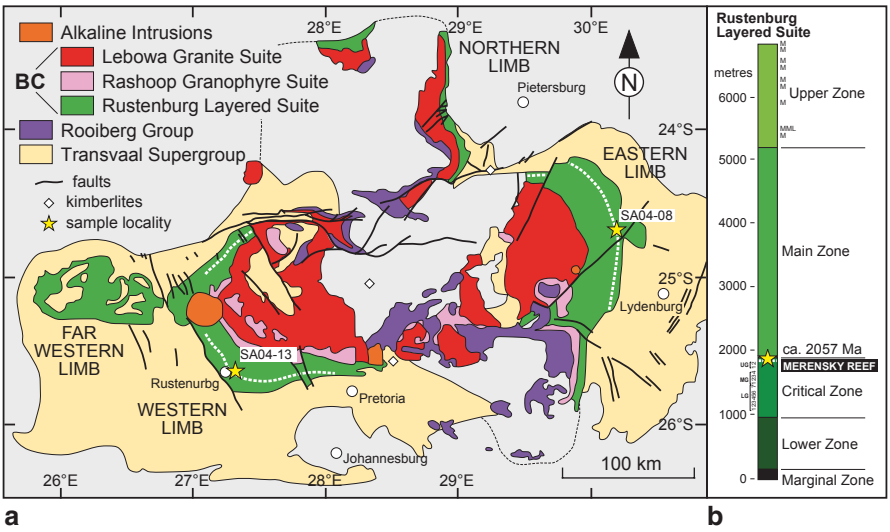

Fig. 1.8 Locations and geologic context of Merensky Reef samples in the Bushveld Complex. **a** Generalized geologic map of the Bushveld Complex (*BC*) showing the position of the Merensky Reef (*white dashed* line) and sample locations (*yellow* stars) (map modified from Kinnaird et al. 2005). Sample SA04-13 was collected underground from the Merensky Reef in West Mine (Rustenburg area). Sample SA04-08 was collected on surface from the Merensky Reef as exposed on the Farm Driekop. **b** Simplified stratigraphic section showing the major subdivisions of the layered mafic-ultramafic rocks (Rustenburg Layered Suite), the position of the platiniferous Merensky Reef near the *top* of the Critical zone, and the approximate positions of major chromitite horizons (*LG* Lower Group, *MG* Middle Group, *UG* Upper Group) in the Critical zone and major magnetite horizons in the Upper zone (*MML* main magnetite layer, *M* magnetite horizon)

Geologic Setting of the Merensky Reef in the Bushveld Complex

The Bushveld Complex consists of an 400 km-wide, 7- to 9-km-thick sequence of layered mafic-ultramafic rocks (referred to as the Rustenburg Layered Suite), which may be a shallowly dipping, interconnected sheet (Webb et al. 2004), that is associated with pre- and syn-layered suite marginal sills and intrusions (e.g., Eales and Cawthorn 1996; Kruger 2005) (Fig. 1.8a). The Bushveld Complex was emplaced at shallow levels in the crust (0.15–0.25 GPa: Pitra and de Waal 2001) into Paleoproterozoic rocks of the Transvaal Supergroup and the ca. 2061 Ma Rooiberg Group (Walraven 1997), a 6-km-thick sequence of precursor basaltic andesites to rhyolites (Buchanan et al. 2002; Mathez et al. 2013) that defines the upper age limit for the complex. The layered mafic-ultramafic rocks themselves are overlain and locally cut by a 2.5-km-thick sequence of ca. 2054 Ma granites (Rashoop Granophyre Suite and Lebowa Granite Suite: Walraven and Hattingh 1993).

Rocks of the Bushveld Complex are distributed in four discrete regions (Fig. 1.8a). The 200 km-long Eastern Limb contains the best surface exposures of the complex, including the Merensky Reef. The Western Limb, also ~200 km in length, generally

has poor outcrop, although it has historically been the focus of much of the active mining for PGE due its higher average grades. The Northern Limb is partially covered beneath younger rocks and is notable for the presence of the PlatReef, a pyroxenitic-harzburgitic PGE–Cu–Ni-bearing package (up to 300 m-thick) that is situated directly on, or within a few tens of metres, of the contact with country rocks (e.g., Kinnaird et al. 2005; Mitchell and Scoon 2012). The least known of the regions, the Far Western Limb, is a poorly exposed eroded remnant of the Bushveld Complex. The Rustenburg Layered Suite, dominated by mafic-ultramafic rocks, is subdivided into the Marginal, Lower, Critical, Main, and Upper zones based on a variety of criteria (e.g., Eales and Cawthorn 1996), but most commonly on the appearance of a new cumulus mineral (Fig. 1.8b).

The PGE-rich Merensky Reef and UG-2 chromitite are both hosted in the Critical zone of the lower part of the Bushveld Complex. The Merensky Reef is a distinctive 40 to 120 cm-thick minable layer with a relatively constant grade of PGE (5–8 g/t or ppm) that occurs at the top of the Upper Critical zone and can be traced for several 100 km in the western and eastern limbs of the intrusion (white dashed line in Fig. 1.8a) (Cawthorn et al. 2005). The Reef is highly variable in thickness, structure, and texture and it can display strong vertical and lateral lithologic variations (Smith et al. 2003; Mitchell and Scoon 2007). The Merensky Reef in its highest or "normal" stratigraphic position in the Western limb consists of sulphide-bearing (2–4 vol %), coarse-grained (pegmatitic) feldspathic orthopyroxenite or melanorite bounded by thin chromitite stringers with the PGE concentrated near the chromitites (e.g., Barnes and Maier 2002; Smith et al. 2003; Cawthorn and Boerst 2006). The footwall to "normal" Reef facies varies from norite to anorthosite and the hanging wall is typically orthopyroxenite. The Merensky Reef in the Eastern limb shares some structural and compositional similarities with the classic localities described from the Western limb, although it is also characterized by some important differences. At Winnaarshoek, the 10–15 m-thick Reef package contains a 2–5 m-thick basal layer of feldspathic orthopyroxenite that includes the 1.8 m-thick Reef, which is bounded by thin chromitites (Mitchell and Scoon 2007). The Reef package here is underlain by layered norites and overlain by a sequence of plagioclase-rich rocks (norite-leuconorite, spotted-mottle anorthosite, mottled anorthosite). Pegmatitic feldspathic orthopyroxenites are known to occur in the Eastern limb, but unlike the Western limb they are not commonly mineralized.

Sample Locations and Characterization

Samples of pegmatitic feldspathic orthopyroxenite (SA04-11 and SA04-13) from the Western limb of the Rustenburg Layered Suite were collected on May 4, 2004 (erroneously given as April 4, 2004 in Scoates and Friedman 2008), from the mining face of the Merensky Reef (Fig. 1.9a) in the West mine, Townlands shaft (now known as the Khuselaka platinum mine, Khuseleka 1 shaft [25°37'29.1"S, 27°15'31.9"E]; level 22, ~850 m below surface), Rustenburg mining section. In the sampled area,

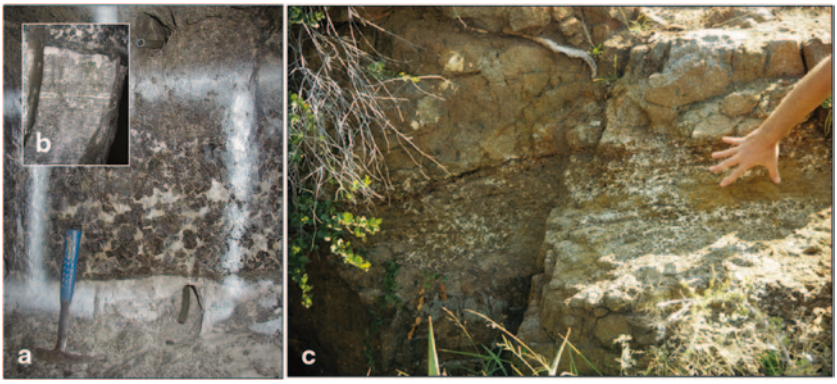

Fig. 1.9 Photographs showing sample localities of the Merensky Reef in the Bushveld Complex. **a** Photograph of the mining face of the Merensky Reef in the West Mine (Townlands shaft; level 22, ~850 m below surface), Rustenburg mining section, showing the coarse grain size and heterogeneous texture of the pegmatitic feldspathic orthopyroxenite. The *lower* bounding chromitite is a thin dense layer 2–3 cm thick, whereas the *upper* chromitite is an irregular diffuse layer ~2 cm thick. **b** Inset photograph focuses on the footwall contact of the Reef and underlying leuconorite; note 5 cm-thick anorthosite horizon immediately below lower chromitite and irregular anorthosite layers ~80 cm below lower chromitite. Photographs courtesy of Pat Hayman; hammer for scale. **c** Photograph of the Merensky Reef in outcrop at the Farm Driekop, Eastern Limb. Hand for scale

Reef thickness varies from ~5 to 40 cm (Figs. 1.9a and b). A sample (SA04-08) of the Merensky Reef exposed at surface from the Eastern Limb was collected on May 2, 2004, at Farm Driekop (24°31'11"S, 30°05'11.4"E) (Fig. 1.9c). The sample site is referenced in Bristow et al. (1993, Locality 3.4, p. 26) and the Reef was exposed in three old adits near the crest of a small hill at the time of sampling. The sample was collected from the northern edge of the adit from medium-grained equigranular pyroxenite beneath patchy pegmatitic feldspathic pyroxenite (Fig. 1.9c).

Sample SA04-13, a pegmatitic feldspathic orthopyroxenite, consists of large orthopyroxene crystals (0.5–3 cm diam), many displaying euhedral habit, enveloped by interstitial plagioclase that locally occupies pockets up to 5 cm across (Figs. 1.10a, b). Clots of biotite (0.5–1 cm), locally associated with zircon and interstitial quartz, and sulphide aggregates up to 0.5 cm diameter are heterogeneously distributed throughout the sample. Small (<0.4 mm) chromite grains occur in clusters and are concentrated in an ~5 mm thick stringer with plagioclase and orthopyroxene along the base of the pegmatitic feldspathic orthopyroxenite. Sample SA04-08, a variably equigranular and pegmatitic feldspathic pyroxenite, consists of small to large (0.1–2 cm diam) orthopyroxene crystals with both interstitial (poikilitic) clinopyroxene and plagioclase (Figs. 1.10c and 1.10d). Irregular rounded olivine grains (resorbed) occur within large orthopyroxene crystals. Minor interstitial biotite and quartz occur on the edges of the finer grained orthopyroxene and are locally intergrown with zircon. Only rare chromite grains (1–2 per thin section) are present in sample SA04-08 and there is no sulphide.

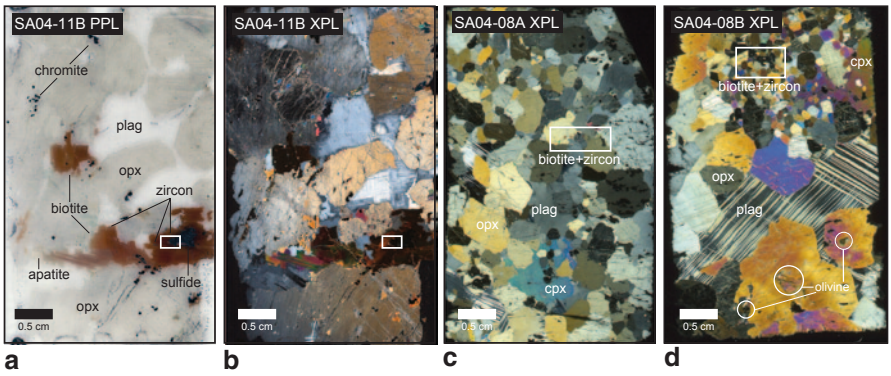

Fig. 1.10 Images of scanned thin sections for dated samples from the Merensky Reef (all sections are standard size, 45 × 25 mm). **a** Section SA04-11B (PPL) from the West Mine, Western Limb, showing the relative sizes and distribution of the main minerals (orthopyroxene, *opx*; plagioclase, *plag*; biotite, bio; *chromite*) and the locations of *zircon* and *apatite; white box* indicates location of zircon rim around *sulphide* shown in Fig. 1.11a. **b** Section SA04-11B (XPL) showing alteration along fractures in orthopyroxene and deformation in interstitial plagioclase (bent twins); *white box* indicates location of zircon rim around sulphide shown in Fig. 1.11a. **c** Section SA04-08A (XPL) from the Farm Driekop, Eastern Limb, showing equigranular orthopyroxene and clinopyroxene (*cpx*) with minor interstitial plagioclase; *white box* outlines area with minor late *interstitial biotite* and *zircon*. **d** SA04-08B (XPL) from the Farm Driekop, Eastern Limb, of feldspathic pyroxenite (both *opx* and *cpx*) with abundant large interstitial patches of plagioclase and no biotite; *white box* outlines area with minor late *interstitial biotite* and *zircon*

Accessory Minerals in the Merensky Reef

Both of the studied samples from the Merensky Reef, SA04-08 and SA04-13, are ideal targets for geochronology of layered intrusions as they are texturally heterogeneous with abundant interstitial plagioclase and local patches of biotite identifiable in hand sample (Figs. 1.9, 1.10). In thin section, both samples also reveal a wealth of potentially dateable accessory minerals that were identified and characterized prior to sample processing for mineral separates (Fig. 1.11).

Zircon, rutile, apatite, and biotite occur in the Merensky Reef (Figs. 1.11a, b, c, d, e, f, g, h, i and j), typically associated with interstitial quartz and alkali feldspar/plagioclase, locally as granophyric or myrmekitic intergrowths (Figs. 1.11k, and l). Zircon (~20–500 microns) is most commonly intergrown with interstitial biotite and, in one example, observed to rim sulphide and is in turn enveloped by biotite (Figs. 1.11a, b, c and d). In most cases, zircon is anhedral or irregularly shaped in the Merensky Reef (Figs. 1.11a, b and c), although examples of euhedral morphology are present (Fig. 1.11d). Rutile was found throughout the Critical zone of the Bushveld Complex by Cameron (1979), but has rarely been reported in the more recent literature. We find rutile in most samples from the Bushveld Complex that we have examined. In sample SA04-13, rutile occurs primarily as large (150–250 microns) equant to irregular grains associated with chromite, included within, as

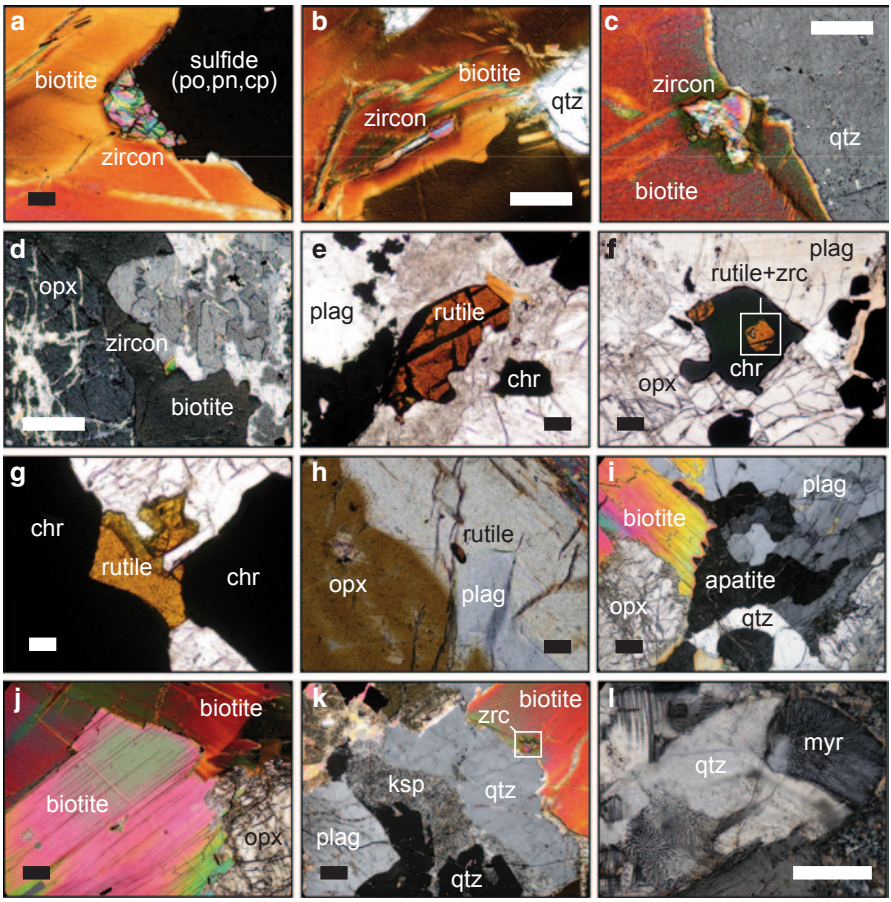

Fig. 1.11 Photomicrographs of accessory and other interstitial minerals in samples of the Merensky Reef (scale bar is 200 microns long in each panel). **a** Large grain of zircon on the margin of a composite sulphide (*po* pyrrhotite, *pn* pentlandite, *cp* chalcopyrite) encased in biotite (SA04-11B, XPL). **b** Zircon along cleavage plane in biotite with interstitial quartz (*qtz*) (SA04-11B, XPL). **c** Irregular zircon enclosed in the rim of biotite and in contact with interstitial quartz (SA04-11B, XPL). **d** Euhedral zircon on the margin of biotite in contact with orthopyroxene (*opx*) (SA04-11B, XPL). **e** Large single grain of rutile (brown-colored, high-relief) enclosed by orthopyroxene from near the base of the pegmatitic feldspathic orthopyroxenite (plagioclase, plag; chromite, *chr*) (SA04-13, PPL). **f** Rutile associated with chromite from the lower chromitite stringer; rutile apparently included in chromite contains an inclusion of zircon (zrc) (SA04-13, PPL). **g** Rutile on the edges of several chromite grains in contact with orthopyroxene (SA04-13, PPL). **h** Small euhedral crystal of rutile at the contact between orthopyroxene and plagioclase (SA04-08, XPL). **i** Large composite apatite cluster (at extinction) with interstitial biotite, quartz and plagioclase (SA04-11B, XPL). **j** Intergrown biotite grains (note euhedral outline to highly birefringent grain) showing deformation (*bent cleavage planes in lower centre*) and incipient alteration along the grain margin in contact with orthopyroxene (SA04-11B, XPL). **k** Interstitial biotite, quartz, and granophyre patch (quartz is at extinction, K-feldspar [*ksp*] is partially altered to sericite); note zircon in biotite rim (same as panel C) (SA04-11B, XPL). **l** Interstitial quartz and myrmekite (myr; vermicular intergrowth of quartz and plagioclase) (SA04-11B, XPL)

overgrowths on, and as discrete grains adjacent to chromite in the chromitite stringers (Figs. 1.11e, f and g). Smaller (20–100 microns), acicular grains of rutile are also observed enclosed in biotite, plagioclase, and orthopyroxene within the pegmatitic feldspathic orthopyroxenite of SA04-13 (Fig. 1.11h), and fine skeletal rutile-quartz intergrowths are found in SA04-08. Apatite is present as irregular interstitial aggregates intergrown with biotite and quartz (Fig. 1.11i). Biotite is present in all thin sections (~10) prepared from the Merensky Reef samples, ranging in size from large (1–2 cm) macroscopic sheaths (Figs. 1.10a, 1.11a and j) to fine (0.1–0.5 mm) platelets with quartz in interstitial patches between orthopyroxene crystals.

Microscopic quartz and quartz-alkali feldspar intergrowths are heterogeneously distributed throughout the Merensky Reef samples and are commonly spatially associated with zircon, biotite, apatite, and more rarely, rutile (Figs. 1.11b, c, i, k and l). Although rarely noted in the literature, Wagner (1929, p. 106) identified quartz and quartz-feldspar intergrowths in samples of the Merensky Reef from the Eastern Limb (Lydenburg district). This "granitic" association of minerals (quartz, alkali feldspar, biotite, zircon, apatite, rutile) indicates that much of the zircon and the other U–Th–Pb accessory minerals crystallized from fractionated interstitial melt likely at temperatures approaching the solidus of the Merensky Reef samples.

Zircon Textures and Zoning in Cathodoluminescence Images

The external morphology and internal textures of zircon reflect the geological history of the mineral (e.g., Pupin 1980; Vavra 1993; Corfu et al. 2003). Zircon imaging is accomplished initially using a binocular microscope during grain selection for geochronology based on a variety of features such as color, degree of transparency, shape and external morphology, and the absence of inclusions (mineral and fluid) and fractures. Backscattered electron (BSE) and cathodoluminescence (CL) imaging provide the highest resolution of internal structures (i.e., zoning, xenocryst cores, subsolidus modifications) of zircon and CL imaging is now considered standard practice in the final selection of grains for geochronology. Corfu et al. (2003) provide an excellent overview of zircon selection and imaging techniques for examining morphology and textures. Cathodoluminescence emission in zircon is complex with the possibility of quenching by optical absorption processes, however, it is dominated by narrow emission bands generally related to Dy^{3+}impurities or other rare earth elements such as Sm^{3+}, Eu^{2+}, Tb^{3+}(Nasdala et al. 2003).

For detailed imaging of zircon from the Merensky Reef samples in this study, all selected zircons were mounted in epoxy in 2.5 cm diameter circular grain mounts and polished until the grains were sectioned in half. The polished epoxy sections were carbon coated and prepared in the Electron Microbeam/X-Ray Diffraction Facility at the University of British Columbia, Vancouver. Back-scattered electron (BSE) and cathodoluminescence (CL) imaging were carried out on a Philips XL-30 scanning electron microscope (SEM) equipped with a Bruker Quanta 200 energy-dispersion X-ray microanalysis system and a Robinson cathodoluminescence detector. An operating voltage of 15 kV was used, with a spot diameter of 6 μm, and peak count time of 30 s.

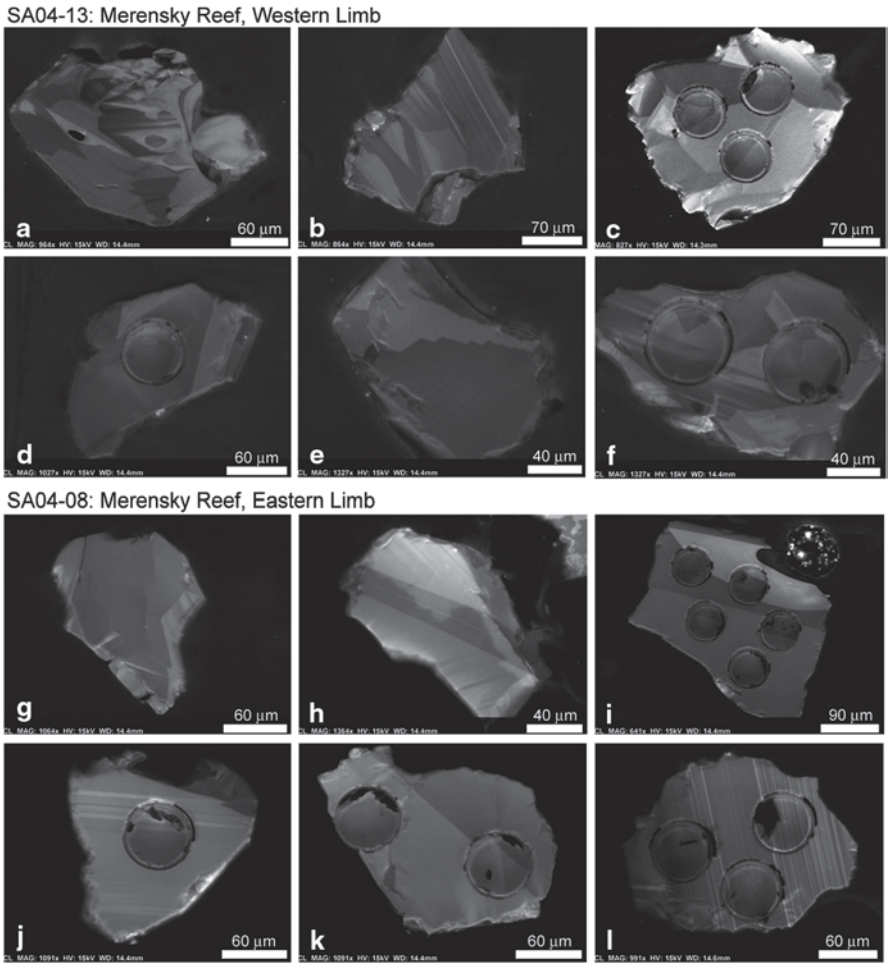

Fig. 1.12 Cathodoluminescence (*CL*) images of zircon from the Merensky Reef. Scale indicated with scale bars on each image. **a**–**f** Zircon grains from sample SA04-13, Western Limb, showing the typical irregular, anhedral morphology of interstitial zircon and simple to complex sector zoning. **g**–**l** Zircon grains from sample SA04-08, Eastern Limb again showing the typical irregular, anhedral morphology of interstitial zircon and presence of oscillatory zoning in addition to broad sector zones. *Circular* pits indicate locations of laser ablation-ICP-MS spot analyses (60 µ diameter) for trace element concentrations in zircon (note that the orientation of some zone contacts can be observed within the pits)

The BSE images of the Merensky zircon grains (not shown) reveal little internal structure with only slight changes in brightness, reflecting changes in average atomic number, present along select grain margins. In contrast, CL images provide clear details of the range of zoning present in zircon (Fig. 1.12), even though the CL emission is relatively low compared with zircon grains from other layered intrusions (e.g., Stillwater, work in progress). There is no evidence of inheritance

or xenocrystic cores in any of the analyzed Merensky zircons. The external morphology is typically irregular with only local development of rational crystal faces (e.g., Figs. 1.12a, d, g and h) as is typical of zircon from gabbroic rocks that crystallized from fractionated interstitial melt late in the consolidation history of a cumulate (e.g., Scoates and Chamberlain, 1995; Scoates and Friedman 2008). Sector zoning is predominant in sample SA04-13 (Figs. 1.12a, b, c, d, e and f) and fine to coarse oscillatory zoning is characteristic of zircon from sample SA04-08 (Figs. 1.12g, h, i, j, k and l), likely reflecting different growth rates for zircon from these two different, and widely separated, samples of Merensky Reef (e.g., Hanchar and Miller 1993; Watson and Liang 1995; Corfu et al. 2003). The CL images also show that there are no prominent truncation surfaces indicative of resorption and there are few inclusions (Fig. 1.12a, black elongate feature in centre-left; Fig. 1.12k, black spot at base on rightmost laser ablation pit).

Methods

Treatment and Dissolution of Zircon, Rutile and Apatite

Mineral treatment protocols were carried out at the Pacific Centre for Isotopic and Geochemical Research (PCIGR) at the University of British Columbia, Vancouver (Canada). Zircon grains were separated from samples using conventional crushing, grinding, and Wilfley table techniques, followed by final concentration using heavy liquids and magnetic separation. Fractions of zircon, rutile, and apatite for analysis were hand-picked in methanol under magnification using a binocular microscope and selected based on grain morphology, quality, size and low magnetic susceptibility. Biotite grains were also handpicked under magnification using a binocular microscope and selected based on size and lack of inclusions and alteration.

All handpicked zircon grains were anhedral, clear, colorless to light pink, devoid of mineral and fluid inclusions, and ~50 μm in diameter. Prior to dissolution, the zircon grains were annealed and chemically abraded following the procedures outlined in Mattinson (2005). The zircon grains selected for CA-TIMS analysis were annealed in quartz glass crucibles in a muffle furnace at 900°C for 60 h. They were transferred into 10 mL Pyrex® beakers, agitated in ultrapure 3 N HNO_3 in an ultrasonic cleaner for 15 min, warmed to 60 ± 10°C for 30 min, and rinsed with ultrapure acetone and water. The zircon grains were then transferred to 3.5 mL PFA screwtop beakers, ultrapure HF (50%, 500 μL) and HNO_3 (14 N, 50 μL) were added, and caps were closed finger-tight. Following this, the beakers were placed in 125 mL PTFE Teflon® liners (up to four per liner) and about 2 mL HF and 0.2 mL concentrated HNO_3 was added to the liners. The liners were slid into stainless steel jackets of Parr® high-pressure dissolution devices, which were sealed and brought up to 200 °C for 16 h. After cooling, the beakers were removed from the liners and the remaining zircon grains were separated from the leachate.

The annealed, leached, and rinsed grains were then weighed, each transferred into 300 μL PFA microcapsules, and 50 μL of 50% HF and 5 μL of 14 N HNO_3

were added. Single zircon grains were transferred into individual microcapsules and each was spiked with EARTHTIME ^{205}Pb–^{233}U–^{235}U isotope tracer (verified by comparison with three mixed U–Pb gravimetric reference solutions from Massachusetts Institute of Technology, the University of California, Santa Barbara, and the National Environment Research Council Isotope Geosciences Laboratory, United Kingdom, made available through EARTHTIME), and each was subsequently capped and placed in a Parr® liner (8–13 microcapsules per liner). HF and nitric acids in a 10:1 ratio, respectively, were added to the liner, which was then placed in the jacket, sealed, and brought up to 240°C for 40 h for complete dissolution. The resulting solutions were dried on a hotplate at 130 °C. The fluorides were dissolved in 3.1 N HCl in the high-pressure devices for 12 h at 210 °C. Following dissolution, samples were transferred into clean 7 mL PFA beakers and dried after adding 2 µL of 0.5 N H_3PO_4. No chemical separation of U and Pb was done for zircon in this study.

Rutile was most abundant in the M2 and M5 magnetic fractions of both samples, whereas apatite was most abundant in the N2 magnetic fractions. Hand-picked rutile ranged in color from amber to chocolate brown, in shape from euhedral (rare) to subhedral wafers and irregular fragments, and in size from 100 to 200 µm across (5–10 grains per fraction). Handpicked apatite grains were colorless, subhedral and irregular fragments, and ranged in size from 50 to 100 µm across (25–85 per fraction). Rutile fractions were transferred into 10 mL Pyrex® beakers. About 2 mL of 1 M HNO_3 was added and grains were ultrasonicated for 5 min and warmed to 60 ± 10 °C for 10 min, rinsed with > 18 MΩ•cm water followed by sub-boiled acetone, and then air-dried. Fractions were weighed and transferred to 3.5 mL screwtop PFA Teflon® beakers. One mL of a 10:1 mixture of sub-boiled 50 % HF and 14 M HNO_3 was added followed by a weighed drop of EARTHTIME ^{205}Pb –^{233}U –^{235}U isotope tracer. The beakers were capped tightly and placed in a Parr® liner (four beakers per liner). HF and nitric acids in a 10:1 ratio, respectively, were added to the liner, which was then placed in the jacket, sealed, and brought up to 240°C for 40 h for complete dissolution. The resulting solutions were dried on a hotplate at 130°C. The fluorides, along with the weighed apatite fractions, were dissolved in 3.1 N HCl in the high-pressure devices for 12 h at 210 °C. Uranium was eluted into a beaker with 0.5 N HBr followed by elution of Pb into a separate beaker with 6.2 N HCl. The U was taken nearly to dryness at 110 °C, and 1 mL of sub-boiled 6.2 N HCl was added. The resin in the columns was washed with > 18 MΩ•cm water and conditioned with 6.2 N HCl, then the U solution was reintroduced into each column and washed with 8M HNO_3 to remove iron. Uranium was then eluted with water into the same beaker into which Pb was eluted. Samples were dried after addition of 2 µL of 0.5 N H_3PO_4.

U–Pb TIMS Isotopic Analysis

All zircon, rutile, and apatite samples were loaded onto single zone-refined Re filaments with 2 µL of silicic acid activator (Gerstenberger and Haase 1997). Both Pb

and U isotopes were analyzed in the peak-hopping mode using a modified thermal ionization mass spectrometry (TIMS) on a VG354S equipped with Sector 54 electronics and a Daly photomultiplier housed at PCIGR (Table 1.2). All major Pb and U isotopes were collected in an analogue Daly detector. Isotope ratios of Pb were corrected for a fractionation of 0.25 %/amu ± 0.02 % (2s) based on replicate analysis of the NBS-982 Pb reference material throughout the course of this study. Due to the presence of two U isotopes in the spike, U is self-corrected in each run. All analytical errors were numerically propagated through the entire age calculation using the technique of Roddick (1987). Standard concordia diagrams were constructed and U–Pb concordia ages calculated with U–Pb_Redux (McLean et al. 2011); all errors are quoted at the 2s level. Additional U–Pb analytical results and details of the analytical procedure can be found in the footnote to Table 1.4.

Biotite and $^{40}Ar/^{39}Ar$ Isotopic Analysis

Biotite separates were hand-picked, washed in acetone, dried, wrapped in aluminum foil and stacked in an irradiation capsule with similar-aged samples and neutron flux monitors (Fish Canyon Tuff sanidine). The samples were irradiated on October 29 through November 4, 2005 at the McMaster Nuclear Reactor in Hamilton, Ontario, for 225 MWH, with a neutron flux of approximately 3×10^{16} neutrons/cm^2. Analyses ($n = 36$) of 12 neutron flux monitor positions produced errors of < 0.5 % in the J value. The samples were analyzed on January 3 and 4, 2006, at PCIGR. The mineral separates were step-heated at incrementally higher powers in the defocused beam of a 10W CO_2 laser (New Wave Research MIR10) until fused. The gas evolved from each step was analyzed by a VG5400 mass spectrometer equipped with an ion-counting electron multiplier. All measurements were corrected for total system blank, mass spectrometer sensitivity, mass discrimination, radioactive decay during and subsequent to irradiation, as well as interfering Ar from atmospheric contamination and the irradiation of Ca, Cl and K (isotope production ratios: $(^{40}Ar/^{39}Ar)K = 0.0302 \pm 0.00006$, $(^{37}Ar/^{39}Ar)Ca = 1416.4 \pm 0.5$, $(^{36}Ar/^{39}Ar)Ca = 0.3952 \pm 0.0004$, $Ca/K = 1.83 \pm 0.01(^{37}ArCa/^{39}ArK)$).

The results of the $^{40}Ar/^{39}Ar$ analyses, including plateau (spectrum) and inverse correlation ages, are shown in Table 1.5. The plateau and correlation ages were calculated using Isoplot ver. 3.09 (Ludwig 2003). Errors are quoted at the 2s (95 % confidence) level and are propagated from all sources, except for mass spectrometer sensitivity and age of the flux monitor. The best statistically justified plateau and plateau age were picked based on the following criteria: (1) three or more contiguous steps comprising more than 50 % of the ^{39}Ar; (2) probability of fit of the weighted mean age greater than 5 %; (3) slope of the error-weighted line through the plateau ages equals zero at 5 % confidence; (4) ages of the two outermost steps on a plateau are not significantly different from the weighted-mean plateau age (at 1.8s, six or more steps only); (5) outermost two steps on either side of a plateau must not have non-zero slopes with the same sign (at 1.8s, nine or more steps only).

Table 1.4 U–Th–Pb results for zircon, rutile and apatite from the Merensky Reef, Bushveld Complex

Composition							Isotopic Ratios					
	Mass[b]	U[c]		Pb*[c]	Pb_c[e]							
Fraction[a]	(µg)	(ppm)	Th/U[d]	(ppm)	(pg)	Pb*/Pb_c[e]	$^{206}Pb/^{204}Pb$[f]	$^{206}Pb/^{238}U$[g]	±2σ %[h]	$^{207}Pb/^{235}U$[g]	±2σ %[h]	$^{207}Pb/^{206}Pb$[g]
SA04-13 Zircon (Western Limb)												
CA1	24	7	3.68	5	0.92	135	4558	0.37507	0.11287	6.56936	0.16953	0.12703
CA2	21	18	4.00	13	0.91	304	9857	0.37566	0.10223	6.57788	0.15167	0.12700
CA3	14	44	2.80	27	1.05	364	13913	0.37548	0.10336	6.57508	0.15255	0.12700
CA4	11	103	1.28	50	0.91	607	29947	0.37562	0.09453	6.57833	0.14305	0.12702
CA5	12	31	1.59	16	1.70	110	5130	0.37394	0.08802	6.54894	0.15185	0.12702
CA6	12	22	4.30	17	1.68	118	3688	0.37491	0.09299	6.56664	0.16005	0.12703
SA04-08 Zircon (Eastern Limb)												
CA1	15	57	0.781	25	0.16	2277	124250	0.37428	0.31004	6.55404	0.32845	0.12700
CA2	12	28	1.37	14	1.63	103	4992	0.37548	0.30770	6.57611	0.32809	0.12702
CA3	14	23	0.747	10	0.42	324	17835	0.37435	0.32152	6.55595	0.34111	0.12702
CA4	11	11	1.17	5	4.34	14	700	0.37421	0.28923	6.56826	0.30842	0.12730
CA5	30	13	1.40	6	2.75	69	3318	0.37514	0.09252	6.56900	0.17149	0.12700
CA6	15	97	0.933	44	0.29	2279	120432	0.37527	0.15043	6.57124	0.18561	0.12700
CA7	15	28	1.62	14	0.70	310	14361	0.37571	0.10594	6.57931	0.15223	0.12701
CA8	13	33	1.21	16	0.75	276	13787	0.37528	0.08851	6.57157	0.14331	0.12700
CA9	15	65	1.41	32	1.29	376	18119	0.37534	0.09457	6.57102	0.14143	0.12697
CA10	20	155	1.19	74	0.82	1803	90453	0.37553	0.13116	6.57681	0.17235	0.12702
SA04-13 Rutile (Western Limb)												
R1	185	2	0.027	1.2	79.2	1.81	121	0.37488	0.257774	6.55513	0.43809	0.12682
R2	147	2	0.028	1.2	67.4	1.57	107	0.37604	0.288944	6.56994	0.46378	0.12671
R3	195	1	0.056	0.6	42.5	1.89	126	0.37597	0.260431	6.57130	0.44901	0.12676
R4	113	4	0.032	1.9	31.9	5.57	343	0.37498	0.182064	6.54762	0.32536	0.12664
R5	138	1	0.087	0.7	41.6	1.32	91.9	0.37755	0.324335	6.59989	0.43663	0.12678
SA04-08 Rutile (Eastern Limb)												
R1	207	37	0.008	14	33.0	84	5037	0.37464	0.13880	6.54559	0.17613	0.12672
R2	128	63	0.005	23	17.7	165	9878	0.37504	0.16505	6.55339	0.19694	0.12673
R3	111	62	0.005	23	18.2	136	8164	0.37275	0.37654	6.51103	0.39637	0.12669
R4	122	64	0.015	23	23.3	121	7217	0.37436	0.10208	6.54140	0.14781	0.12673
SA04-13 Apatite (Western Limb)												
A2	99	1	1.75	2.9	233	0.23	25.0	0.35892	4.11762	6.93679	7.32729	0.14017
A3	190	0.2	5.34	1.1	185	0.18	20.0	0.37108	10.72227	8.07141	17.46022	0.15776
SA04-08 Apatite (Eastern Limb)												
A1	140	2	3.11	10	1268	0.17	22.8	0.48566	3.10164	8.77285	4.16761	0.13101
A2	125	3	2.30	12	1309	0.17	23.7	0.45811	2.77341	7.97486	3.87527	0.12626
A3	64	3	1.37	18	1065	0.08	21.0	0.54384	4.09778	10.06558	5.52211	0.13424
A4	141	1	5.25	12	1472	0.12	19.9	0.60975	4.99752	11.45443	6.60221	0.13624
A5	144	1	4.76	14	1865	0.10	19.2	0.67948	5.80171	12.88478	7.33831	0.13753

[a] CA1, etc.: chemically abraded single zircon grains or fragments; chemical abrasion after Mattinson (2005) and Scoates and Friedman (2008); *R* rutile, *A* apatite

[b] Fraction weights of zircon determined from volume estimates just prior to final dissolution; apatite and rutile weights done by weighing on a microbalance

[c] U and Pb concentrations subject to uncertainty in weight of grains

[d] Th contents calculated from radiogenic ^{208}Pb and the $^{207}Pb/^{206}Pb$ date of the sample, assuming concordance between U–Th and Pb systems

[e] Pb* and Pb_c represent radiogenic and common Pb, respectively; mol% $^{206}Pb^*$ with respect to radiogenic, blank, and initial common Pb

[f] Measured ratio corrected for spike and fractionation only; mass discrimination of 0.25%/amu ± 0.03% (2σ abs) based on analysis of NBS-982 during the duration of this study; all Daly analyses

[g] Corrected for fractionation, spike, and common Pb; up to 5 pg (zircon), 5–10 pg (rutile), 20–25 pg (apatite) of common Pb was assumed to be procedural blank: $^{206}Pb/^{204}Pb = 18.50 \pm 1.0\%$; $^{207}Pb/^{204}Pb = 15.50 \pm 1.0\%$; $^{208}Pb/^{204}Pb = 38.40 \pm 1.0\%$ (all uncertainties 1-sigma); excess over blank was assigned to intial common Pb determined by leached feldspar analyses: $^{206}Pb/^{204}Pb = 15.174 \pm 0.006$, $^{207}Pb/^{204}Pb = 15.241 \pm 0.006$, and $^{208}Pb/^{204}Pb = 34.896 \pm 0.007$; 2σ errors

		Dates (Ma)						
±2σ %[h]	rho[i]	$^{206}Pb/^{238}U$[j]	±2σ abs[h]	$^{207}Pb/^{235}U$[j]	±2σ abs[h]	$^{207}Pb/^{206}Pb$[j]	±2σ abs[h]	% disc[k]
0.08786	0.877	2053.21	1.98	2055.25	1.49	2057.29	1.57	0.20
0.07032	0.913	2055.97	1.80	2056.39	1.34	2056.80	1.27	0.04
0.06605	0.932	2055.13	1.82	2056.01	1.34	2056.89	1.19	0.09
0.06251	0.935	2055.81	1.66	2056.45	1.26	2057.08	1.13	0.06
0.08130	0.897	2047.89	1.54	2052.50	1.34	2057.14	1.46	0.45
0.09225	0.858	2052.48	1.63	2054.88	1.41	2057.29	1.65	0.23
0.06376	0.981	2049.51	5.44	2053.19	2.89	2056.88	1.15	0.36
0.09010	0.961	2055.13	5.41	2056.15	2.89	2057.17	1.61	0.10
0.07382	0.976	2049.84	5.65	2053.44	3.01	2057.07	1.33	0.35
0.06828	0.975	2049.19	5.08	2055.10	2.72	2061.02	1.23	0.40
0.09623	0.898	2053.55	1.63	2055.20	1.51	2056.85	1.72	0.16
0.06296	0.947	2054.14	2.65	2055.50	1.64	2056.86	1.14	0.13
0.06954	0.910	2056.22	1.87	2056.58	1.34	2056.94	1.25	0.03
0.07392	0.895	2054.19	1.56	2055.54	1.26	2056.90	1.33	0.13
0.06722	0.905	2054.50	1.66	2055.47	1.25	2056.44	1.21	0.09
0.06412	0.942	2055.37	2.31	2056.24	1.52	2057.12	1.16	0.09
0.42184	0.356	2053.33	3.86	2052.30	4.53	2054.38	7.45	0.05
0.43732	0.400	2055.32	4.09	2057.76	5.09	2052.88	7.72	−0.12
0.41142	0.428	2055.51	3.96	2057.44	4.59	2053.56	7.26	−0.09
0.25028	0.645	2052.33	2.87	2052.79	3.20	2051.86	4.42	−0.02
0.33315	0.653	2059.33	3.85	2064.82	5.73	2053.85	5.88	−0.27
0.06443	0.944	2051.21	2.44	2052.05	1.55	2052.90	1.14	0.08
0.06524	0.950	2053.09	2.90	2053.10	1.73	2053.11	1.15	0.00
0.09517	0.971	2042.31	6.59	2047.39	3.49	2052.51	1.68	0.50
0.06293	0.938	2049.89	1.79	2051.49	1.30	2053.10	1.11	0.16
7.4621	0.248	1977.1	70.1	2103.4	65.0	2229.3	129.2	11
17.9313	0.263	2034.5	187.1	2239.1	157.7	2431.8	303.9	16
4.9958	0.079	2551.9	65.4	2314.7	38.0	2111.5	87.6	−21
4.5814	0.080	2431.2	56.2	2228.2	35.0	2046.5	80.9	−19
6.5841	0.087	2799.5	93.1	2440.8	51.0	2154.1	114.9	−30
7.9616	0.078	3069.0	122.0	2560.9	61.7	2180.0	138.6	−41
9.0480	0.066	3342.4	151.3	2671.3	69.2	2196.3	157.2	−52

[h] Errors are 2-sigma, propogated using the algorithms of McLean et al. (2011).

[i] R = correlation coefficient

[j] Isotopic dates are calculated using the decay constants $\lambda^{238} = 1.55125E^{-10}$ and $\lambda^{235} = 9.8485E^{-10}$ (Jaffey et al. 1971); $^{206}Pb/^{238}U$ and $^{207}Pb/^{206}Pb$ ages corrected for initial disequilibrium in $^{230}Th/^{238}U$ using Th/U [magma] = 3

[k] % discordance = 100 – (100*($^{206}Pb/^{238}U$ date)/($^{207}Pb/^{206}Pb$ date))

Table 1.5 $^{40}Ar/^{39}Ar$ results for biotite from the Merensky Reef, Bushveld Complex

Laser Power (%)	$\%^{39}Ar$	$^{40}Ar/^{39}Ar$	±1σ	$^{38}Ar/^{39}Ar$	±1σ	$^{37}Ar/^{39}Ar$	±1σ	$^{36}Ar/^{39}Ar$	±1σ	$\%^{40}Ar$ atm	$^{40}Ar^*/^{39}ArK$	±1σ	Age (Ma)	±1σ
SA04-13, J = 0.030017 ± 0.000054, Biotite (Western Limb)														
2.0	0.76	374.16	0.009	0.688	0.041	0.047	0.129	1.120	0.020	87.7	46.12	6.099	1568	139
2.1	1.27	71.442	0.006	0.417	0.037	0.054	0.097	0.096	0.030	39.1	43.54	0.880	1508	21
2.3	2.26	71.688	0.007	0.347	0.033	0.030	0.075	0.051	0.040	20.7	56.89	0.708	1797	14
2.5	5.61	74.785	0.005	0.283	0.020	0.010	0.171	0.034	0.028	13.3	64.93	0.445	1951	8
2.7	4.28	72.669	0.006	0.274	0.019	0.003	0.345	0.019	0.038	7.5	67.33	0.473	1995	8
2.8	4.84	69.384	0.005	0.267	0.022	0.002	0.351	0.006	0.065	2.7	67.61	0.355	2000	6
2.9	4.36	69.339	0.006	0.272	0.030	0.001	1.806	0.004	0.103	1.8	68.16	0.435	2009	8
3.0	5.71	68.500	0.005	0.264	0.022	0.002	0.340	0.003	0.141	1.2	67.74	0.382	2002	7
3.1	4.41	69.110	0.006	0.269	0.016	0.001	1.415	0.004	0.232	1.7	68.06	0.494	2008	9
3.2	6.20	68.152	0.005	0.271	0.024	0.001	0.410	0.002	0.177	1.0	67.55	0.377	1999	7
3.3	4.58	68.597	0.005	0.267	0.021	0.002	0.552	0.003	0.223	1.1	67.92	0.414	2005	7
3.4	4.34	68.723	0.005	0.271	0.023	0.001	0.631	0.004	0.141	1.7	67.64	0.404	2000	7
3.5	3.82	69.053	0.007	0.272	0.022	0.002	0.443	0.003	0.179	1.4	68.15	0.502	2009	9
3.6	5.93	67.991	0.005	0.268	0.014	0.001	0.674	0.002	0.203	0.9	67.49	0.355	1997	6
3.7	4.51	68.539	0.006	0.263	0.022	0.001	1.752	0.002	0.195	0.8	68.09	0.414	2008	7
3.8	4.97	68.358	0.005	0.268	0.028	0.001	0.632	0.002	0.233	0.9	67.84	0.382	2004	7
3.9	4.60	68.465	0.005	0.264	0.025	0.001	0.524	0.002	0.333	0.9	67.93	0.401	2005	7
4.0	5.42	68.006	0.005	0.258	0.014	0.002	0.339	0.002	0.154	0.9	67.51	0.327	1998	6
4.1	5.50	67.928	0.005	0.252	0.016	0.001	0.643	0.002	0.283	0.8	67.45	0.368	1997	7
4.2	2.81	68.823	0.006	0.258	0.035	0.002	0.884	0.003	0.357	1.3	68.03	0.508	2007	9
4.3	2.67	69.356	0.005	0.257	0.022	0.003	0.571	0.004	0.211	1.6	68.37	0.438	2013	8
4.4	3.57	68.938	0.006	0.249	0.029	0.002	0.609	0.003	0.135	1.4	68.09	0.422	2008	8
4.5	3.16	69.193	0.005	0.245	0.020	0.003	0.258	0.003	0.251	1.1	68.52	0.404	2016	7
4.7	1.90	69.592	0.006	0.245	0.034	0.002	0.626	0.005	0.207	2.0	68.26	0.498	2011	9
4.9	2.53	69.403	0.007	0.229	0.029	0.000	5.805	0.002	0.456	0.9	68.87	0.559	2022	10

Table 1.5 (continued)

Laser Power (%)	%^{39}Ar	^{40}Ar/^{39}Ar	±1σ	^{38}Ar/^{39}Ar	±1σ	^{37}Ar/^{39}Ar	±1σ	^{36}Ar/^{39}Ar	±1σ	%^{40}Ar atm	^{40}Ar*/^{39}ArK	±1σ	Age (Ma)	±1σ
SA04-11A, J = 0.030012 ± 0.000056, Biotite (Western Limb)														
2.0	0.20	73.253	0.019	0.266	0.106	0.152	0.125	0.161	0.054	64.5	26.02	2.449	1041	74
2.5	1.27	61.879	0.006	0.211	0.037	0.076	0.075	0.035	0.057	16.5	51.77	0.678	1691	14
2.8	4.73	68.465	0.005	0.197	0.025	0.008	0.135	0.003	0.157	1.2	67.71	0.354	2001	6
2.9	3.50	68.596	0.006	0.189	0.061	0.009	0.196	0.004	0.215	1.8	67.43	0.507	1996	9
3.0	4.14	68.996	0.006	0.194	0.021	0.009	0.117	0.004	0.208	1.8	67.81	0.513	2003	9
3.1	3.67	69.007	0.005	0.194	0.036	0.008	0.190	0.003	0.245	1.2	68.27	0.392	2011	7
3.2	4.87	68.915	0.005	0.200	0.020	0.010	0.106	0.004	0.129	1.8	67.74	0.381	2002	7
3.3	6.19	67.783	0.005	0.198	0.021	0.022	0.048	0.002	0.309	0.7	67.41	0.373	1996	7
3.4	3.66	68.613	0.005	0.199	0.032	0.021	0.083	0.003	0.302	1.1	67.97	0.402	2006	7
3.5	5.57	67.955	0.005	0.198	0.021	0.008	0.177	0.001	0.300	0.6	67.62	0.389	2000	7
3.6	5.06	68.480	0.005	0.190	0.022	0.006	0.155	0.003	0.166	1.2	67.76	0.392	2002	7
3.7	2.49	68.772	0.007	0.192	0.028	0.005	0.271	0.003	0.394	1.3	67.94	0.612	2005	11
3.8	5.14	67.697	0.005	0.197	0.018	0.004	0.099	0.001	0.286	0.6	67.36	0.378	1995	7
3.9	6.27	67.549	0.005	0.188	0.013	0.006	0.185	0.001	0.205	0.5	67.27	0.320	1993	6
4.0	6.13	67.649	0.005	0.193	0.025	0.007	0.148	0.001	0.400	0.6	67.35	0.383	1995	7
4.1	4.12	68.508	0.005	0.198	0.030	0.014	0.141	0.003	0.386	1.1	67.84	0.469	2004	8
4.2	5.58	67.923	0.005	0.191	0.037	0.009	0.126	0.001	0.743	0.4	67.73	0.416	2002	7
4.3	4.43	67.842	0.007	0.190	0.038	0.015	0.135	0.000	1.196	0.2	67.81	0.533	2003	10
4.4	3.99	67.932	0.008	0.193	0.025	0.076	0.049	0.001	1.355	0.2	67.88	0.600	2004	11
4.5	4.62	68.426	0.004	0.189	0.015	0.078	0.033	0.002	0.178	1.0	67.85	0.334	2004	6
4.7	4.59	67.173	0.005	0.193	0.024	0.092	0.031	−0.001	1.204	−0.1	67.30	0.436	1994	8
4.9	5.63	67.630	0.007	0.193	0.013	0.245	0.021	0.002	0.494	0.6	67.38	0.502	1995	9
5.3	4.15	68.499	0.005	0.183	0.021	0.069	0.057	0.002	0.354	0.9	67.97	0.402	2006	7

J, flux; 1σ, error quoted at 68% confidence

Results

U–Pb Zircon

U–Pb data for all 10 chemically abraded zircon grains from the Eastern Limb sample of the Merensky Reef (SA04-08) are only slightly discordant (0.03–0.57 %), yield overlapping $^{207}Pb/^{206}Pb$ dates ranging from 2056.44 to 2061.02 Ma (Table 1.4), and give a weighted $^{207}Pb/^{206}Pb$ average age of 2056.88 ± 0.41/0.41/6.0 Ma (2s, MSWD = 0.12) (Fig. 1.13a). The U–Pb errors are reported in the ± X/Y/Z format of Schoene et al. (2006) with internal error in the absence of all systematic errors (± X), tracer calibration error (± Y), and uncertainty due to decay-constant errors (± Z). The MSWD, mean square of the weighted deviates is a useful parameter for evaluating the probability that a weighted-mean population is statistically equivalent (Wendt and Carl 1991). For the Western Limb sample (SA04-13) that was previously dated by Scoates and Friedman (2008), the U–Pb data for the six new analyses of chemically abraded zircon grains are slightly discordant (0.04–0.45 %), yield overlapping $^{207}Pb/^{206}Pb$ dates ranging from 2056.80 to 2057.29 Ma (Table 1.4), and give a weighted average of 2057.04 ± 0.55/0.55/6.0 Ma (2s, MSWD = 0.10) (Fig. 1.13b). This age is older than the previously published age of 2054.4 ± 1.3 Ma by several million years and has significantly better precision. These differences are attributed to the combination of changes in analytical protocols at PCIGR since 2008 (Table 1.2), including the systematic use of EARTHTIME reference synthetic solutions, reduced blanks, and a revised internal value for the NBS-982 Pb standard. The U–Pb zircon ages for these samples of the Merensky Reef supersede the value published by Scoates and Friedman (2008) for SA04-13 as well as the preliminary results reported in abstract form for both samples in Scoates et al. (2011) and Scoates et al. (2012). These two U–Pb zircon ages for the Merensky Reef, 2056.88 ± 0.41 Ma and 2057.04 ± 0.55 Ma, are identical within uncertainty and are interpreted as the age of crystallization of this stratabound horizon. These results for two samples separated by ~ 310 km indicate that the Merensky Reef formed concurrently across the entire length of the Bushveld Complex.

U–Pb Rutile

Data from four concordant rutile fractions (5–10 grains each) from SA04-08 yield a weighted mean $^{207}Pb/^{206}Pb$ age of 2052.96 ± 0.61 Ma (2s, MSWD = 0.14) (Fig. 1.13c) and data from five concordant multigrain fractions from SA04-13 yield a weighted mean $^{207}Pb/^{206}Pb$ age of 2053.0 ± 2.74 Ma (2s, MSWD = 0.13) (Fig. 1.13d). Both of the U–Pb rutile ages are younger than the U–Pb zircon ages from their respective samples of Merensky Reef, most notably in the high-precision result of SA04-08. These slightly younger ages are interpreted as cooling ages resulting from Pb diffusion in rutile. For relatively fast cooling rates between 100 and 1000 °C/million years, estimated closure temperatures range from ~ 720–800 °C based on the formulation of Dodson (1973) and experimental Pb diffusion data for rutile from Cherniak

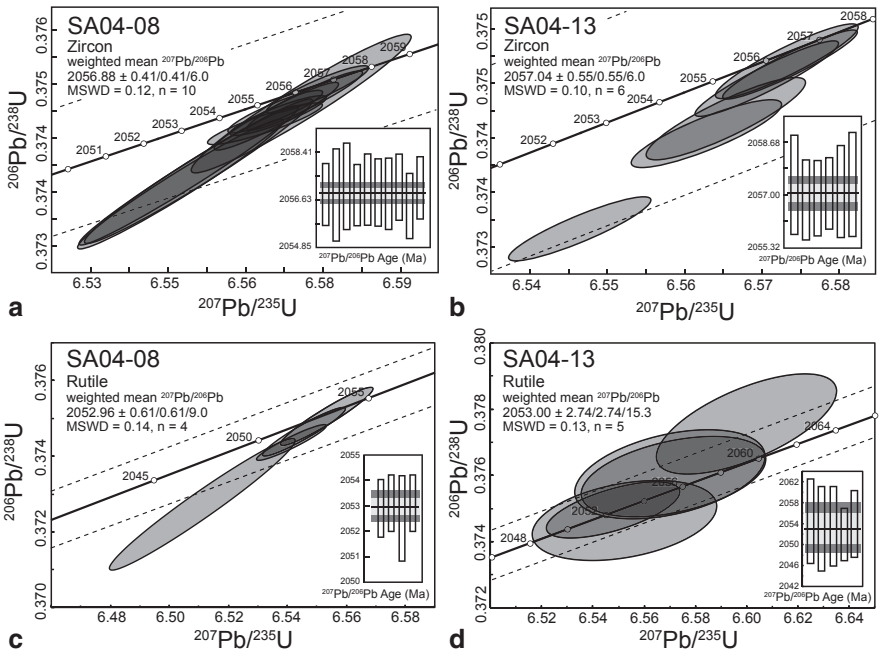

Fig. 1.13 Concordia diagrams showing U–Pb geochronological results for rutile and zircon from the Merensky Reef. **a** SA04-08 zircon. **b** SA04-13 zircon. **c** SA04-08 rutile. **d** SA04-13 rutile. Calculated weighted mean $^{207}Pb/^{206}Pb$ ages are indicated (uncertainty reported as 2s, including tracer calibration errors; decay-constant errors ignored). Each *shaded ellipse* indicates the analysis of a single zircon grain or 2–3 rutile grains (2s uncertainty). *Dashed* lines show the error bounds of the concordia curve. Inset in *lower right* of each panel show bar diagrams where each bar represents the analysis of a single fraction; the *horizontal black* line indicates the weighted mean age, the *light grey* band reflects the external reproducibility, and the *darker grey* band represents the total uncertainty. All dates Th-corrected for initial disequilibrium in $^{230}Th/^{238}U$ using Th/U [magma] = 3

(2000) (assuming cylindrical diffusion geometry and an average diffusion dimension of 125 μm). However, field-based studies consistently show that the closure temperature for rutile must be in the range of 400–450 °C (Schmitz and Bowring 2003). In this study, we assume that the ca. 2053 Ma ages from the U–Pb systematics of rutile indicate closure to Pb diffusion through a temperature of 450 °C following crystallization at ca. 2057 Ma.

U–Pb Apatite

Apatite from the two Merensky Reef samples has very low U concentrations (0.2–3 ppm) and large amounts of common Pb (< 23 % of the Pb in apatite is radiogenic) with correspondingly low $^{206}Pb/^{204}Pb$ (19.2–25.0) (Fig. 1.14a, Table 1.4). Age corrections for the initial common Pb composition were made using the results from co-existing leached plagioclase (Tam 2005; Scoates et al. 2006). The resulting U/Pb

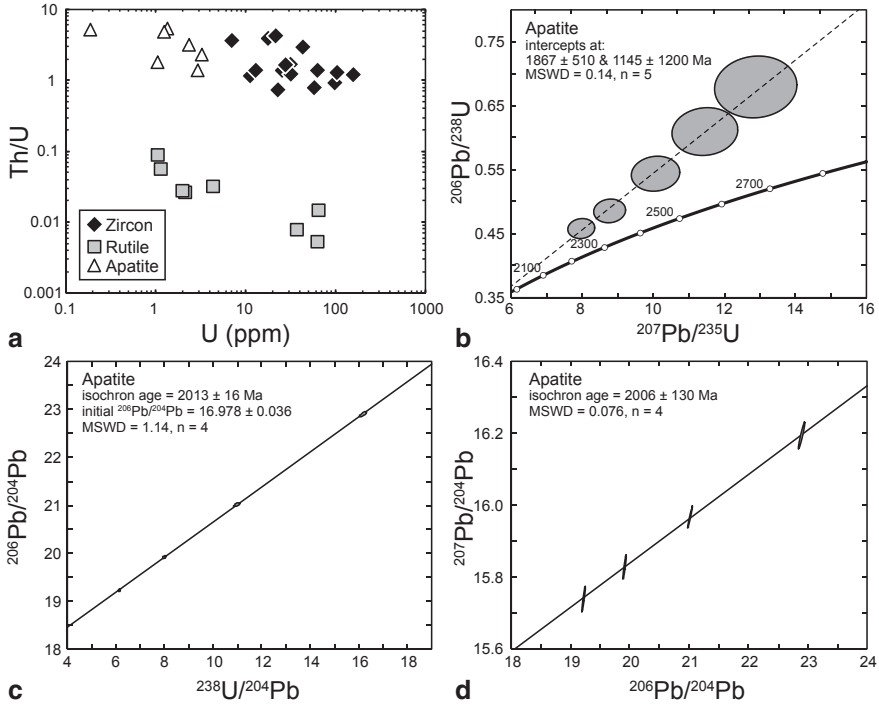

Fig. 1.14 Diagrams showing trace element and U–Pb geochronological results for apatite from the Merensky Reef. **a** Th/U vs. U (ppm) for all analyzed zircon, rutile, and apatite from the two samples of Merensky Reef in this study. Note that the plot axes are logarithmic to more effectively show the low U concentrations of apatite and rutile, and the very low Th/U of rutile. **b** Concordia diagram showing U–Pb geochronological results for apatite from SA04-08. **c** $^{206}Pb/^{204}Pb$ vs. $^{238}U/^{204}Pb$ plot showing results for apatite from SA04-08. **d** $^{207}Pb/^{204}Pb$ vs. $^{206}Pb/^{204}Pb$ plot showing results for apatite from SA04-08. Ellipses in **b**–**d** indicate 2s uncertainty. All plots produced using Isoplot (Ludwig 2003)

ages are extremely reversely discordant (up to 28 %; Fig. 1.14b), older than the U–Pb zircon crystallization age of the Merensky Reef (apatite $^{207}Pb/^{206}Pb$ dates = 2162–2467 Ma), and have large uncertainties. Reverse discordance is likely the result of U-loss at some time subsequent to crystallization (e.g., Kruger et al. 1998). The intercepts with concordia are highly imprecise with an upper intercept of ca. 1.9 Ga, close to the U–Pb zircon age, and a lower intercept of ca. 1.1 Ga. Use of a 1.1 Ga common Pb correction (Stacey and Kramers 1975) rather than the composition of the co-existing plagioclase yields concordant U/Pb ages. As they do not require a choice of initial Pb isotopic compositions, isochron plots (U–Pb, Pb–Pb) can also be used to investigate potential age relationships (Chamberlain and Bowring 2000). In a U–Pb isochron plot ($^{238}U/^{204}Pb$ vs. $^{206}Pb/^{204}Pb$), the resultant isochron age is 2013 ± 16 Ma (Fig. 1.14c). In a Pb–Pb isochron plot ($^{206}Pb/^{204}Pb$ vs. $^{207}Pb/^{204}Pb$), the isochron age is similar at 2006 ± 130 Ma (Fig. 1.14d), but with significantly larger uncertainty. Although these ages are likely to be inaccurate given the discordant

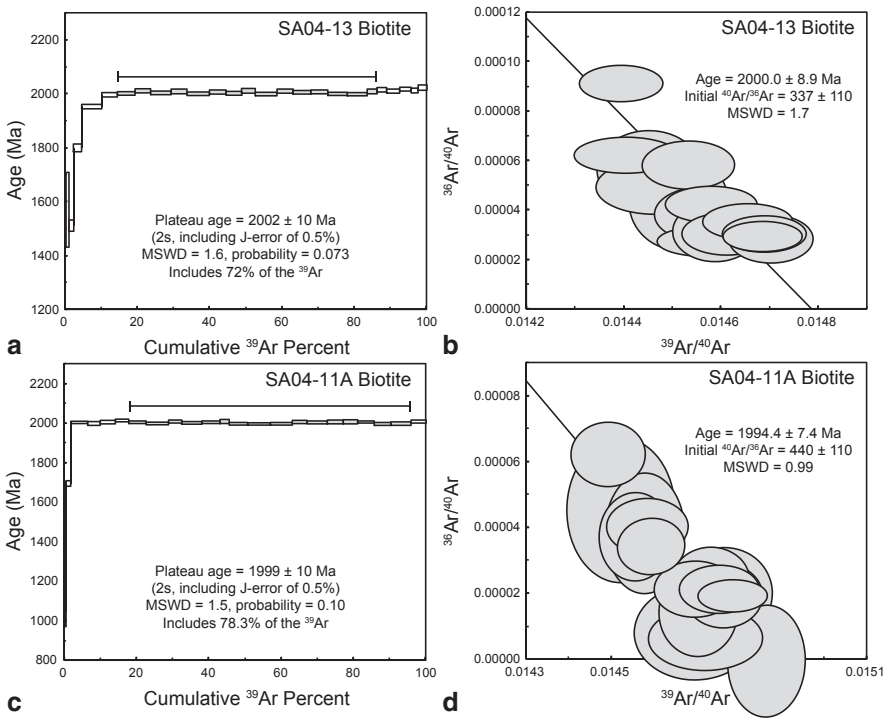

Fig. 1.15 Diagrams showing $^{40}Ar/^{39}Ar$ geochronological results for biotite from the Merensky Reef. **a** Apparent age spectrum for biotite from SA04-13, Eastern Limb. Grey-shaded boxes are those included in the plateau age calculation (range indicated by the *solid* line above the spectrum) and rejected steps are open boxes; 2s uncertainty level, errors include analytical uncertainty in J value. **b** Inverse isochron plot for biotite from SA04-13 (data-point error ellipses are 2s). **c** Apparent age spectrum for biotite from SA04-11A, Western Limb. **d** Inverse isochron plot for biotite from SA04-11A

nature of the U–Pb data and evidence for open-system behavior (Chamberlain and Bowring 2000), they may record hydrothermal resetting of the U–Pb systematics of apatite in the Merensky Reef at ca. 2.0 Ga, an event more strongly supported from the $^{40}Ar/^{39}Ar$ biotite results to follow.

Age spectra and inverse isochron diagrams for the two analyzed biotite samples (SA04-11A, SA04-13) from the Merensky Reef are shown in Fig. 1.15 with analytical data reported in Table 1.5. The plateau ages are 1999 ± 10 Ma (includes 78.3 % of the total ^{39}Ar released) and 2002 ± 10 Ma (includes 72 % of the total ^{39}Ar released), respectively, similar to the apatite U–Pb isochron age documented above. Both spectra have low apparent ages in the earliest stages of gas released (1–2 % for SA04-11A, 14 % for SA04-13). This is consistent with the early release of ^{39}Ar at the lowest extraction temperatures from minor chlorite interlayers in biotite that are artificially enriched in ^{39}Ar during irradiation and transfer from the surrounding biotite (Nomade et al. 2004). The inverse isochron ages, 1994.4 ± 7.4 Ma and 2000.0 ± 8.9 Ma, are indistinguishable from their respective plateau ages (Fig. 1.15).

Both isochrons have large uncertainties in initial $^{40}Ar/^{36}Ar$ with values that either overlap (sample SA04-13) with that determined for the precise estimate of atmospheric argon ($^{40}Ar/^{36}Ar = 298.56 \pm 0.31$; Lee et al. 2006; Mark et al. 2011) or that are higher (sample SA04-11A) indicative of excess ^{40}Ar introduced into the biotite at some time since crystallization (e.g., Kuiper 2002).

Crystallization and Cooling of the Merensky Reef and Bushveld Complex

The U–Pb zircon ages for the Merensky Reef, 2056.88 ± 0.41 Ma (Eastern Limb) and 2057.04 ± 0.55 Ma (Western Limb), are indistinguishable from each other and signify that the Reef is an intrusion-wide time marker in the crystallization history of the Bushveld Complex. Since its discovery in 1924 on the Farm Maandagshoek (Eastern Limb), the processes involved in the formation of the Merensky Reef have been the focus of intense study, controversy, and debate (e.g., Wagner 1929; Cousins 1969; Vermaak 1976; Ballhaus and Stumpfl 1986; Mathez 1995; Barnes and Maier 2002; Naldrett et al. 2009; Maier et al. 2013). From the perspective of chronology, the single most important feature of the Merensky Reef is that it is a regionally stratabound, but locally not stratiform, horizon with rocks of different composition comprising the footwall in different parts of the intrusion (e.g., mottled anorthosite in the Western Limb compared to layered norite from the Eastern Limb; Mitchell and Scoon 2007). This discontinuity ranges from kilometres at regional scale down to centimetres to metres at local scale (Eales and Cawthorn 1996), including the remarkable and persistent "potholes" (e.g., Ballhaus 1988; Carr et al. 1994; Smith and Basson 2006). Based on the results of this study, the absolute timing of the "Merensky discontinuity" is restricted to a relatively narrow interval (± 500,000 years or 0.025 %) at ca. 2057 Ma.

The duration of magmatism and cooling of the Bushveld Complex and associated mafic-ultramafic rocks across the northern Kaapvaal craton remains a fundamental question in the origin of the world's largest layered intrusion (Cawthorn and Walraven 1998; Cawthorn and Webb 2013). Whether the duration is 1, 5, or 10 Ma or longer, directly impacts estimates for rates of mantle melting, melt extraction, magma transport, magma flux, and cooling, and even potential environmental impacts (i.e., degassing associated with eruptive equivalents). Recent compilations of available geochronological data, combining in some cases published (analytical technique and data tables available) and unpublished (ages reported in abstracts with no associated data), suggest that most of the products of Bushveld-related magmatism may have crystallized in the interval of 2054–2061 Ma (Mapeo et al. 2004; Scoates and Friedman 2008; Yudovskaya et al. 2013; Rajesh et al. 2013). Comparison of recently published ages filtered for apparent uncertainties of less than ± 5–10 Ma, however, is problematic. The compiled ages include a wide range of minerals analyzed (e.g., zircon, baddeleyite, titanite, monazite, biotite), analytical techniques (e.g., TIMS [+ thermal evaporation], CA-TIMS, SHRIMP, LA-ICP-MS), and age interpretations (e.g., upper intercept $^{207}Pb/^{206}Pb$ ages from discordant results, weighted average $^{207}Pb/^{206}Pb$ ages for concordant results, Pb–Pb evaporation ages, $^{40}Ar/^{39}Ar$ plateau

or inverse isochron ages). Few studies involve common reference materials, reference values, and data reduction techniques. In this study alone, the ca. 2057 Ma ages for the Merensky Reef samples are ~2.5 million years older than our previously published result from the same materials, an age range that may encompass the crystallization and cooling of the entire thickness of the intrusion (Cawthorn and Webb 2013). Additionally, in the absence of a common technique referenced to the same standards, a true comparison of the published geochronological results for the Bushveld Complex and related rocks requires use of all external errors, including uncertainty in decay constants for the different isotopic systems (e.g., Min et al. 2000; Renne et al. 2010), an exercise that will inevitably lead to significantly larger and overlapping uncertainty. Determination of the absolute and precise duration of Bushveld-related magmatism will require careful application of the single-grain CA-ID-TIMS U–Pb zircon method, referenced to EARTHTIME synthetic reference solutions and common data reduction protocols, to select samples of previously dated samples and intrusions and to newly targeted samples.

There remain, as of yet, few published datasets for samples that directly date the timing of crystallization of mafic-ultramafic rocks from the Rustenburg Layered Suite. The CA-TIMS U-Pb zircon ages for the Merensky Reef, 2056.88 ± 0.41 and 2057.04 ± 0.55 Ma, establish the synchronous crystallization of this horizon within the uppermost Upper Critical Zone across the Bushveld Complex (see Fig. 1.8a). Olsson et al. (2010) report a U–Pb age of 2057.7 ± 1.6/6.4 Ma (± X/Z) for baddeleyite separated from a coarse-grained norite collected from the Marginal Zone (Eastern Limb). The date is an upper intercept $^{207}Pb/^{206}Pb$ age regressed through the slightly discordant (0.8–2.7 %) U–Pb results of four multi-grain (n = 10–23) baddeleyite fractions. This age is indistinguishable from the Merensky Reef ages within 2s uncertainty (internal errors only) and it is permissible that the lowermost part of the intrusion, from the Marginal Zone through the Upper Critical Zone, crystallized at ca. 2057 Ma. Direct comparison between the two datasets, however, is not possible at this time as Olsson et al. (2010) use an "in-house program" for data reduction and do not report use of EARTHTIME reference synthetic solutions to allow for interlaboratory comparison and calibration. The Merensky Reef ages are now closer to that of Buick et al. (2001) for titanite that formed in a retrogressed xenolith in the Upper Zone (Eastern Limb). Their U–Pb age of 2058.9 ± 0.8 Ma (2s, weighted $^{207}Pb/^{206}Pb$ age, internal errors) from three large multi-grain titanite fractions (5–12 mg) provide an indirect age of crystallization for the uppermost part of the Bushveld Complex that appears to be older than the Merensky Reef ages by at least 500,000 years assuming that there is no interlaboratory bias. Whether or not titanite growth in the calc-silicate protolith occurred during hydrothermal alteration related to Rooiberg magmatism with subsequent partial resetting during incorporation of the xenolith into the Bushveld magmas (Scoates and Friedman 2008) or that titanite growth indeed records the age of Bushveld magmatism remains to be tested.

This study demonstrates that it is possible to extract a wide range of chronometric minerals from single samples of cumulates from layered intrusions (Fig. 1.16). The resultant geochronologic information can be used to constrain crystallization and cooling histories for individual samples and by extension to entire intrusions.

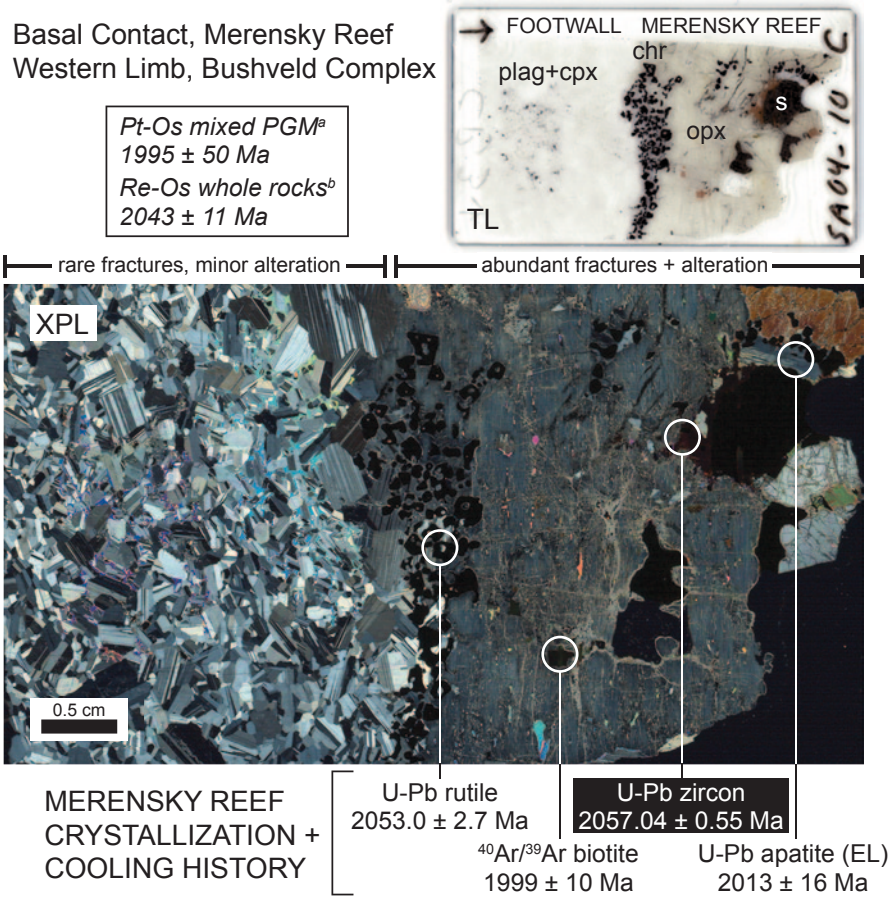

Fig. 1.16 Ages and petrologic setting of interstitial minerals dated from a sample of the Merensky Reef (SA04-13, Western Limb). A scanned thin section (45 × 25 mm) across the basal contact of the Reef is shown in the *upper right* of the figure in transmitted light (*TL*) for reference and in cross-polarized light (*XPL*) in the main part of the figure. The section displays the *uppermost* hanging wall leucogabbronorite to anorthosite (*left*), basal chromitite stringer (*centre*), and pegmatitic feldspathic orthopyroxenite (*right*). The *circled* areas indicate the approximate setting of interstitial minerals dated by the U–Pb method (zircon, rutile, apatite) and by the $^{40}Ar/^{39}Ar$ method (biotite); the ages determined in this study are shown below. Note that the apparent apatite age (U–Pb isochron) is from the Eastern Limb sample for comparison. This single sample captures the crystallization and cooling history of the Bushveld Complex from this locality of the Merensky Reef. Of note is the relatively pristine footwall plagioclase-rich rock with rare fractures and minor alteration compared to the Reef rock that is strongly fractured with abundant secondary alteration due to late hydrothermal alteration confined to the horizon of the Merensky Reef. Also indicated are previously published ages for the Merensky Reef package using different isotopic systems: (**a**) Merensky Reef (Western Limb), Pt–Os isochron age from mixed platinum group minerals (*PGM*), Coggon et al. (2012), (**b**) Bastard unit (Western Limb), whole rock Re–Os isochron for four poikilitic pyroxenites, Schoenberg et al. (1999). Abbreviations: *plag* plagioclase, *cpx* clinopyroxene, *chr* chromite, *opx* orthopyroxene, *s* sulphide

Most of the minerals analyzed in this study (zircon, apatite, biotite) demonstrably crystallized from late fractionated melt following crystallization of plagioclase-orthopyroxene-sulphide as they are found interstitial to these major rock-forming minerals (e.g., Figs. 1.2, 1.16) and they are observed in direct association with patches of intergrown quartz + alkali feldspar (Fig. 1.11). Rutile appears to have crystallized earlier, at higher temperatures, based on its presence as rims on chromite (Western Limb) that are poikilitically enclosed by plagioclase (Fig. 1.16) or as acicular crystals included in plagioclase, orthopyroxene and biotite (Eastern Limb). Following crystallization, the textures and mineralogy of the Merensky Reef sample in the western Bushveld Complex indicate that it was altered during fluid-rock interaction associated with subsequent hydrothermal activity. The footwall leucogabbronorite is unfractured with only trace patches of secondary minerals, whereas the feldspathic pegmatitic orthopyroxenite, particularly orthopyroxene, is very strongly fractured (sub-parallel to the basal contact defined by the chromitite stringer) with abundant secondary minerals (e.g., actinolite, epidote, talc, calcite) (Fig. 1.16). The margins of the coarse clots of base metal sulphides (pyrrhotite, pentlandite, chalcopyrite) have been replaced by secondary minerals, similar to the assemblages observed by Li et al. (2004) in their study of sulphide replacement from the UG2 and Merensky Reef (e.g., actinolite, epidote, calcite, magnetite). The presence of micro-fractures and evidence for interaction with an aqueous fluid (e.g., hydrous silicates, calcite) are particularly relevant to interpreting the chronologic information recorded by biotite. The relatively low closure temperature for Ar diffusion in biotite (~350–450 °C depending on cooling rate and diffusion dimension: Grove and Harrison 1996; Lee 1995; Nomade et al. 2004), combined with its weakly bound sheet structure, allow for the possibility of open-system behavior, argon loss, and resetting during fracture-controlled circulation of aqueous hydrothermal fluids. The anomalously young ca. 2000 Ma biotite $^{40}Ar/^{39}Ar$ ages for the Merensky Reef sample from Rustenburg (Western Limb), and the disturbed U–Pb systematics of apatite, are consistent with the effects of a post-magmatic hydrothermal event.

The thermal history of the Bushveld Complex, which is recorded in the mineral ages and their associated closure temperatures from the Merensky Reef, can be schematically divided into five stages (Fig. 1.17). Stage 1 is constrained by the high-precision U–Pb zircon results from both samples and dates the time of zircon crystallization (~2057 ± 0.5 Ma) from highly fractionated interstitial melt at near-solidus temperatures (1000 °C or less). Stage 2 involved rapid cooling (~125 °C/Ma) down to temperatures of ~400–450 °C by 2053 Ma defined by the U–Pb rutile ages from the same samples. The geochronologic evidence for rapid cooling supports the results of thermal modeling of the Bushveld Complex indicating that the 8 km-thick layered intrusion was emplaced and cooled from magma liquidus temperatures down to the Curie temperature of magnetite (580 °C) in less than 700,000 years (Cawthorn and Walraven 1998; Cawthorn and Webb 2013). Assuming that their respective closure temperatures are similar, the $^{40}Ar/^{39}Ar$ results from Nomade et al. (2004) for biotite from the UG2 chromitite, Western Limb (2042.4 ± 3.2 Ma), and from Cassata et al. (2009) for biotite from a gabbro near the MG-1 chromitite

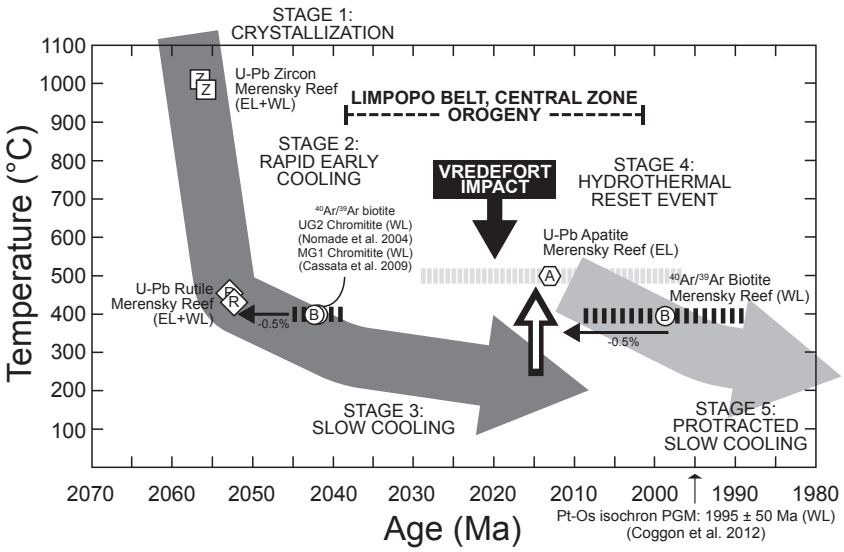

Fig. 1.17 Summary diagram showing a cooling curve for the Bushveld Complex as recorded by the different closure temperatures and ages for minerals from the Merensky Reef. The crystallization and cooling history of the Merensky Reef is divided into five stages that are constrained by U–Pb zircon results for crystallization of zircon at near-solidus temperatures (*Stage 1*), followed by rapid early cooling (*Stage 2*) defined by U–Pb rutile ages and from $^{40}Ar/^{39}Ar$ biotite results from Nomade et al. (2004) and Cassata et al. (2009) assuming a −0.5 % bias between the calibrations of the $^{40}Ar/^{39}Ar$ and U–Pb systems (indicated by the *arrow*), and initial slow cooling (*Stage 3*) below 300 °C. *Stage 4* is a postulated hydrothermal reset event of the Merensky Reef in the Western Limb of the Bushveld Complex recorded by the $^{40}Ar/^{39}Ar$ biotite ages (*arrow* indicates −0.5 % bias) and U–Pb isochron for apatite from this study. *Stage 5* involves protracted slow cooling from 300 to 150 °C over 600 Ma based on $^{40}Ar/^{39}Ar$ plagioclase results from Cassata et al. (2009). For reference, the timing of the Vredefort impact event to the south of the Bushveld Complex (ca. 2020 Ma: Kamo et al. 1996; Moser 1997) and orogeny in the Central Zone of the Limpopo Belt (Kramers and Mouri 2011) to the north are shown. Also shown is the Pt–Os isochron age from platinum group minerals from the Merensky Reef from Coggon et al. (2012). Analytical uncertainty on the U–Pb zircon and rutile ages is smaller than the symbol size. See text for discussion of specific closure temperatures. Abbreviations: *Z* zircon, *R* rutile, *A* apatite, *B* biotite, *WL* Western Limb, *EL* Eastern Limb

layer in the Critical Zone (2042 ± 2 Ma), are both consistent with the U–Pb rutile ages when an −0.5 % bias between the calibrations of the $^{40}Ar/^{39}Ar$ and U–Pb systems is applied (e.g., Min et al. 2000; Nomade et al. 2004; Renne et al. 2010) (Fig. 1.17). If the generally accepted bias of 1 % is used instead (Renne et al. 2010), then the $^{40}Ar/^{39}Ar$ biotite ages from these samples that occur in rocks stratigraphically beneath the Merensky Reef, is 2062 Ma, which is older than the U–Pb zircon ages from the Merensky Reef. Stage 3 marks the onset of slow cooling of the Bushveld Complex below 300 °C based on high-precision $^{40}Ar/^{39}Ar$ data and Ar diffusion kinetics from plagioclase from a Critical Zone gabbro that indicate protracted slow cooling (Stage 5) through crustal temperatures of 150–200 °C over 600 Ma (Cassata

et al. 2009). Stage 4 represents the hydrothermal event that locally affected the Merensky Reef in the sampled area of the Western Limb and that is supported both by the textural and mineralogical evidence for fracturing and secondary alteration of the reef and by the ca. 2000 Ma ages for biotite (Fig. 1.17). This hydrothermal event occurred in the interval from 2010 to 2020 Ma when considering a 0.5–1 % bias correction for comparison with the results from the U–Pb system. Mixed platinum group minerals (e.g., laurite, cooperate, sperrylite) yield a Pt–Os isochron age for the Merensky Reef of 1995 ± 50 Ma from mineral concentrates collected from the Frank Shaft (Coggon et al. 2012), ~9 km to the ESE of the Townlands Shaft (sample SA04-13 locality), and thus also appears to record the effects of this late, low-temperature hydrothermal event.

There are a number of potential heat sources that could have driven fluid flow and alteration in the Merensky Reef. Candidates include (1) the hydrothermal convection system of the Bushveld Complex itself, which is unlikely given that maintaining a hydrothermal system for 40–50 million years after initial emplacement even for the largest mafic layered intrusion on Earth vastly exceeds that now established even for giant gold deposits (e.g., Carlin, Nevada: Hickey et al. 2014) and porphyry systems where the duration of hydrothermal activity is constrained to be in the range of 10s of thousands of years up to 1–2 Ma (e.g., Cathles et al. 1997; Chiaradia et al. 2013), (2) hydrothermal activity that followed the Vredefort impact event at ca. 2020 Ma (Kamo et al. 1996; Moser 1997) (Fig. 1.17) when an asteroid struck the Kaapvaal craton 140 km to the south of the Bushveld Complex, ablating > 15 km of crust at the centre of the 70 km-diameter crater and producing a 300 km^2 thermal imprint, although impact-related metamorphism and hydrothermal circulation would likely have been limited to within the final crater itself (Turtle et al. 2003), and (3) hydrothermal circulation related to orogenesis at 2.02 ± 0.02 Ga (Fig. 1.17) in the Central Zone of the Limpopo Belt on the northern edge of the Kaapvaal craton that was associated with zones of transcurrent shearing at high-grade granulite-facies metamorphism (e.g., McCourt and Armstrong 1998; Buick et al. 2007; Kramers and Mouri 2011), which is potentially the most likely scenario given the presence of a regional heat source and stress field. Whether late hydrothermal activity is restricted only to the Merensky Reef in the Rustenburg area or whether it is more widespread will require detailed chronological studies of samples from across the Bushveld Complex (Western, Eastern, and Northern limbs) with multiple chronometric minerals.

Summary and Future Directions

Layered intrusions have long been considered to provide the clearest natural examples of the effects of fractional crystallization of magmas (Wager and Brown 1967). They formed throughout Earth history and they preserve rock records in such remarkable igneous bodies as the Bushveld Complex, Stillwater Complex, Muskox intrusion, and Skaergaard intrusion, and in innumerable smaller bodies exposed in

crustal sections worldwide, that provide a template for how mafic magma differentiates in the Earth's crust. Yet, comprehensive age information involving integration of high-precision absolute ages, duration of magmatism, and cooling history is still lacking for most of them.

In this contribution, we have provided the field and petrologic context for identifying samples from layered intrusions with the potential to contain a wide array of U–Th–Pb-bearing accessory minerals, and K-bearing minerals, that are dateable by modern mass spectrometric techniques, especially zircon by the chemical abrasion-TIMS, or CA-TIMS, technique (Mattinson 2005). Prospective samples from mafic and ultramafic cumulates are those with heterogeneous textures, not equigranular or adcumulus textures, and with macroscopic evidence for interstitial minerals, typically poikilitic plagioclase, that crystallized from evolved interstitial melt. From the microscopic perspective, such samples may contain interstitial patches with minerals that crystallized from highly fractionated melt (e.g., quartz, alkali feldspar) at near-solidus temperatures. Dateable accessory minerals (e.g., zircon, baddeleyite, rutile, apatite), although typically present in minute quantities (a few tens to hundreds of grains per 10–20 kg of sample), are in sufficient quantity to provide high-precision geochronologic results where individual grains or grain fragments can be processed and analyzed. Single samples, separated by ~300 km, of the platiniferous Merensky Reef from the Bushveld Complex of South Africa can yield multiple chronometric minerals with different closure temperatures (e.g., Pb diffusion in zircon, rutile, and apatite; $^{40}Ar^*$ in biotite) that allow for the cooling histories of the samples, and by extrapolation that of the entire Bushveld Complex, to be established. And through the efforts of EARTHTIME, with isotopic tracers, U–Pb synthetic standards, and new data collection and reduction software available to the community to alleviate intra-laboratory bias, reductions in Pb blanks, and carefully characterized Pb fractionation of standard materials, it is possible to achieve internal uncertainties on the U–Pb analysis of single zircon grains to significantly less than 0.1 %. This now means that uncertainties of ± 500,000 years or less are attainable for Paleoproterozoic to Archean layered intrusions (e.g., Bushveld Complex, Stillwater Complex) and potentially ± 10,000–20,000 years for Phanerozoic intrusions, thus approaching the timescales of residence, magma storage, and differentiation of magmas in the crust (Turner and Costa 2007; Cooper and Kent 2014).

The discovery that zircon is more common in mafic-ultramafic rocks of layered intrusions than previously recognized provides the petrologic community with a wide range of new geochemical tools to decipher and quantify the processes that operate during their crystallization and consolidation. Careful petrographic studies involving the textural setting of zircon in cumulates and detailed SEM-BSE and SEM-CL imaging are required to fully document the timing of zircon saturation and crystal growth relative to other interstitial minerals (e.g., biotite, quartz, alkali feldspar, apatite, rutile). Because of the low abundance of zircon (<< 1 vol%) in mafic-ultramafic cumulates, the probability of intersecting crystals in thin sections is relatively small. An alternative approach to characterizing the distribution of zircon, and association with major cumulus minerals and pockets of trapped interstitial melt, is through the use of high-resolution X-ray computed tomography,

a technique that has revolutionized our understanding of the spatial relationship of platinum group minerals to sulphide blebs and chromite grains in PGE-rich reefs from layered intrusions (e.g., Merensky Reef, Bushveld Complex; J-M Reef, Stillwater Complex; Platinova Reef, Skaergaard intrusion) (Godel et al. 2010; Godel et al. 2014).

In addition to U+Th, zircon can also incorporate a wide range of different elements in trace to wt% amounts, including Ti, Hf, and the rare earth elements (REE), through a variety of substitution mechanisms (e.g., Harley and Kelly 2007; Nardi et al. 2013). This will allow for future studies on the trace element and isotopic composition of zircon from layered intrusions that can be compared to information derived from the higher temperature cumulus minerals and thus potentially serve to map-out the complete geochemical evolution of cumulates from liquidus to solidus. The Ti content of zircon coexisting with rutile, which has a strong dependence on temperature (Watson et al. 2006; Ferry and Watson 2007; Fu et al. 2008), can be measured in situ by LA-ICP-MS or SHRIMP from zircon in thin sections or out-of-context zircon grains from mineral separates, so that the temperature at which zircon crystallized in cumulates can now be quantified. The REE contents of zircon from layered intrusions can be used to reconstruct the geochemical evolution of the fractionated melt from which it crystallized and help identify melt compositions and magma sources (e.g., Belousova et al. 2002; Claiborne et al. 2010; Nardi et al. 2013), which is a rapidly expanding field of research, especially for zircon in felsic rocks.

New methods have been developed to allow for the simultaneous acquisition of high-precision U–Pb geochronology and zircon trace element analysis (U–Pb TIMS-TEA, Schoene et al. 2010), a technique that can be expanded to include baddeleyite, titanite, apatite, rutile, monazite, and xenotime, if they are found to be present in cumulates under investigation. The radiogenic isotopic systematics of zircon (Lu–Hf, Sm–Nd) (e.g., Kinny and Maas 2003; Scherer et al. 2007; Barboni et al. (2013) and oxygen isotope signatures of zircon (Valley 2003; Valley et al. 2005) can provide information on variations in crustal contamination, crustal residency, and protolith and source compositions from the analysis (LA-MC-ICP-MS, SHRIMP) of single grains from cumulates sampled throughout the stratigraphic thicknesses of individual intrusions (e.g., Bushveld Complex, Zirakparvar et al. 2014). It is now also possible to conduct correlated microanalysis of zircon (trace elements, oxygen isotopes, Hf isotopes, U–Th–Pb geochronology) (Cavosie et al. 2006), which would be advantageous when zircon populations in layered intrusions are complex and spatial resolution is required (e.g., inherited cores, cracks, radiation-damaged zones), although with the trade-off of reduced precision. Depending on the particular layered intrusion and its specific emplacement and crystallization history, it may even be possible to identify the different types of zircon that are now recognized in arc plutons (e.g., autocrysts, antecrysts, xenocrysts, inherited zircon; Miller et al. 2007).

By combining these advances in technologies and applications with our current capabilities of determining high-precision crystallization and cooling ages from a range of rock types in layered intrusions, Archean to Cenozoic, the next 10–15 years of research will undoubtedly provide many important, and unexpected, discoveries based on the geochronology of layered intrusions with implications for the

evolution of mafic magmatism in the Earth's crust. The geochronological tools are now available to address whether major layered intrusions are assembled in discrete magmatic episodes, whether all layered intrusions are simple stratigraphic sequences of cumulates with the oldest rocks at the base and the youngest at the top near the roof, whether discontinuities in cumulate sequences can be identified and time gaps measured, and whether their associated mineral deposits are directly related to the crystallization of their immediate host rocks or formed or were modified at some temporally resolvable time after crystallization. Answers to these questions will directly impact our understanding of the emplacement, crystallization, and cooling of these exceptional bodies of igneous rocks.

Acknowledgements

We thank Wolf Maier for leading a superb field trip on the Eastern Limb of the Bushveld Complex and to Anglo Platinum for allowing access and sampling in the West Mine, Rustenburg Section of the Western Limb of the Bushveld Complex. Our thanks to Bill Meurer for helping in initiating selection and collection of geochronology samples from the Stillwater Complex many summers ago. We are extremely grateful for the assistance, input, advice, and comments from Richard Friedman, who has been instrumental in maintaining the daily operation of the U–Pb geochronology stream at the PCIGR for so many years. We thank Hai Lin for help with sample processing (crushing, Wilfley Table, heavy liquids, and magnetic separation) and Yeena Lin for careful clean lab chemistry. Thanks to Mati Raudsepp for his expertise and management of the scanning electron microscope and associated cathodoluminescence detector at UBC. Dominique Weis has provided many useful ideas over the years on isotopic systematics and mass spectrometry that have significantly improved our U–Pb TIMS geochronology capabilities. Tom Ullrich conducted the $^{40}Ar/^{39}Ar$ analyses and data reduction. Many thanks to Jon Scoates for a timely and detailed review of the manuscript. We greatly appreciate the insightful review comments of Kevin Chamberlain, Wolf Maier, and an anonymous reviewer, in addition to the efficient editorial handling by Bernard Charlier. Funding for this study has been provided through a NSERC CGS-M and PGS-D awarded to Corey Wall and NSERC Discovery Grants awarded to Dr. James Scoates.

References

Alapieti T (1982) The Koillismaa layered igneous complex, Finland—its structure, mineralogy and geochemistry, with emphasis on the distribution of chromium. Geol Surv Finl Bull 319:116

Alapieti TT, Kujanpää J, Lahtinen JJ, Papunen H (1989) The Kemi stratiform chromitite deposit, northern Finland. Econ Geol 84:1057–1077 doi:10.2113/gsecongeo.84.5.1057

Amelin Y, Zaitsev AN (2002) Precise geochronology of phoscorites and carbonatites: the critical role of U-series disequilibrium in age interpretations. Geochim Cosmochim Acta 66:2399–2419. doi:10.1016/S0016-7037(02)00831-1

Amelin Y, Davis WJ (2006) Isotopic analysis of lead in sub-nanogram quantities by TIMS using a ^{202}Pb–^{205}Pb spike. J Anal At Spectrom 21:1053–1061. doi:10.1039/b606842a

Amelin YV, Heaman LM, Semenov VS (1995) U-Pb geochronology of layered mafic intrusions in the eastern Baltic Shield: implications for the timing and duration of Paleoproterozoic continental rifting. Precambrian Res 75:31–46. doi:10.1016/0301-9268(95)00015-W

Ballhaus CG (1988) Potholes of the Merensky Reef at Brakspruit Shaft, Rustenburg Platinum Mines: primary disturbances in the magmatic stratigraphy. Econ Geol 83:1140–1158. doi:10.2113/gsecongeo.83.6.1140

Ballhaus CG, Stumpfl EF (1986) Sulfide and platinum mineralization in the Merensky Reef: evidence from hydrous silicates and fluid inclusions. Contrib Mineral Petrol 94:193–204. doi:10.1007/BF00592936

Barboni M, Schoene B, Ovtcharova M, Bussy F, Schaltegger GA (2013) Timing of incremental pluton construction and magmatic activity in a back-arc setting revealed by ID-TIMS U/Pb and Hf isotopes on complex zircon grains. Chem Geol 340:76–93. doi:10.1016/j.chemgeo.2012.12.011

Barfod GH, Otero O, Albarède F (2003) Phosphate Lu-Hf geochronology. Chem Geol 200:241–253. doi:10.1016/S0009-2541(03)00202-X

Barkov AY, Savchenko YE, Men'shikov YP, Barkova LP (1996) Loveringite from the Last-Yavr mafic-ultramafic intrusion, Kola Peninsula; a second occurrence in Russia. Nor Geol Tidsskr 76:115–120

Barnes S-J, Maier WD (2002) Platinum-group elements and microstructures of normal Merensky Reef from Impala Platinum Mines, Bushveld Complex. J Petrol 43:103–128. doi:10.1093/petrology/43.1.103

Belousova EA, Griffin WL, O-Reilly SY, Fisher NI (2002) Igneous zircon: trace element composition as an indicator of source rock type. Contrib Mineral Petrol 143:602–622. doi:10.1007/s00410-002-0364-7

Boehnke P, Watson EB, Trial D, Harrison RM, Schmitt AK (2013) Zircon saturation re-revisited. Chem Geol 351:324–334 doi:10.1016/j.chemgeo.2013.05.02

Boudreau A (2011) The evolution of texture and layering in layered intrusions. Int Geol Rev 53:330–353. doi:10.1080/00206814.2010.496163

Boudreau AE, Hoatson DM (2004) Halogen variations in the Paleoproterozoic layered mafic-ultramafic intrusions of the East Kimberley, Western Australia: implications for platinum group element mineralization. Econ Geol 99:1015–1026. doi:10.2113/gsecongeo.99.5.1015

Boudreau AE, Mathez EA, McCallum IS (1986) Halogen geochemistry of the Stillwater and Bushveld complexes: evidence for transport of the platinum-group elements by Cl-rich fluids. J Petrol 27:967–986. doi:10.1093/petrology/27.4.967

Bowen NL (1928) The evolution of igneous rocks. Dover Publications, New York, NY p 332

Bowring JF, McLean NM, Bowring SA (2011) Engineering cyber infrastructure for U-Pb geochronology: Tripoli and U-Pb_Redux. Geochem Geophys Geosystems 12:(Q0AA19), p 19. doi:10.1029/2010GC003479

Bristow DG, Cawthorn RG, Harmer J, Lee CA, Tegner C, Vijoen MJ, Walraven F, Wilson JR (1993) Field excursion to the Bushveld Complex, 11–17th Sept 1993. Excursion guide—symposium on layering in igneous complexes, p 59

Buchanan PC, Reimold WU, Koeberl C, Kruger FJ (2002) Geochemistry of intermediate to siliceous volcanic rocks of the Rooiberg Group, Bushveld Magmatic Province, South Africa. Contrib Mineral Petrol 144:131–143. doi:10.1007/s00410-002-0386-1

Buick IS, Maas R, Gibson R (2001) Precise U-Pb titanite age constraints on the emplacement of the Bushveld Complex, South Africa. J Geol Soc Lond 158:3–6. doi:10.1144/jgs.158.1.3

Buick IS, Hermann J, Maas R, Gibson RL (2007) The timing of sub-solidus hydrothermal alteration in the Central Zone, Limpopo Belt (South Africa): constraints from titanite U–Pb geochronology and REE partitioning. Lithos 98:97–117. doi:10.1016/j.lithos.2007.02.002

Cabella R, Gazzotti M, Lucchetti G (1997) Loveringite and baddeleyite in layers of chromian spinel from the Bracco ophiolitic unit, Northern Apennines, Italy. Can Mineral 35:899–908

Cameron EN (1979) Titanium-bearing oxide minerals of the critical zone of the eastern Bushveld Complex. Am Mineral 64:140–150

Campbell IH (1987) Distribution of orthocumulate textures in the Jimberlana intrusion. J Geol 95:35–53

Campbell IH, Kelly PR (1978) The geochemistry of loveringite, a uranium–rare-earth-bearing accessory phase from the Jimberlana intrusion of Western Australia. Mineral Mag 42:187–193

Campbell IH, Naldrett AJ, Barnes SJ (1983) A model for the origin of the platinum-rich sulfide horizons in the Bushveld and Stillwater complexes. J Petrol 24:133–165. doi: 10.1093/petrology/24.2.133

Carr HW, Groves DI, Cawthorne RG (1994) The importance of synmagmatic deformation in the formation of Merensky Reef potholes in the Bushveld Complex. Econ Geol 89:1398–1410. doi:10.2113/gsecongeo.89.6.1398

Cassata WS, Renne PR, Shuster DL (2009) Argon diffusion in plagioclase and implications for thermochronology: a case study from the Bushveld Complex, South Africa. Geochim Cosmochim Acta 73:6600–6612. doi:10.1016/j.gca.2009.07.017

Cathles LM, Erendi AHJ, Barrie T (1997) How long can a hydrothermal system be sustained by a single intrusive event? Econ Geol 92:766–771. doi:10.2113/gsecongeo.88.8.1977

Cavosie AJ, Valley JW, Wilde SA, EIMF (2006) Correlated microanalysis of zircon: Trace element, $\delta^{18}O$, and U–Th–Pb isotopic constraints on the igneous origin of complex >3900 Ma detrital grains. Geochim Cosmochim Acta 70:5601–5616. doi:10.1016/j.gca.2006.08.011

Cawthorn RG (ed) (1996) Layered intrusions (Developments in Petrology 15). Elsevier, Amsterdam, The Netherlands p 531

Cawthorn RG, Boerst K (2006) Origin of the pegmatitic pyroxenite in the Merensky unit, Bushveld Complex, South Africa. J Petrol 47:1509–1530. doi:10.1093/petrology/egl017

Cawthorn RG, Walraven F (1998) Emplacement and crystallization time for the Bushveld Complex. J Petrol 39:1669–1687. doi:10.1093/petroj/39.9.1669

Cawthorn RG, Webb SJ (2013) Cooling of the Bushveld Complex, South Africa: implications for paleomagnetic reversals. Geology 41:687–690. doi:10.1130/G34033.1

Cawthorn RG, Barnes SJ, Ballhaus C, Malitch KN (2005) Platinum group element, chromium, and vanadium deposits in mafic and ultramafic rocks. In: Hedenquist JW et al. (eds) Economic Geology (One Hundredth Anniversary Volume), Littleton, CO pp 215–250 Society of Economic Geologists, Inc.

Chamberlain KR, Bowring SA (2000) Apatite–feldspar U–Pb thermochronometer: a reliable, mid-range (~450°C), diffusion-controlled system. Chem Geol 172:173–200. doi:10.1016/S0009-2541(00)00242-4

Chamberlain KR, Schmitt AK, Swapp SM, Harrison TM, Swoboda-Colberg N, Bleeker W, Peterson TD, Jefferson CW, Khudoley AK (2010) In situ U–Pb SIMS (IN-SIMS) micro-baddeleyite dating of mafic rocks: method with examples. Precambrian Res 183:379–387. doi:10.1016/j.precamres.2010.05.004

Chang Z, Vervoort JD, McClelland WC, Knaack C (2006) U-Pb dating of zircon by LA-ICP-MS. Geochem Geophys Geosystems 7:(Q05009), p 14. doi:10.1029/2005GC001100

Cherniak DJ (1993) Lead diffusion in titanite and preliminary results on the effects of radiation damage on Pb transport. Chem Geol 110:177–194. doi:10.1016/0009-2541(93)90253-F

Cherniak DJ (2000) Pb diffusion in rutile. Contrib Mineral Petrol 139:198–207

Cherniak DJ (2010) Diffusion in accessory minerals: zircon, titanite, apatite, monazite and xenotime. In: Zhang Y, Cherniak DJ (eds) Diffusion in minerals and melts, Reviews in Mineralogy and geochemistry, Chantilly, VA vol. 72. pp 827–869. doi:10.2138/rmg.2010.72.18 The Mineralogical Society of America

Cherniak DJ, Watson EB (2000) Pb diffusion in zircon. Chem Geol 172:5–24. doi:10.1007/PL00007671

Cherniak DJ, Watson EB (2003) Diffusion in zircon. In: Hanchar JM, Hoskin PWO (eds) Zircon, Reviews in Mineralogy and Geochemistry, Washington, DC vol. 53. pp 113–143. doi:10.2113/0530113 The Mineralogical Society of America

Cherniak DJ, Lanford WA, Ryerson FJ (1991) Lead diffusion in apatite and zircon using ion implantation and Rutherford backscattering techniques. Geochim Cosmochim Acta 55:1663–1673. doi:10.1016/0016-7037(91)90137-T

Chew DM, Petrus JA, Kamber BS (2014) U–Pb LA–ICPMS dating using accessory mineral standards with variable common Pb. Chem Geol 363:185–199. doi:10.1016/j.chemgeo.2013.11.006

Chiaradia M, Schaltegger U, Spiking R, Wotzlaw J-F, Ovtcharova M (2013) How accurately can we date the duration of magmatic-hydrothermal events in porphyry systems?—an invited paper. Econ Geol 108:565–584. doi:10.2113/econgeo.108.4.565

Chutas NI, Bates E, Prevec SA, Coleman DS, Boudreau AE (2012) Sr and Pb isotopic disequilibrium between coexisting plagioclase and orthopyroxene in the Bushveld Complex, South Africa: microdrilling and progressive leaching evidence for sub-liquidus contamination within a crystal mush. Contrib Mineral Petrol 163:653–668. doi:10.1007/s00410-011-0691-7

Claiborne LL, Miller CF, Wooden JL (2010) Trace element composition of igneous zircon: a thermal and compositional record of the accumulation and evolution of a large silicic batholith, Spirit Mountain, Nevada. Contrib Mineral Petrol 160:511–531. doi:10.1007/s00410-010-0491-5

Coggon JA, Nowell GM, Pearson DG, Oberthür T, Lorand J-P, Melcher F, Parman SW (2012) The ^{190}Pt–^{186}Os decay system applied to dating platinum-group element mineralization of the Bushveld Complex, South Africa. Chem Geol 302–303:48–60. doi:10.1016/j.chemgeo.2011.10.015

Compston W, Williams IS, Meyer C (1984) U–Pb geochronology of zircons from lunar breccia 73217 using a sensitive high mass-resolution ion microprobe. J Geophys Res Suppl 89:B525–B534

Condon D, Schoene B, Bowring S, Parrish R, Mclean N, Noble S, Crowley Q (2007) Earthtime: Isotopic tracers and optimized solutions for high-precision U-Pb ID-TIMS geochronology. American Geophysical Union, Fall Meeting 2007 [abstract #V41E-06].

Condon DJ, McKean N, Noble SR, Bowring SA (2010) Isotopic composition ($^{238}U/^{235}U$) of some commonly used uranium reference materials. Geochim Cosmochim Acta 74:7127–7143. doi:10.1016/j.gca.2010.09.019

Cooper KM, Kent AJR (2014) Rapid remobilization of magmatic crystals in cold storage. Nature 506:480–483. doi:10.1038/nature12991

Corfu F, Krogh TE, Ayres LD (1985) U–Pb zircon and sphene geochronology of a composite Archean granitoid batholith, Favorable Lake area, northwestern Ontario. Can J Earth Sci 22:1436–1451. doi:10.1139/e85-150

Corfu F, Hanchar JM, Hoskin PWO, Kinny P (2003) Atlas of zircon textures. In: Hanchar JM, Hoskin PWO (eds) Zircon, Reviews in Mineralogy and Geochemistry, Washington, DC vol. 53. pp 469–500. doi:10.2113/0530469 The Mineralogical Society of America

Cottle JM, Horstwood MSA, Parrish RR (2009) A new approach to single shot laser ablation analysis and its application to in situ Pb/U geochronology. J Anal At Spectrom 24:1355–1363. doi:10.1039/B821899D

Cottle JM, Kylander-Clark AR, Vrijmoed JC (2012) U-Th/Pb geochronology of detrital zircon and monazite by single shot laser ablation inductively coupled plasma mass spectrometry (SS-LA-ICPMS). Chem Geol 332–333:136–147. doi:10.1016/j.chemgeo.2012.09.035

Cousins CA (1969) The Merensky Reef of the Bushveld Igneous Complex. In: Wilson HDB (ed) Magmatic ore deposits: a symposium. Economic Geology Publishing Company, Lancaster, PA pp 239–251

Das A, Davis DW (2010) Response of Precambrian zircon to the chemical abrasion (CA-TIMS) method and implications for improvement of age determinations. Geochim Cosmochim Acta 74:5333–5348. doi:10.1016/j.gca.2010.06.029

Davis DW, Sutcliffe RH (1985) U-Pb ages from the Nipigon plate and northern Lake Superior. Geol Soc Am Bull 96:1572–1579. doi:10.1130/0016-7606(1985)96&#X1;1572:UAFTNP>2.0.CO;2

Davis DW, Williams IS, Krogh TE (2003) Historical developments of zircon geochronology. In: Hanchar JM, Hoskin PWO (eds) Zircon, Reviews in Mineralogy and Geochemistry, Washington, DC vol. 53. pp 145–181. doi:10.2113/0530145 The Mineralogical Society of America

DePaolo DJ (1985) Isotopic studies of processes in mafic magma chambers: I. The Kiglapait intrusion, Labrador. J Petrol 26:925–951. doi:10.1093/petrology/26.4.925

DePaolo DJ, Wasserburg GJ (1979) Sm-Nd age of the Stillwater Complex and the mantle evolution curve for neodymium. Geochim Cosmochim Acta 43: 999–1008. doi:10.1016/0016-7037(79)90089-9

Dickin AP (2005) Radiogenic isotope geology, 2nd edn. Cambridge University Press, Cambridge, UK p 512

Dodson MH (1973) Closure temperature in cooling geochronological and petrological systems. Contrib Mineral Petrol 40:259–274. doi:10.1007/BF00373790

Dodson MH (1978) A linear method for second-degree interpolation in cyclical data collection. J Phys E Sci Instrum 11:296

Eales HV, Cawthorn RG (1996) The Bushveld Complex. In: Cawthorn RG. (ed) Layered intrusions. Elsevier Science B.V., Amsterdam, pp 181–229. doi:10.1016/S0167-2894(96)80008-X

Ernst RE, Buchan KL (2001) Large mafic magmatic events through time and links to mantle-plume heads. Geol Soc Am Spec Pap 352:483–575. doi:10.1130/0-8137-2352-3.483

Ewing RC, Meldrum A, Wang L, Weber WJ, Corrales LR (2003) Radiation effects in zircon. In: Hanchar, JM, Hoskin PWO (eds) Zircon, Reviews in Mineralogy and Geochemistry, Washington, DC vol. 53. pp 387–425. doi:10.2113/0530387 The Mineralogical Society of America

Faure G, Mensing TM (2005) Isotopes: principles and applications, 3rd edn. Wiley, Hoboken, NJ p 928

Fenton MD, Faure G (1969) The age of the igneous rocks of the Stillwater Complex of Montana. Geol Soc Am Bull 80:1599–1604

Ferreira-Filho CF, Kamo SL, Fuck RA, Krogh TE, Naldrett JA (1994) Zircon and rutile U-Pb geochronology of the Niquelândia layered mafic and ultramafic intrusion, Brazil: constraints for the timing of magmatism and high grade metamorphism. Precambrian Res 68:241–255. doi:10.1016/0301-9268(94)90032-9

Ferry JM, Watson EM (2007) New thermodynamic models and revised calibrations for the Ti-in-zircon and Zr-in-rutile thermometers. Contrib Mineral Petrol 154:429–437. doi:10.1007/s00410-007-0201-0

Finch RJ, Hanchar JM (2003) Structure and chemistry of zircon and zircon-group minerals. In: Hanchar JM, Hoskin PWO (eds) Zircon, Reviews in Mineralogy and Geochemistry, Washington, DC vol. 53. pp 1–25. doi:10.2113/0530001 The Mineralogical Society of America

Fisher CM, Longerich HP, Jackson SE, Hanchar JM (2010) Data acquisition and calculation of U–Pb isotopic analyses using laser ablation (single collector) inductively coupled plasma mass spectrometry. J Anal Atomic Spectrom 25:1905–1920: doi:10.1039/c004955g

Francis D (2011) Columbia Hills—an exhumed layered igneous intrusion on Mars? Earth Planet Sci Lett 310:59–64. doi:10.1016/j.epsl.2011.08.003

French JE, Heaman LM, Chacko T (2002) Feasibility of chemical U–Th–total Pb baddeleyite dating by electron microprobe. Chem Geol 188:85–104. doi:10.1016/S0009-2541(02)00074-8

Frei D, Gerdes A (2009) Precise and accurate in situ U–Pb dating of zircon with high sample throughput by automated LA-SF-ICP-MS. Chem Geol 261:261–270. doi:10.1016/j.chemgeo.2008.07.025

Frost BR, Chamberlain KR, Schumacher JC (2000) Sphene (titanite): phase relations and role as a geochronometer. Chem Geol 172:131–148. doi:10.1016/S0009-2541(00)00240-0

Fu B, Page FZ, Cavosie AJ, Fournelle J, Kita NT, Lackey JS, Wilde SA, Valley JW (2008) Ti-in-zircon thermometry: applications and limitations. Contrib Mineral Petrol 156:197–215. doi:10.1007/s00410-008-0281-5

Fujimaki H (1986) Partition coefficients of Hf, Zr, and REE between zircon, apatite, and liquid. Contrib Mineral Petrol 94:42–45. doi:10.1007/BF00371224

Gatehouse BM, Grey IE, Campbell IH, Kelly P (1978) The crystal structure of loveringite—a new member of the crichtonite group. Am Mineral 63:28–36

Geisler T, Pidgeon RT, Kurtz R, Bronswijk WV, Schleicher H (2003) Experimental hydrothermal alteration of partially metamict zircon. Am Mineral 88:1496–1513

Geisler T, Schaltegger U, Tomsachek F (2007) Re-equilibration of zircon in aqueous fluids and melts. Elements 3:43–50. doi:10.2113/gselements.3.1.43

Gerstenberger H, Haase G (1997) A highly effective emitter substance for mass spectrometric Pb isotope ratio determinations. Chem Geol 136:309–312. doi:10.1016/S0009-2541(96)00033-2

Godel B, Barnes SJ, Barnes S-J, Maier WD (2010) Platinum ore in three dimensions: insights from high-resolution X-ray computed tomography. Geology 38:1127–1130. doi:10.1130/G31265.1

Godel B, Rudashevsky NS, Nielsen TFD, Barnes SJ, Rudashevsky VN (2014) New constraints on the origin of the Skaergaard intrusion Cu–Pd–Au mineralization: insights from high-resolution X-ray computed tomography. Lithos 190-191:27–36. doi:10.1016/j.lithos.2013.11.019

Grimes CB, John BE, Cheadle MJ, Mazdab FK, Wooden JL, Swapp S, Schwartz JJ (2009) On the occurrence, trace element geochemistry, and crystallization history of zircon from in situ ocean lithosphere. Contrib Mineral Petrol 158:757–783. doi:10.1007/s00410-009-0409-2

Grove M, Harrison TM (1996) ^{40}Ar diffusion in Fe-rich biotite. Am Mineral 81:940–951

Hamilton MA, Pearson DG, Thompson RN, Kelley SP, Emeleus CH (1998) Rapid eruption of Skye lavas inferred from precise U-Pb and Ar-Ar dating of the Rum and Cuillin plutonic complexes. Nature 394:260–263. doi:10.1038/28361

Hanchar JM, Miller CF (1993) Zircon zonation patterns as revealed by cathololuminescence and backscattered electron images: implications for interpretation of complex crustal histories. Chem Geol 110:1–13. doi:10.1016/0009-2541(93)90244-D

Harker A (1904) The Tertiary igneous rocks of Skye. (Memoir Geological Survey United Kingdom) Glasgow p 481 James Hedderwick and Sons

Harley SL, Kelly NM (2007) Zircon, tiny but timely. Elements 3:13–18. doi:10.2113/gselements.3.1.13

Harrison TM, Zeitler PK (2005) Fundamentals of noble gas thermochronometry. In: Reiner PW, Ehlers TA (eds) Low-temperature thermochronology: techniques, interpretations, and applications, Reviews in Mineralogy and Geochemistry, Chantilly, VA vol. 58, pp 123–149. doi:10.2138/rmg.2005.58.5 The Mineralogical Society of America

Haskin LA, Salpas PA (1992) Genesis of compositional characteristics of Stillwater AN-I and AN-II thick anorthosite units. Geochim Cosmochim 56:1187–212. doi:10.1016/0016-7037(92)90056-O

Heaman LM, LeCheminant AN (1993) Paragenesis and U-Pb systematics of baddeleyite (ZrO_2). Chem Geol 110:95–126. doi:10.1016/0009-2541(93)90249-I

Heaman LM, LeCheminant AN (2000) Anomalous U–Pb systematics in mantle-derived baddeleyite xenocrysts from Ile Bizard: evidence for high temperature radon diffusion? Chem Geol 172:77–93. doi:10.1016/S0009-2541(00)00237-0

Heaman L, Parrish R (1991) U-Pb geochronology of accessory minerals. In: Heaman L, Ludden JN (eds) Applications of radiogenic isotope systems to problems in geology. Mineralogical Association of Canada, short course handbook, Nepean, Canada vol 19. pp 59–102 Mineralogical Association of Canada

Heaman LM, Machado N, Krogh TE, Weber W (1986) Precise U-Pb zircon ages for the Molson dyke swarm and the Fox River sill: constraints for early Proterozoic crustal evolution in northeastern Manitoba, Canada. Contrib Mineral Petrol 94:82–89. doi:10.1007/BF00371229

Hemming SR, Rasbury ET (2000) Pb isotope measurements of sanidine monitor standards: implications for provenance analysis and tephrochronology. Chem Geol 165:331–337. doi:10.1016/S0009-2541(99)00174-6

Hess HH (1960) Stillwater igneous complex, Montana. Geol Soc Am Memoir 80:230

Hickey KA, Barker SLL, Dipple GM, Arehart GB, Donelick RA (2014) The brevity of hydrothermal fluid flow revealed by thermal haloes around giant gold deposits: implications for Carlin-type gold systems. Econ Geol 109:1461–1487

Hiess J, Condon, DJ, McLean N, Noble SR (2012) ^{238}U/^{235}U systematics in terrestrial uranium-bearing mineral. Nature 335:1610–1614. doi:10.1126/science.1215507

Higgins MD (2011) Textural coarsening in igneous rocks. Int Geol Rev 53:354–376. doi:10.1080/00206814.2010.496177

Higgins MD, van Breeman O (1998) The age of the Sept Iles layered mafic intrusion, Canada: implications for the Late Neoproterozoic/Cambrian history of Southeastern Canada. J Geol 106:421–432. doi:10.1086/516033

Hirschmann MM, Renne PR, McBirney AR (1997) ^{40}Ar/^{39}Ar dating of the Skaergaard intrusion. Earth Planet Sci Lett 146:645–658. doi:10.1016/S0012-821X(96)00250-6

Hoatson DM, Blake DH (eds) (2000) Geology and economic potential of the Palaeoproterozoic layered mafic-ultramafic intrusions in the East Kimberley, Western Australia. Aust Geol Surv Organ Bull 246:476

Holland HD, Gottfried D (1955) The effect of nuclear radiation on the structure of zircon. Acta Crystallogr 8:291–300. doi:10.1107/S0365110X55000947

Holness MB, Anderson AT, Mamrtin VM, MacLennan J, Passmore E, Schwindinger K (2007) Textures in partially solidified crystalline nodules: a window into the pore structure of slowly cooled mafic intrusions. J Petrol 48:1243–1264. doi:10.1093/petrology/egm016

Hulbert L (2005) Geology of the Muskox intrusion and associated Ni and Cu occurrences. Geological Survey of Canada, Open File 4881 (CD-ROM)

Hunter RH (1996) Texture development in cumulate rocks. In: Cawthorn RG (ed) Layered intrusions. Elsevier Science B.V., Amsterdam, pp 103–145. doi:10.1016/S0167-2894(96)80006-6

Ireland TR, Williams IS (2003) Considerations in zircon geochronology by SIMS. In: Hanchar JM, Hoskin PWO (eds) Zircon Reviews in mineralogy and geochemistry, Washington, DC vol. 53. pp 215–241.doi:10.2113/0530215 The Mineralogical Society of America

Irvine TN (1982) Terminology for layered intrusions. J Petrol 23:127–162. doi:10.1093/petrology/23.2.127-a

Irvine TN (1987) Appendix I. Glossary of terms for layered intrusions. In: Parsons I (ed) Origins of igneous layering. D. Reidel Publishing Company, Dordrecht, Holland pp 641–647. doi:10.1016/S0167-2894(96)80005–4

Ivanic TJ, Wingate MTD, Kirkland CL, Van Kranendonk MJV, Wyche S (2010) Age and significance of voluminous mafic-ultramafic magmatic events in the Murchison Domain, Yilgarn Craton. Aust J Earth Sci 57:597–614. doi:10.1080/08120099.2010.494765

Jackson ED (1961) Primary textures and mineral associations in the Ultramafic Zone of the Stillwater Complex, Montana. U. S Geol Surv Prof Pap 358:106

Jaffey AH, Flynn KF, Glendenin LE, Bentley WC, Essling AM (1971) Precision measurement of half-lives and specific activities of ^{235}U and ^{238}U. Phys Rev C 4(5):1889–1906. doi:http://dx.doi.org/10.1103/PhysRevC.4.1889

Jerram DA, Cheadle MJ, Philpotts AR (2003) Quantifying the building blocks of igneous rocks: are clustered crystal frameworks the foundation? J Petrol 44:2033–2051. doi:10.1093/petrology/egg069

Kamo SL, Reimold WU, Krogh TE, Colliston WP (1996) A 2.023 Ga age for the Vredefort impact event and a first report of shock metamorphosed zircons in pseudotachylitic breccias and granophyre. Earth Planet Sci Lett 144:369–387. doi:10.1016/S0012-821X(96)00180-X

Kinnaird JA, Hutchinson D, Schurmann L, Nex PAM, de Lange R (2005) Petrology and mineralization of the southern PlatReef: northern limb of the Bushveld Complex, South Africa. Miner Depos 40:576–597. doi:10.1007/s00126-005-0023-9

Kinny PD, Maas R (2003) Lu-Hf and Sm-Nd isotope systems in zircon. In: Hanchar JM, Hoskin PWO (eds) Zircon, Reviews in Mineralogy and Geochemistry, Washington, DC vol. 53. pp 327–341. doi:10.2113/0530327 The Mineralogical Society of America

Kosler J, Sylvester PJ (2003) Present trends and the future of zircon in geochronology: laser ablation ICPMS. In: Hanchar JM, Hoskin PWO (eds.) Zircon, Reviews in Mineralogy and Geochemistry, Washington, DC vol. 53. pp 243–275. doi:10.2113/0530243 The Mineralogical Society of America

Kramers J, Mouri H (2011) The geochronology of the Limpopo Complex: a controversy solved. Geol Soc Am Mem 207:85–106. doi:10.1130/2011.1207(06)

Krogh TE (1973) A low contamination method for the hydrothermal decomposition of zircon and extraction of U and Pb for isotopic age determinations. Geochim Cosmochim Acta 37:485–494. doi:10.1016/0016-7037(73)90213-5

Krogh TE (1982a) Improved accuracy of U-Pb zircon ages by the creation of more concordant systems using an air abrasion technique. Geochim Cosmochim Acta 46:637–649. doi:10.1016/0016-7037(82)90165-X

Krogh TE (1982b) Improved accuracy of U-Pb zircon dating by selection of more concordant fractions using a high gradient magnetic separation technique. Geochim Cosmochim Acta 46:631–635. doi:10.1016/0016-7037(82)90164-8

Krogh TE, Davis GL (1974) Alteration in zircons with discordant U-Pb ages. Carnegie Inst Wash Yearb 73:560–567

Kruger FJ (2005) Filling the Bushveld Complex magma chamber: lateral expansion, roof and floor interaction, magmatic unconformities, and the formation of giant chromitite, PGE and Ti-V-magnetitite deposits. Miner Depos 40:451–472. doi:10.1007/s00126-005-0016-8

Kruger FJ, Kamber BS, Harris PD (1998) Isotopic peculiarities of an Archaean pegmatite (Union Mine, Mica, South Africa): geochemical and geochronological implications. Precambrian Res 91:253–267. doi:10.1016/S0301-9268(98)00052-7

Krumrei TV, Villa IM, Marks MAW, Markl G (2006) A $^{40}Ar/^{39}Ar$ and U/Pb isotopic study of the Ilimaussaq complex, South Greenland: implications for the ^{40}K decay constant and for the duration of magmatic activity in a peralkaline complex. Chem Geol 227:258–273. doi:10.1016/j.chemgeo.2005.10.004

Kuiper YD (2002) The interpretation of inverse isochron diagrams in $^{40}Ar/^{39}Ar$ geochronology. Earth Planet Sci Lett 203:499–506. doi:10.1016/S0012-821X(02)00833-6

Kuiper KF, Deino A, Hilgen FJ, Krijgsman W, Renne PR, Wijbrans JR (2008) Synchronizing rock clocks of Earth History. Science 320:500–504. doi:10.1126/science.1154339

LeCheminant AN, Heaman LM (1989) Mackenzie igneous events, Canada: Middle Proterozoic hotspot magmatism associated with ocean opening. Earth Planet Sci Lett 96:38–48. doi:10.1016/0012-821X(89)90122-2

Lee JKW (1995) Multipath diffusion in geochronology. Contrib Mineral Petrol 120:60–82. doi:10.1007/BF00311008

Lee CA (1996) A review of mineralization in the Bushveld Complex and some other layered intrusions. In Cawthorn RG (ed) Layered intrusions. Elsevier Science B.V., Amsterdam, pp 103–145. doi:10.1016/S0167-2894(96)80006-6

Lee J-Y, Marti K, Severinghaus JP, Kawamura K, Yoo H-S, Lee JB, Kim JS (2006) A redetermination of the isotopic abundances of atmospheric Ar. Geochim Cosmochim Acta 70:4507–4512. doi:10.1016/j.gca.2006.06.1563

Li C, Ripley EM, Merino E, Maier WD (2004) Replacement of base metal sulfides by actinolite, epidote, calcite, and magnetite in the UG2 and Merensky Reef of the Bushveld Complex, South Africa. Econ Geol 99:173–184. doi:10.2113/gsecongeo.99.1.0173

Lindsley DH, Brown GM, Muir ID (1969) Conditions of the ferrowollastonite-ferrohedenbergite inversion in the Skaergaard intrusion. East Greenland. Mineral Soc Am Spec Pap 2:193–201

Ludwig KR (2003) Isoplot/Ex 3.00, a Geochronological Toolkit for Microsoft Excel: Berkeley Geochronology Center

Lumpkin GR (1999) Physical and chemical characteristics of baddeleyite (monoclinic zirconia) in natural environments: an overview and case study. J Nucl Mater 274:206–217

Luvizotto GL, Zack T, Meyer HP, Ludwig T, Triebold S, Kronz A, Münker C, Stockli DF, Prowatke S, Klemme S, Jacob DE, von Eynatten H (2009) Rutile crystals as potential trace element and isotope mineral standards for microanalysis. Chem Geol 261:346–369. doi:10.1016/j.chemgeo.2008.04.012

Mackie RA, Scoates JS, Weis D (2009) Age and Nd–Hf isotopic constraints on the origin of marginal rocks from the Muskox layered intrusion (Nunavut, Canada) and implications for the evolution of the 1.27 Ga Mackenzie large igneous province. Precambrian Res 172:46–66. doi:10.1016/j.precamres.2009.03.007

Maier WD, Barnes S-J, Gartz V, Andrews G (2003) Pt-Pd Reefs in magnetites of the Stella layered intrusion, South Africa: a world of new exploration opportunities for platinum group elements. Geology 31:885–888. doi:10.1130/G19746.1

Maier WD, Barnes S-J, Groves DI (2013) The Bushveld Complex, South Africa: formation of platinum-palladium, chrome- and vanadium-rich layers via hydrodynamic sorting of a mobilized cumulate slurry in a large, relatively slowly cooling, subsiding magma chamber. Mineral Depos 48:1–56. doi:10.1007/s00126-012-0436-1

Mapeo RBM, Kampunzu AB, Ramokate LV, Corfu F, Key RM (2004) Bushveld-age magmatism in southeastern Botswana: Evidence from U-Pb zircon and titanite geochronology of the Moshaneng Complex. S Afr J Geol 107:219–232. doi:10.2113/107.1-2.219

Mark DF, Stuart FM, de Podesta M (2011) New high-precision measurements of the isotopic composition of atmospheric argon. Geochim Cosmochim Acta 75:7494–7501. doi:10.1016/j.gca.2011.09.042.

Mathez EA (1995) Magmatic metasomatism and formation of the Merensky reef, Bushveld Complex. Contrib Mineral Petrol 119:277–286. doi:10.1007/BF00307287

Mathez EA, VanTongeren JA, Schweitzer J (2013) On the relationships between the Bushveld Complex and its felsic roof rocks, part 1: petrogenesis of Rooiberg and related felsites. Contrib Mineral Petrol 166:435–449. doi:10.1007/s00410-013-0884-3

Mattinson JM (2005) Zircon U-Pb chemical abrasion ("CA-TIMS") method: Combined annealing and multi-step partial dissolution analysis for improved precision and accuracy of zircon ages. Chem Geol 220:47–66. doi:10.1016/j.chemgeo.2005.03.011

Mattinson JM (2013) Revolution and evolution: 100 years of U-Pb geochronology. Elements 8, 53–57. doi: 10.2113/gselements.9.1.53

McBirney AR, Creaser RA (2003) The Skaergaard Layered Series, Part VII: Sr and Nd isotopes. J Petrol 44:757–771. doi:10.1093/petrology/44.4.757

McCallum IS (1996) The Stillwater Complex. In: Cawthorn RG (ed) Layered intrusions. Elsevier, Amsterdam, pp 441–484. doi:10.1016/S0167-2894(96)80015-7

McCourt S, Armstrong RA (1998) SHRIMP U–Pb zircon geochronology of granites from the Central Zone, Limpopo Belt, southern Africa: implications for the age of the Limpopo Orogeny. S Afr J Geol 101:329–338

McDougall I., Harrison T.M. (1999) Geochronology and thermochronology by the $^{40}Ar/^{39}Ar$ method. Oxford University Press, New York, NY pp 269

McLean NM, Bowring JF, S. A. Bowring (2011) An algorithm for U-Pb isotope dilution data reduction and uncertainty propagation. Geochem Geophys Geosyst 12(Q0AA18):1–26. doi:10.1029/2010GC003478.

McLelland JM, Chiarenzelli J (1990) Isotopic constraints on emplacement age of anorthositic rocks of the Marcy massif, Adirondack Mtns., New York. J Geol 98:19–41

Meinhold G (2010) Rutile and its applications in earth sciences. Earth-Sci Rev 102:1–28. doi:10.1016/j.earscirev.2010.06.001

Meurer WP, Boudreau AE (1996) Petrology and mineral compositions of the Middle Banded Series of the Stillwater Complex, Montana. J Petrol 37:583–607

Meurer WP, Boudreau AE (1998) Compaction of igneous cumulates. Part I. Whole-rock compositions as an indicator of the trapped liquid proportions in the Stillwater Complex, Montana. J Geol 106:281–292. doi:10.1086/516022

Meurer WP, Meurer MES (2006) Using apatite to dispel the ''trapped liquid'' concept and to understand the loss of interstitial liquid by compaction in mafic cumulates: an example from the Stillwater Complex, Montana. Contrib Mineral Petrol 151:187–201. doi:10.1007/s00410-005-0054-3

Meurer WP, Willmore CC, Boudreau AE (1999) Metal redistribution during fluid exsolution and migration in the Middle Banded series of the Stillwater Complex, Montana. Lithos 47:143–156. doi:10.1016/S0024-4937(99)00012-2

Mezger K, Hanson GN, Bohlen SR (1989) High-precision U-Pb ages of metamorphic rutile: application to the cooling history of high-grade terranes. Earth Planet Sci Lett 96:106–118. doi:10.1016/0012-821X(89)90126-X

Miller JS, Matzel JEP, Miller CF, Burgess SD, Miller RB (2007) Zircon growth and recycling during the assembly of large, composite arc plutons. J Volcanol Geotherm Res 167:282–299. doi:10.1016/j.jvolgeores.2007.04.019

Min K, Mundil R, Renne PR, Ludwig KR (2000) A test for systematic errors in $^{40}Ar/^{39}Ar$ geochronology through comparison with U/Pb analysis of a 1.1-Ga rhyolite. Geochim Cosmochim Acta 64:73–98. doi:10.1016/S0016-7037(99)00204-5

Minor DR, Mukasa SB (1997) Zircon U-Pb and hornblende ^{40}Ar –^{39}Ar ages for the Dufek layered mafic intrusion, Antarctica: implications for the age of the Ferrar large igneous province. Geochim Cosmochim Acta 61:2497–2504. doi:10.1016/S0016-7037(97)00098-7

Mitchell AA, Scoon RN (2007) The Merensky Reef at Winnaarshoek, Eastern Bushveld Complex: a primary magmatic hypothesis based on a wide reef facies. Econ Geol 102:971–1009. doi:10.2113/gsecongeo.102.5.971

Mitchell AA, Scoon RN (2012) The PlatReef of the Bushveld Complex, South Africa: a new hypothesis of multiple, non-sequential magma replenishment based on observations at the Akanani Project, north-west of Mokopane. S Afr J Geol 115:535–550. doi:10.2113/gssajg.115.4.535

Mondal SK, Ripley EM, Li C, Frei R (2006) The genesis of Archaean chromitites from the Nuasahi and Sukinda massifs in the Singhbhum Craton, India. Precambrian Research 148:45–66. doi:10.1016/j.precamres.2006.04.001

Morisset C-E, Scoates JS, Weis D, Friedman RM (2009) U-Pb and $^{40}Ar/^{39}Ar$ geochronology of the Saint-Urbain and Lac Allard (Havre-Saint-Pierre) anorthosites and their associated Fe–Ti oxide ores, Québec: Evidence for emplacement and slow cooling during the collisional Ottawan orogeny in the Grenville Province. Precambrian Res 174:95–116. doi:10.1016/j.precamres.2009.06.009

Morrison DA, Davis DW, Wooden JL, Gogard DD, Maczuga DE, Phinney WC, Ashwal LD (1985) Age of the Mulcahy Lake intrusion, northwest Ontario, and implications for the evolution of greenstone-granite terrains. Earth Planet Sci Lett 73:306–316. doi:10.1016/0012-821X(85)90079-2

Morse SA (1986) Convection in aid of adcumulus growth. J Petrol 27:1183–1214. doi:10.1093/petrology/27.5.1183

Morse SA (2008) Toward a thermal model for the Skaergaard liquidus. Am Mineral 93:248–251. doi:10.2138/am.2008.2792

Moser DE (1997) Dating the shock wave and thermal imprint of the giant Vredefort impact, South Africa. Geology 25:7–10. doi:10.1130/0091-7613(1997)0252.3.CO;2

Naldrett AJ, Wilson A, Kinnaird J, Chunnett G (2009) PGE tenor and metal ratios within and below the Merensky Reef, Bushveld Complex: implications for its genesis. J Petrol 50:625–659. doi:10.1093/petrology/egp015

Nardi LVS, Formoso MLL, Müller IF, Fontana E, Jarvis K, Lamarao C (2013) Zircon/rock partition coefficients of REEs, Y, Th, U, Nb, and Ta in granitic rocks: Uses for provenance and mineral exploration purposes. Chem Geol 335:1–7. doi:10.1016/j.chemgeo.2012.10.043

Nasdala L, Zhang M, Kempe U, Panczer G, Gaft M, Andrut M, Plötze M (2003) Spectroscopic methods applied to zircon. In: Hanchar JM, Hoskin PWO (eds) Zircon, Reviews in Mineralogy and Geochemistry, Washington, DC vol. 53. pp 427–467. doi:10.2113/0530427 The Mineralogical Society of America

Nasdala L, Hanchar JM, Kronz A, Whitehouse MJ (2005) Long-term stability of alpha particle damage in natural zircon. Chem Geol 220:83–103. doi:10.1016/j.chemgeo.2005.03.012

Nemchin AA, Horstwood MSA, Whitehouse MJ (2013) High-spatial-resolution geochronology. Elements 9:31–37. doi:10.2113/gselements.9.1.31

Nilsen O, Corfu F, Roberts D (2007) Silurian gabbro-diorite-trondhjemite plutons in the Trondheim Nappe Complex, Caledonides, Norway: petrology and U-Pb geochronology. Nor J Geol 87:329–342

Nomade S, Renne PR, Merkle RKW (2004) $^{40}Ar/^{39}Ar$ age constraints on ore deposition and cooling of the Bushveld Complex, South Africa. J Geol Soc Lond 161:411–420. doi:10.1144/0016764903-065

Norman MD, Nemchin AA (2014) A 4.2 billion year old impact basin on the Moon: U–Pb dating of zirconolite and apatite in lunar melt rock 67955. Earth Planet Sci Lett 388:387–398. doi:10.1016/j.epsl.2013.11.040

Nunes PD (1981) The age of the Stillwater complex—a comparison of U-Pb zircon and Sm-Nd isochron systematics. Geochim Cosmochim Acta 45:1961–1963. doi:10.1016/0016-7037(81)90028-4

Nunes PD, Tilton GR (1971) Uranium-lead ages of minerals from the Stillwater igneous complex and associated rocks, Montana. Geol Soc Am Bull 82:2231–2250

Nutman AP, McGregor VR, Friend CRL, Bennett VC, Kinny PD (1996) The Itsaq gneiss complex of southern West Greenland; the world's most extensive record of early crustal evolution (3900-3600 Ma). Precambrian Res 78:1–39

Oberthür T, Davis DW, Blenkinsop TG, Höhndorf A (2002) Precise U-Pb mineral ages, Rb-Sr and Sm-Nd systematics for the Great Dyke, Zimbabwe—constraints on late Archean events in the Zimbabwe craton and Limpopo belt. Precambrian Res 113:293–305. doi:10.1016/S0301-9268(01)00215-7

O'Neil J, Maurice C, Stevenson RK, Larocque J, Cloquet C, David J, Francis D (2007) The geology of the 3·8 Ga Nuvvuagittuk (Porpoise Cove) Greenstone Belt, northern Superior Province, Canada. In: Kranendonk MJ, Smithies RH, Bennett VC (eds) Earth's oldest rocks. Elsevier, Amsterdam, pp. 219–250

O'Neil, J, Francis D, Carlson RW (2011) Implications of the Nuvvuagittuq greenstone belt for the formation of Earth's early crust. J Petrol 52:985–1009. doi:10.1093/petrology/egr014

O'Neil, J, Carlson RW, Paquette J-L, Francis D (2012) Formation age and metamorphic history of the Nuvvuagittuq Greenstone Belt. Precambrian Res 220-221:23–44. doi:10.1016/j.precamres.2012.07.009

Olsson JR, Söderlund U, Klausen MB, Ernst RE (2010) U–Pb baddeleyite ages linking major Archean dyke swarms to volcanic-rift forming events in the Kaapvaal craton (South Africa), and a precise age for the Bushveld Complex. Precambrian Res 183:490–500. doi:10.1016/j.precamres.2010.07.009

Paces JB, Miller JD Jr (1993) Precise U-Pb ages of Duluth Complex and related mafic intrusions, northeastern Minnesota: geochronological insights to physical, Petrogenetic, paleomagnetic, and tectonomagmatic processes associated with the 1.1 Ga Midcontinent Rift System. J Geophys Res 98(B4):13,997–14,013

Page RW, Hoatson DM (2000) Geochronology of the mafic-ultramafic intrusions. In: Hoatson DM, Blake DH (eds) Geology and economic potential of the Paleoproterozoic layered mafic-ultramafic intrusions in the East Kimberley, Western Australia. AGSO Bulletin 246:163–172

Parrish RR (1987) An improved micro-capsule for zircon dissolution in U–Pb geochronology. Chem Geol Isot Geosci Sect 66:99–102. doi:10.1016/0168-9622(87)90032-7

Parrish RR, Noble SR (2003) Zircon U-Th-Pb geochronology by isotope dilution—thermal ionization mass spectrometry (ID-TIMS). In: Hanchar JM, Hoskin PWO (eds) Zircon, Reviews in Mineralogy and Geochemistry, Washington, DC vol. 53. pp 183–213. doi:10.2113/0530183 The Mineralogical Society of America

Parsons I (ed) (1987) Origins of igneous layering. NATO ASI series C 196. D. Reidel Publishing Company, Dordrecht, Holland p 666

Pasteels P, Demaiffe D, Michot J (1979) U-Pb and Rb-Sr geochronology of the eastern part of the south Rogaland igneous complex, southern Norway. Lithos 12:199–208. doi:10.1016/0024-4937(79)90004-5

Patchett PJ, Kouvo O, Hedge CE, Tatsumoto M (1981) Evolution of continental crust and mantle heterogeneity: evidence from Hf isotopes. Contrib Mineral Petrol 78:279–297. doi:10.1007/BF00398923

Pitra P, de Waal SA (2001) High-temperature, low-pressure metamorphism and development of prograde symplectites, Marble Hall Fragment, Bushveld Complex (South Africa). J Metamorph Petrol 19:311–325

Polat A, Frei R, Scherstén A, Appel PWU (2010) New age (ca. 2790 Ma), mantle source composition and geodynamic constraints on the Archean Fiskenaesset anorthosite complex, SW Greenland. Chem Geol 277:1–20. doi:10.1016/j.chemgeo.2010.06.016

Premo WR, Helz RT, Zientek ML, Langston RB (1990) U-Pb and Sm-Nd ages for the Stillwater Complex and its associated sills and dikes, Beartooth Mountains, Montana: Identification of a parent magma? Geology 18:1065–1068. doi:10.1130/0091-7613(1990)018 2.3.CO;2

Prendergast MD (2008) Archean komatiitic sill-hosted chromite deposits in the Zimbabwe craton. Econ Geol 103:981–1004. doi:10.2113/gsecongeo.103.5.981

Prevec SA, Ashwal LD, Mkaza MS (2005) Mineral disequilibrium in the Merensky Reef, western Bushveld Complex, South Africa: new Sm–Nd isotopic evidence. Contrib Mineral Petrol 149:306–315. doi:10.1007/s00410-005-0650-2

Pupin JP (1980) Zircon and granite petrology. Contrib Mineral and Petrol 73:207–220. doi:10.1007/BF00381441

Rajesh HM, Chisonga BC, Shindo K, Beukes NJ, Armstrong RA (2013) Petrographic, geochemical and SHRIMP U–Pb titanite age characterization of the Thabazimbi mafic sills: Extended time frame and a unifying petrogenetic model for the Bushveld Large Igneous Province. Precambrian Res 230:79–102. doi:10.1016/j.precamres.2013.02.002

Rasmussen B, Fletcher IR (2004) Zirconolite: a new U-Pb chronometer for mafic igneous rocks. Geology 32:785–788. doi:10.1130/G20658.1

Renne PR, Swisher CC, Deino AL, Karner DB, Owens T, DePaolo DJ (1998) Intercalibration of standards, absolute ages and uncertainties in $^{40}Ar/^{39}Ar$ dating. Chem Geol 145:117–152. doi:10.1016/S0009-2541(97)00159-9

Renne PR, Mundil R, Balco G, Min K, Ludwig KR (2010) Joint determination of ^{40}K decay constants and $^{40}Ar^*/^{40}K$ for the Fish Canyon sanidine standard, and improved accuracy for $^{40}Ar/^{39}Ar$ geochronology. Geochim Cosmochim Acta 74:5349–5367. doi: 10.1016/j.gca.2010.06.017.

Renne PR, Balco G, Ludwig KR, Mundil R, Mon K (2011) Response to the comment by W.H. Schwarz et al. on "Joint determination of ^{40}K decay constants and $^{40}Ar^*/^{40}K$ for the Fish Canyon sanidine standard, and improved accuracy for $^{40}Ar/^{39}Ar$ geochronology" by P.R. Renne et al. (2010). Geochim Cosmochim Acta 75:5097–5100. doi:10.1016/j.gca.2011.06.021

Rioux M, Bowring S, Dudas F, Hanson R (2010) Characterizing the U–Pb systematics of baddeleyite through chemical abrasion: application of multi-step digestion methods to baddeleyite geochronology. Contrib Mineral Petrol 160:777–801. doi:10.1007/s00410-010-0507-1

Rios S, Salje EKH, Zhang M, Ewing RC (2000) Amorphization in zircon: evidence for direct impact damage. J Phys Condens Matter 12:2401–2412. doi:10.1088/0953-8984/12/11/306

Roddick JC (1987) Generalized numerical error analysis with application to geochronology and thermodynamics. Geochim Cosmochim Acta 51:2129–2135. doi:10.1016/0016-7037(87)90261-4

Roelofse F, Ashwal LD (2012) The Lower Main Zone in the Northern Limb of the Bushveld Complex—a >1.3 km thick sequence of intruded and variably contaminated crystal mushes. J Petrol 53:1449–1476. doi:10.1093/petrology/egs022

Rollinson H, Appel PWU, Frei R (2002) A metamorphosed, Early Archean chromitite from West Greenland: Implications for the genesis of Archean anorthositic chromitites. J Petrol 43:2143–2170. doi:10.1093/petrology/43.11.2143

Saleeby JB (1992) Age and tectonic setting of the Duke Island ultramafic intrusion, southeast Alaska. Can J Earth Sci 29:506–522

Scherer EE, Münker C, Mezger K (2001) Calibration of the lutetium-hafnium clock. Science 293:683–687. doi:10.1126/science.1061372

Scherer EE, Whitehouse MJ, Münker C (2007) Zircon as a monitor of crustal growth. Elements 3:19–24. doi:10.2113/gselements.3.1.19

Schmitt AK, Chamberlain KR, Swapp SM, Harrison TM (2010) In situ U–Pb dating of microbaddeleyite by secondary ion mass spectrometry. Chem Geol 269:386–395. doi:10.1016/j.chemgeo.2009.10.013

Schmitt AK, Perfit MR, Rubin KH, Stockli DF, Smith MC, Cotsonika LA, Zellmer GF, Ridley WI, Lovera OM (2011) Rapid cooling rates at an active mid-ocean ridge from zircon thermochronology. Earth Planet Sci Lett 302:349–358. doi:10.1016/j.epsl.2010.12.022

Schmitz MD, Bowring SA (2003) Constraints on the thermal evolution of continental lithosphere from U-Pb accessory mineral thermochronometry of lower crustal xenoliths, southern Africa. Contrib Mineral Petrol 144:592–618. doi:10.1007/s00410-002-0419-9

Schmitz MD, Kuiper KF (2013) High-precision geochronology. Elements 9:25–30. doi: 10.2113/gselements.9.1.25

Schmitz MD, Schoene B (2007) Derivation of isotope ratios, errors, and error correlations for U-Pb geochronology using ^{205}Pb-^{235}U-(^{233}U)-spiked isotope dilution thermal ionization mass spectrometry data. Geochem Geophys Geosyst 8(Q0800):1–20 doi:10.1029/2006GC001492

Schmitz MD, Bowring SA, Ireland TR (2003) Evaluation of Duluth Complex anorthositic series (AS3) zircon as a U-Pb geochronological standard: new high-precision isotope dilution thermal ionization mass spectrometry results. Geochim Cosmochim Acta 67:3665–3672. doi:10.1016/S0016-7037(03)00200-X

Schoenberg R, Kruger FJ, Nägler TF, Meisel T, Kramers JD (1999) PGE enrichment in chromitite layers and the Merensky Reef of the western Bushveld Complex; a Re–Os and Rb–Sr isotope study. Earth Planet Sci Lett 172:49–64. doi:10.1016/S0012-821X(99)00198-3

Schoene B (2014) U-Th-Pb geochronology. Treatise on geochemistry, 2nd edn. Amsterdam, The Netherlands pp 341–378. doi:10.1016/B978-0-08-095975-7.00310-7 Elsevier Ltd.

Schoene B, Crowley JL, Condon DJ, Schmitz MD, Bowring SA (2006) Reassessing the uranium decay constants for geochronology using ID-TIMS U–Pb data. Geochim Cosmochim Acta 70:426–445. doi:10.1016/j.gca.2005.09.007

Schoene B, Latkoczy C, Schaltegger U, Günther D (2010) A new method integrating high-precision U–Pb geochronology with zircon trace element analysis (U–Pb TIMS-TEA). Geochim Cosmochim Acta 74:7144–7159. doi:10.1016/j.gca.2010.09.016

Schwartz JJ, John BE, Cheadle MJ, Miranda EA, Grimes CB, Wooden JL, Dick HJB (2005) Dating the growth of oceanic crust at a slow-spreading ridge. Science 310:654–657. doi:10.1126/science.1116349

Scoates RFJ (1990) The Fox River Sill, Northeastern Manitoba—a major stratiform intrusion. Manitoba Energy and Mines, Geological Report GR82-3, p 192

Scoates JS, Chamberlain KA (1995) Baddeleyite (ZrO_2) and zircon ($ZrSiO_4$) from anorthositic rocks in the Laramie anorthosite complex, Wyoming: petrologic consequences and U-Pb ages. Am Mineral 80:1319–1329

Scoates JS, Chamberlain KA (2003) Geochronologic, geochemical and isotopic constraints on the origin of monzonitic and related rocks in the Laramie anorthosite complex, Wyoming, USA. Precambrian Res 124:269–304. doi:10.1016/S0301-9268(03)00089-5

Scoates JS, Friedman RM (2008) Precise age of the platiniferous Merensky Reef, Bushveld Complex, South Africa, by the U-Pb zircon chemical abrasion ID-TIMS technique. Econ Geol 103:465–471. doi:10.2113/gsecongeo.103.3.465

Scoates JS, Scoates RFJ (2013) Age of the Bird River Sill, Southeastern Manitoba, Canada, with implications for the secular variation of layered intrusion-hosted stratiform chromite mineralization. Econ Geol 108:895–907. doi:10.2113/econgeo.108.4.895

Scoates JS, Weis D, Williams GA, Henriques F, Tam L (2006) Initial lead isotopic compositions of plagioclase feldspar: leaching experiments, residue imaging, and applications. Geological Association of Canada-Mineralogical Association of Canada annual meeting, May 14-17, 2006, Montréal (abstract)

Scoates JS, Weis D, Franssens M, Mattielli N, Annell H, Frey FA, Nicolaysen K, Giret A (2007) The Val gabbro plutonic suite: a sub-volcanic intrusion emplaced at the end of flood basalt volcanism on the Kerguelen Archipelago. J Petrol 49:79–105. doi:10.1093/petrology/egm071

Scoates JS, Wall CJ, Friedman RM, Booth K, Scoates RFJ, Couëslan C, Macek J (2010) Recent progress in determining the precise age of ultramafic sills and mafic dikes associated with mineralization in the Thompson Nickel Belt, Manitoba, Canada. 11th international platinum symposium, Ontario Geological Survey, Miscellaneous Release Data 269:1–4

Scoates JS, Wall CJ, Friedman RM, Chamberlain KR (2011) Revisiting the age of the Merensky Reef, Bushveld Complex. Goldschmidt conference abstracts (Prague), Mineralogical Magazine 75 (3), p. 1831 (abstract)

Scoates JS, Wall CJ, Friedman RM, VanTongeren JA, Mathez EA (2012) Age of the Bushveld Complex. Goldschmidt conference abstracts (Montreal), Mineralogical Magazine 76, p. 2348 (abstract)

Silver LT, Deutsch S (1963) Uranium-lead isotopic variations in zircons: a case study. J Geol 71:721–758

Smith CH (1962) Notes on the Muskox intrusion, Coppermine River area, District of Mackenzie. Geol Surv of Can Pap 61–25, p 16

Smith SS, Basson IJ (2006) Shape and distribution analysis of Merensky Reef potholing, Northam Platinum Mine, western Bushveld Complex: implications for pothole formation and growth. Miner Depos 41:281–295. doi:10.1007/s00126-006-0059-5

Smith DS, Basson IJ, Reid DL (2003) Normal reef subfacies of the Merensky reef at Northam platinum mine, Zwartklip facies, Western Bushveld Complex, South Africa. Canadian Mineral 42:243–260. doi:10.2113/gscanmin.42.2.243

Smith ME, Chamberlain KR, Singer BS, Carroll AR (2010) Eocene clocks agree: coeval $^{40}Ar/^{39}Ar$, U-Pb, and astronomical ages from the Green River Formation. Geology 38:527–530. doi:10.1130/G30630.1

Söderlund U, Hofmann A, Klausen MB, Olsson JR, Ernst RE, Persson PO (2010) Towards a complete magmatic barcode for the Zimbabwe craton: Baddeleyite U–Pb dating of regional dolerite dyke swarms and sill complexes. Precambrian Res 183:388–398.

Stacey JS, Kramers JD (1975) Approximation of terrestrial lead isotope evolution by two-stage model. Earth Planet Sci Lett 26:207–221. doi:10.1016/0012-821X(75)90088-6

Stewart BW, DePaolo DJ (1990) Isotopic studies of processes in mafic magma chambers: II. The Skaergaard Intrusion, East Greenland. Contrib Mineral Petrol 104:125–141

Stewart BW, DePaolo DJ (1996) Isotopic studies of processes in mafic magma chambers: III. The Muskox intrusion, Northwest Territories, Canada. In: Basu A, Hart S (eds) Earth processes: reading the isotopic code, vol. 95. Geophysical Monograph, American Geophysical Union, Washington, DC pp 277–292

Storey M, Duncan RA, Swisher CC III (2007) Paleocene-Eocene Thermal Maximum and the opening of the Northeast Atlantic. Science 316:587–589. doi:10.1126/science.1135274

Tam LJ (2005) Pb and Sr isotopic compositions and trace element concentrations of plagioclase from the Merensky Reef in the Rustenburg sector of the Bushveld Complex, South Africa. Unpublished BSc thesis, University of British Columbia, p 86

Tarkian M, Mutanen T (1987) Loveringite from the Koitelainen layered intrusion, Northern Finland. Mineral Petrol 37:37–50

Tegner C, Duncan RA, Bernstein S, Brooks CK, Bird DK, Storey M (1998) ^{40}Ar –^{39}Ar geochronology of Tertiary mafic intrusions along the East Greenland rifted margin: relation to flood basalts and the Iceland hotspot track. Earth Planet Sci Lett 156:75–99. doi:10.1016/S0012-821X(97)00206-9

Tera F, Wasserburg GJ (1972) U–Th–Pb systematics in three Apollo 14 basalts and the problem of initial Pb in lunar rocks. Earth Planet Sci Lett 17:281–304. doi:10.1016/0012-821X(72)90128-8

Tilton GR, Davis GL, Wetherill GW, Aldrich LT (1957) Isotopic ages of zircon from granites and pegmatites. Trans Am Geophys Union 38:360–371

Turner S, Costa F (2007) Measuring timescales of magmatic evolution. Elements 3:267–272. doi:10.2113/gselements.3.4.267

Turtle EP, Pierazzo E, O'Brien DP (2003) Numerical modeling of impact heating and cooling of the Vredefort impact structure. Meteorit Planet Sci 38:293–303. doi:10.1111/j.1945-5100.2003.tb00265.x

Valley JW (2003) Oxygen isotopes in zircon. In: Hanchar JM, Hoskin PWO (eds) Zircon, Reviews in Mineralogy and Geochemistry, Washington, DC vol. 53, pp 343–385. doi:10.2113/0530343 The Mineralogical Society of America

Valley JW, Lackey JS, Cavosie AJ, Clechenko CC, Spicuzza MJ, Basei MAS, Bindeman IN, Ferreira VP, Sial AN, King EM, Peck WH, Sinha AK, Wei CS (2005) 4.4 billion years of crustal maturation: oxygen isotope ratios of magmatic zircon. Contrib Mineral Petrol 150:561–580. doi:10.1007/s00410-005-0025-8

Vavra G (1993) A guide to quantitative morphology of accessory zircon. Chem Geol 110:15–28. doi:10.1016/0009-2541(93)90245-E

Vermaak CF (1976) The Merensky Reef—thoughts on its environment and genesis. Econ Geol 71:1270–1298. doi:10.2113/gsecongeo.71.7.1270

Wagner PA (1929) The platinum deposits and mines of South Africa. Oliver and Boyd, Edinburgh, p 326

Wager LR, Brown GM (1967) Layered igneous rocks. Oliver & Boyd, Edinburgh, Great Britain p 588

Wager LR, Brown GM, Wadsworth WJ (1960) Types of igneous cumulates. J Petrol 1:73–85. doi:10.1093/petrology/1.1.73

Wall CJ (2009) Uranium-lead geochronology of granophyres from the Archean Stillwater Complex, Montana (USA): characterization of uranium-bearing accessory minerals (zircon, titanite, rutile) and preliminary dating results. Unpublished B. Sc. Honours Thesis, University of British Columbia, 60 pages

Wall CJ, Scoates JS, Friedman RM, Meurer WP (2010) Refining the precise age and duration of magmatism related to the Stillwater Complex. 11th international platinum symposium, Ontario Geological Survey, Miscellaneous Release–Data 269:1–4

Wall CJ, Scoates JS, Friedman RM, Meurer WP (2013) Identifying the timing of magma inputs and hiatuses during emplacement and crystallization of the Stillwater complex by high-precision U-Pb geochronology. William Smith Meeting of the Geological Society of London, London, UK, June 25–27, 2013 (abstract)

Walraven F (1997) Geochronology of the Rooiberg Group, Transvaal Supergroup, South Africa. Economic Geology Research Unit Information Circular, University of Witwatersrand, 316, p 21

Walraven F, Hattingh E (1993) Geochronology of the Nebo granite, Bushveld Complex. S Afr J Geol 96:31–41

Walraven F, Armstrong RA, Kruger FJ (1990) A chronostratigraphic framework for the north-central Kaapvaal craton, the Bushveld Complex and the Vredefort structure. Tectonophysics 171:23-48

Watson EB, Liang Y (1995) A simple model for sector zoning in slowly grown crystals: implications for growth rate and lattice diffusion, with emphasis on accessory minerals in crustal rocks. Am Mineral 80:1179-1187

Watson EB, Wark DA, Thomas JB (2006) Crystallization thermometers for zircon and rutile. Contrib Mineral Petrol 151: 413–433. doi:10.1007/s00410-006-0068-5

Webb SJ, Cawthorn RG, Nguuri T, James D (2004) Gravity modeling of Bushveld Complex connectivity supported by Southern African seismic experiment results. S Afr J Geology 107:207–218. doi:10.2113/107.1-2.207

Wendt I, Carl C (1991) The statistical distribution of the mean squared weighted deviation. Chem Geol 86:275–285. doi:10.1016/0168-9622(91)90010-T

Wetherill GW (1956) Discordant uranium–lead ages. Trans Am Geophys Union 37:320–326

White WM (2013) Geochemistry. Wiley-Blackwell, West Sussex, UK p 668.

Williams IS, Compston W, Collerson KD, Arriens PA, Lovering JF (1983) A reassessment of the age of the Windmill metamorphics, Casey area. In: Oliver RL, James PR, Jago JB (eds) Antarctic earth science. Australian Academy of Science, Canberra, pp 73–76

Wotzlaw J-F, Bindeman IN, Schaltegger U, Brooks CK, Naslund HR (2012) High resolution insights into episodes of crystallization, hydrothermal alteration and remelting in the Skaergaard intrusive complex. Earth Planet Sci Lett 355-356:199–212. doi:10.1016/j.epsl.2012.08.042

Yudovskaya M, Kinnaird J, Naldrett AJ, Rodionov N, Antonov A, Simakin S, Kuzmin D (2013) Trace-element study and age dating of zircon from chromitites of the Bushveld Complex (South Africa). Mineral Petrol 107:915–942. doi:10.1007/s00710-013-0269-3

Zaccarini F, Stumpfl EF, Garuti G (2004) Zirconolite and Zr-Th-U minerals in chromitites of the Finero Complex, Western Alps, Italy: evidence for carbonatite-type metasomatism in a subcontinental mantle plume. Can Mineral 42:1825–1845. doi:10.2113/gscanmin.42.6.1825

Zientek ML, Corson SR, West RD (2005) Geochemical surveys of soil and talus fines and the discovery of the J-M Reef, Stillwater Complex, Montana (Chapter 18). In: Mungall JE (ed) Exploration for platinum-group element deposits, vol. 5. Mineralogical Association of Canada, Short Course Series, pp 391–407

Zirakparvar NA, Mathez EA, Scoates JS, Wall CJ 2014 Zircon Hf isotope evidence for an enriched mantle source for the Bushveld Igneous Complex. Contrib Mineral Petrol 168:1050. doi:10.1007/s00410-014-1050-2

Zhong H, Zhu W-G (2006) Geochronology of layered mafic intrusions from the Pan-Xi area in the Emeishan large igneous province, SW China. Miner Depos 41:599–606. doi:10.1007/s00126-006-0081-7